

2022

## Direct Ink Writing Printability – Ashby-like Plots for Guided Design

Domenic Cipollone

West Virginia University, [dtcipollone@mix.wvu.edu](mailto:dtcipollone@mix.wvu.edu)

Follow this and additional works at: <https://researchrepository.wvu.edu/etd>

 Part of the [Materials Science and Engineering Commons](#)

---

### Recommended Citation

Cipollone, Domenic, "Direct Ink Writing Printability – Ashby-like Plots for Guided Design" (2022). *Graduate Theses, Dissertations, and Problem Reports*. 11470.

<https://researchrepository.wvu.edu/etd/11470>

This Dissertation is protected by copyright and/or related rights. It has been brought to you by the The Research Repository @ WVU with permission from the rights-holder(s). You are free to use this Dissertation in any way that is permitted by the copyright and related rights legislation that applies to your use. For other uses you must obtain permission from the rights-holder(s) directly, unless additional rights are indicated by a Creative Commons license in the record and/ or on the work itself. This Dissertation has been accepted for inclusion in WVU Graduate Theses, Dissertations, and Problem Reports collection by an authorized administrator of The Research Repository @ WVU. For more information, please contact [researchrepository@mail.wvu.edu](mailto:researchrepository@mail.wvu.edu).

# **Direct Ink Writing Printability – Ashby-like Plots for Guided Design**

**Domenic Cipollone**

**Dissertation submitted  
to the Statler College  
at West Virginia University**

**in partial fulfillment of the requirements for the degree of  
Doctor of Philosophy in  
Materials Science and Engineering**

**Konstantinos Sierros, Ph.D., Chair**

**Chih-hung Chang, Ph.D.**

**David Mebane, Ph.D.**

**Edward Sabolsky, Ph.D.**

**Charter Stinespring, Ph.D.**

**Department of Mechanical and Aerospace Engineering**

**Morgantown, West Virginia**

**2022**

**Keywords: Printability, Direct Ink Writing, Design, 3D Printing, Rheology**

**Copyright 2022 Domenic Cipollone**

# Abstract

## Direct Ink Writing Printability – Ashby-like Plots for Guided Design

**Domenic Cipollone**

Direct Ink Writing (DIW), an extrusion-based 3D printing technique, offers a broad application space. As such, the technique continues to find use in biomedical, flexible electronic, ceramic, and energy device applications, among others. With this broad application space comes an expanding material library of inks with diverse rheological and microstructural properties. This begs the question: what constitutes a printable ink? How does one define printability? And how does one design for printability?

Researchers currently have a broad understanding of what constitutes a printable ink. However, time and time again, inks with unique rheological properties and formulations are printed. Currently, ink synthesis and ink characterization for DIW take a linear analysis approach – one in which rheological and material specifications are an afterthought. To progress DIW while understanding the fundamental questions discussed above, it may be necessary to take a design approach. The design approach melds understanding of the yield stress fluid microstructure and resultant rheological properties, providing a wholistic view of the DIW fluid parameter space. Implementing design enables one to target rheological properties for a given fluid microstructure or implement new yield stress microstructures with predictable relevant rheological parameters. This ability ultimately accelerates DIW material implementation, reduces experimental time, and opens the door for novel microstructure exploration and ink development.

In this work, we explore DIW printability through a series of cases studies which involve attractive glass and repulsion dominated yield stress fluids. Through the development of a DIW rheological database, we establish the utility of Ashby-like plots in transitioning DIW to a design-based engineering approach. Through the Ashby plots and the clustering of yield stress fluid microstructures, we investigate and identify why defining the concept of printability remains elusive. Ultimately, we propose microstructurally-dependent targeted rheological parameters and demonstrate the utility of design for DIW to accelerate DIW ink implementation.

## **Erratum – Cipollone, Domenic “Direct Ink Writing Printability – Ashby-like Plots for Guided Design”. 2022.**

**Title:** Correction to: Cipollone, Domenic “Direct Ink Writing Printability – Ashby-like Plots for Guided Design” PhD Dissertation, West Virginia University. 2022.  
<https://researchrepository.wvu.edu/etd/11470/>

**Author:** Domenic Cipollone

**Abstract:** Additional citations have been added to the document and the references section updated. Additionally, numerical values within Table 15 on p. 105 have been removed to match the text.

### **Corrections:**

Page 4: A citation has been added to Figure 2a within the figure caption’s first sentence.

Page 4: A citation has been added to Figure 2b within the figure caption’s third sentence.

Page 17: A citation has been added to Figure 9a within the figure caption’s first sentence.

Page 17: A citation has been added to Figure 9b within the figure caption’s first sentence.

Page 105: Table 15 has been edited to remove the shear thinning index and critical shear rate for the 7.5 pH and 8.7 pH alumina inks. Values have been replaced with “N/A” to match the text.

Page 111: References have been updated to reflect the additions within Figure 2 and Figure 9.

## Purpose and Tone

The concept of printability in DIW remains elusive due to a lack of yield stress fluid (a.k.a. ink) understanding. A key fundamental understanding is that of the yield stress mechanism. The mechanism – repulsive or attractive – provides ‘printability’ within different rheological parameter ranges. Previous attempts to define printability take a linear analysis approach and disregard the role of fluid microstructure as related to origin of resulting yield stress. In the analysis approach, one first formulates an ink, modifies the synthesis, and evaluates ‘printability’. A typical printability evaluation involves an extrusion test and then general, but not standard, rheological characterizations. These rheological evaluations typically include steady-state rheology, oscillatory rheology, and relaxation-recovery studies. Researchers typically assess the static yield stress and the storage modulus. Acceptable values and ranges continue to vary widely.

Within DIW, evaluation of the fluid microstructure and yield stress mechanism are very little studied, considering all yield stress fluids through the same lens. However, all yield stress fluids are not the same. They can be complex, with microstructure controlling the rheological properties and thus printing output. This oversight contributes to the variance in printability definitions. This thesis aims to take a step back and begin with the fundamentals. From the fundamentals, we can define the yield stress mechanisms and then classify fluids based on their dominant microstructures and common rheological behaviors. These classifications ultimately facilitate a design approach to printability. We will express this design approach through the generation of printability Ashby-like plots and a series of case studies. Ashby-like plots will serve as reference for target rheological parameters and, in future work, help identify novel yield stress fluid microstructures.

## Contents

1	Introduction.....	1
1.1	Rapid Prototyping, Mesoscale production, customization .....	2
1.2	Direct Ink Writing.....	3
1.3	Applications for Direct Ink Writing .....	5
1.3.1	Bioprinting and Bone Scaffolds.....	5
1.3.2	Soft Robotics .....	7
1.3.3	Energy Devices .....	8
1.3.4	Ceramics.....	9
1.4	DIW Remarks.....	11
2	Yield Stress Fluids and Printability .....	11
2.1.1	Steady-State Flow Curve Models .....	12
2.1.2	Oscillatory crossover.....	14
2.1.3	Alternative Empirical Yield Stress Approximations .....	16
2.1.4	Theoretical Yield Stress Approximations.....	17
2.2	What is printability in direct ink writing? .....	19
2.3	Common Scopes of Printability – analysis approach .....	21
2.3.1	Reliable Extrusion.....	21
2.3.2	Feature Fidelity .....	23
2.3.3	Spanning and three-dimensional capability .....	25
3	Design for Direct Ink Writing .....	35
3.1	Yield Stress Fluid Classes – An Overview.....	35
3.1.1	Repulsion Dominated Yield Stress Fluids for DIW.....	36
3.1.2	Attraction Dominated Yield Stress Fluids for DIW .....	41
3.1.3	Attractive Glasses .....	42
3.2	Transitioning to DIW Design .....	43
3.2.1	Utility in Direct Ink Writing Design .....	46
3.3	DIW Ashby-like Plots.....	51
3.3.1	Storage Modulus versus Static Yield Stress.....	57
3.3.2	Shear Thinning Index versus Static Yield Stress .....	65
3.3.3	Critical Shear Rate versus Static Yield Stress .....	68
3.3.4	What other Ashby plots may be useful? .....	70
3.3.5	Additional Empirical Bounds.....	73

3.4	Conclusions.....	76
4	Repulsive Yield Stress Case studies.....	77
4.1	Introduction.....	77
4.2	Copper Ink Design.....	78
4.3	Hybrid Design Approach.....	78
4.3.1	Commentary.....	82
4.4	Design of Materials Approach.....	84
4.4.1	Problem Statement.....	84
4.4.2	The Model.....	84
4.4.3	The Selection.....	86
4.4.4	Experimental.....	89
4.4.5	Postscript.....	91
4.5	Results.....	91
5	Attractive Glass Case Study.....	93
5.1	Problem Statement.....	93
5.2	The Model.....	94
5.3	Selection.....	97
5.4	Experimental.....	98
5.4.1	Ink Synthesis .....	99
5.5	Results.....	100
5.6	Postscript.....	102
6	Contributions and Future Work.....	106
6.1	Conclusions and Contributions.....	106
6.2	Future Work.....	107
7	References.....	111

## 1 Introduction

Though gaining significant momentum in the past decade, 3D printing has a long and winding history. Most consider 3D printing a modern technology but the concept dates back nearly four decades. In 1981, Hideo Kodama polymerized a photosensitive resin with ultraviolet (UV) light, providing the world with the first stereolithography (SLA) system.<sup>1</sup> A few years later, Charles Hull, successfully filed the first SLA patent.<sup>2,3</sup> His use for the technology? Printing small, custom parts for furniture! Hull then founded the company 3D systems in 1988. Around the same year, the first patents for selective laser sintering (SLS) were filed by Carl Deckard of the University of Texas.<sup>4</sup> Most notably, Scott Crump filed the first patents for fused deposition modeling (FDM) in 1989. Instead of lasers or UV light, thermoplastic filaments were melted and printed (extruded) in a layer-by-layer fashion.<sup>5</sup> Unfortunately for the public, the FDM technology was locked as Crump's intellectual property.

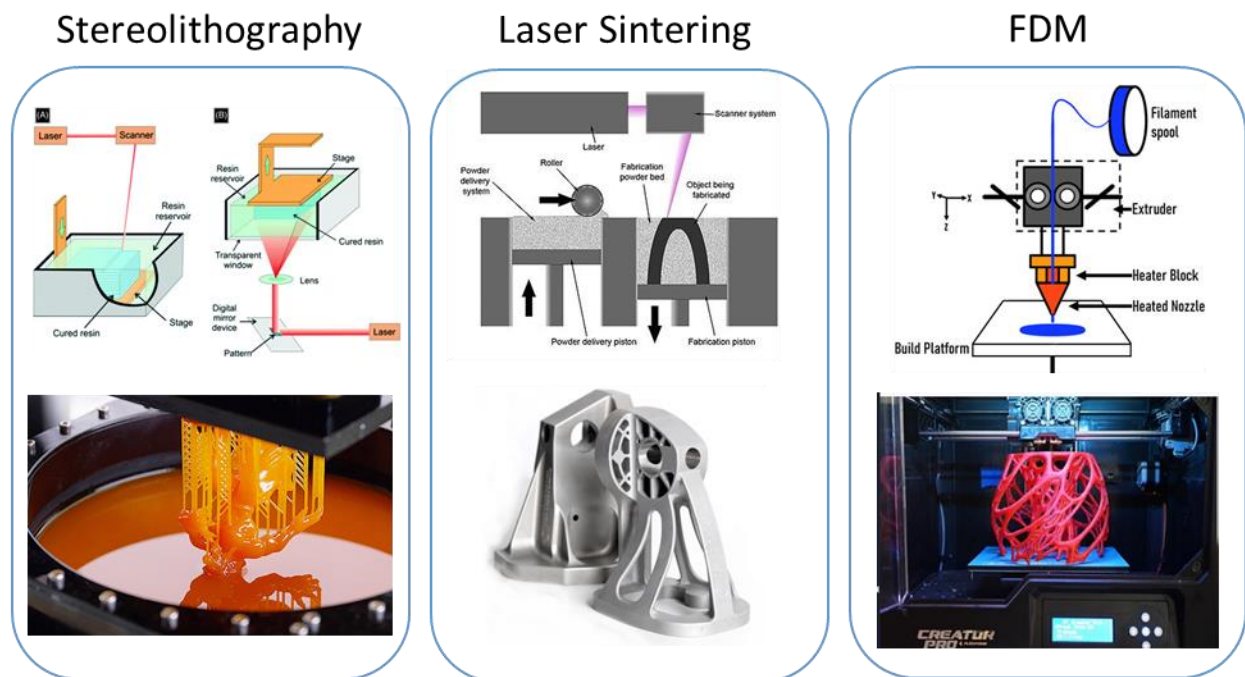


Figure 1: The foundational technologies of 3D printing: stereolithography (SLA), laser sintering (SLS), and fused-deposition modeling (FDM).



Ultimately, in 2009, the FDM patents fell into the public domain, generating the modern 3D printing boom.<sup>5</sup> 3D printers, coupled with several open-source movements such as RepRap, made their way into homes, schools, and small-businesses. The proliferation of lightweight and user-friendly CAD software further democratized the technology. Though there exist numerous 3D printing technologies, SLA, SLS and FDM constitute the 3D printing foundation (Figure 1).

### 1.1 Rapid Prototyping, Mesoscale production, customization

What are the benefits of 3D printing? The technology continues to attract significant attention, but is it living up to the hype? The strength of 3D printing lies in the ability to cost-effectively produce low volume parts (i.e., mass customization). Just as Charles Hull used his SLA technology to produce custom furniture parts, 3D printing technology (particularly FDM) helps engineers and businesses quickly prototype pre-production parts. Moreover, at low to medium volume production, also referred to as mesoscale production, 3D printing can serve as the sole production process.

In addition to filling the mesoscale niche, 3D printing enables the fabrication of previously inaccessible geometries. Complex overhangs, intricate weight saving infills, and seamless production parts are a few of the strengths of 3D printing-based manufacturing. Furthermore, as consumer products trend towards increasing customization (i.e., personalized wearables, health monitors, custom orthotics), 3D printing stands ready to meet the demand. For example, companies such as Protect3D can receive a 3D scan of an athlete's body and print, overnight, a customized athletic pad for any part of the body. Here, SLA printing enables seamless replication of the intricacies of complex body parts, such as the clavicle and thumb joint to provide comfortable and durable protection. Likewise, more traditional companies such as Xerox are pivoting from conventional 2D inkjet printing to 3D printing technologies. Their new product, spun from a fusion of inkjet, SLS, and electrohydrodynamic (e-jet) printing, enables the rapid prototyping of complex metallic parts. New printing technologies continue to develop each year, opening new business verticals, and pushing 3D printing to live up to expectations.

Of all foundational 3D printing technologies, FDM is the most ubiquitous. These systems are commonplace in countless research labs, school settings, and homes. At a basic level (Figure 1), the system heats a thermoplastic (PLA, ABS, Nylon, etc.) and extrudes the appropriately melted plastic through a nozzle. Parts are then built in a layer-by-layer fashion and require minimal post processing. In most instances, only support material needs to be removed. This technology enables small teams to work quickly, move manufacturing in-house, and become self-reliant.

However, there is a glaring limitation with FDM. The user is limited to thermoplastics.<sup>5</sup> Additionally, via material constraints, FDM is limited to printing mostly structural parts. Functional materials, such as electronic materials, stimulus responsive materials, or high-temperature ceramics remain difficult. One highly promising 3D printing technology that removes the material constraints and expands the available material library is direct ink writing (DIW).

## 1.2 Direct Ink Writing

A close cousin to FDM, DIW is an extrusion-based 3D printing technique that offers an expanded material library. *Cesarano et al.* at Sandia National Laboratories developed and demonstrated the first structural ceramic applications of DIW in 1997.<sup>6</sup> From there, DIW research has accelerated, due to its relatively lax material constraints, versatility, and ability to fabricate both three-dimensional and planar geometries. Like many additive manufacturing and 3D printing technologies, DIW utilizes computer control to fabricate geometries in a layer-by-layer process. Moreover, patterns may be designed in computer aided design (CAD) programs, sliced, and read by the printer.

However, instead of the conventional thermoplastic extruded through a heated nozzle and onto a heated bed, the DIW system consists of a syringe barrel loaded with a synthesized ink formulation, a nozzle that allows for extrusion of the ink, and an attachment for the application of pneumatic or mechanical pressure. In most cases, this ink is a viscoelastic fluid with engineered flow properties that is atmospherically deposited. However, in thin film and

unconventional applications (e.g., pressure-less printing), borderline Newtonian inks may be extruded.<sup>7,8</sup> As such, nearly any fluid one can extrude can be printed – in one form or another.

Importantly, the versatility of DIW derives from its ability to fabricate in ambient conditions, with no heat or vacuum necessary, as well as its ability to fabricate objects with little to no required post-processing. This feature allows for the synthesis of a wide-range of inks, including those containing sensitive materials such as peptides, proteins, and cells.<sup>9–11</sup> Moreover, it enables compatibility with materials featuring carefully engineered microstructures.<sup>12–14</sup>

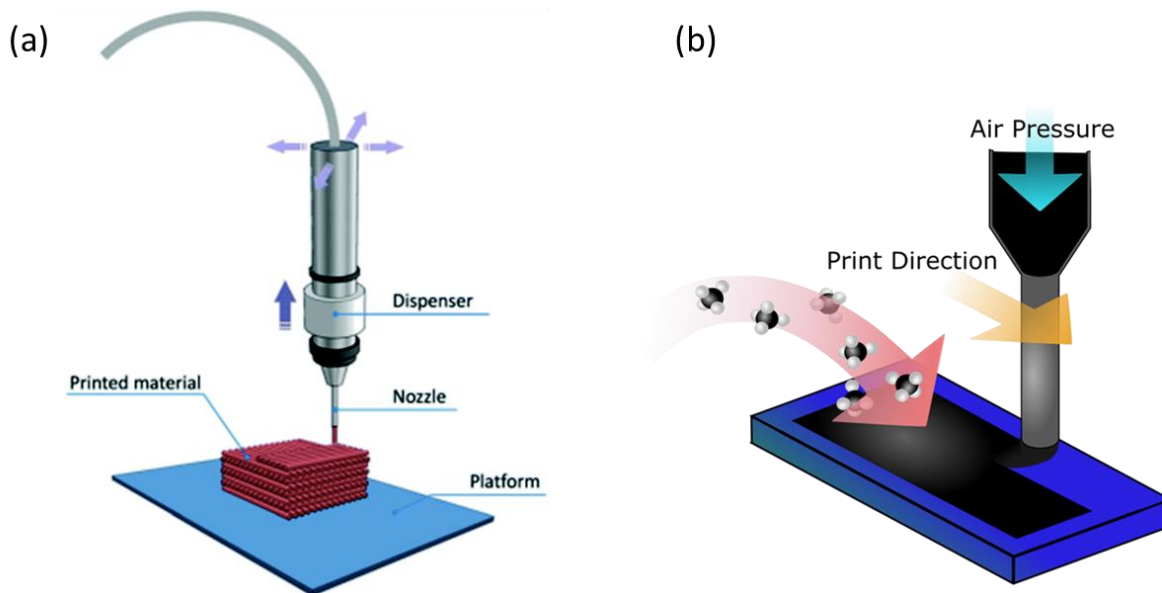


Figure 2: (a) DIW schematic detailing the printing of 3D geometries.<sup>15</sup> Pneumatic or mechanical pressure extrudes an ink through a nozzle onto a moving platform. (b) Schematic of DIW's capability to produce not only 3D geometries, but films with functional inks.<sup>16</sup>

Though there are numerous DIW processing parameters, in the simplest approach, nozzle diameter, stage velocity, and applied pressure are varied to achieve a target output. For simple applications, the target output may be a specific line width.<sup>17,18</sup> In more niche (or demanding) applications, the target output may be the maintenance of an ink's hierarchical microstructure post-extrusion.<sup>19</sup> In addition to the first order processing parameters listed in Table 1, one must consider the ink-substrate interactions. The wetting properties of the

substrate will greatly influence the ink spreading and final printed fidelity. Care should be taken to engineer the hydrophobicity or hydrophilicity of the ink to control spreading.

*Table 1: First order DIW processing parameters.*

Nozzle Speed
Nozzle Diameter
Nozzle-substrate height
Extrusion pressure
Nozzle Geometry

With the processing parameters and ink-substrate interactions in mind, the rheological properties of the ink must be tuned to facilitate reliable extrusion, spanning structures, and functional properties. Thus, the main limitation of DIW stems from the rheological properties of the inks, commonly requiring the ink to be a shear-thinning fluid (i.e., the viscosity decreases with increasing shear rate).<sup>20,21</sup> If one aims to generate complex, spanning, 3D architectures, the ink must also exhibit a well-controlled viscoelastic response, to allow flow through a nozzle, followed by a rapid ‘setting’, which ensures shape retention.<sup>22,23</sup> More information regarding ‘optimal rheological properties will be discussed within Chapters 2 and 3.

As the technology has matured, it has proven to be versatile, enabling the 3D printing of a wide range of materials at room temperature. Highlighting the versatility, this technique has been used to produce biocompatible<sup>24,25</sup>, elastomeric<sup>26,27</sup>, metallic<sup>28</sup>, and ceramic architectures.<sup>29–31</sup> To explore the application space in more detail, and more importantly, explore the diversity of ink microstructures, we conducted a series of DIW studies discussed below.

### 1.3 Applications for Direct Ink Writing

#### 1.3.1 Bioprinting and Bone Scaffolds

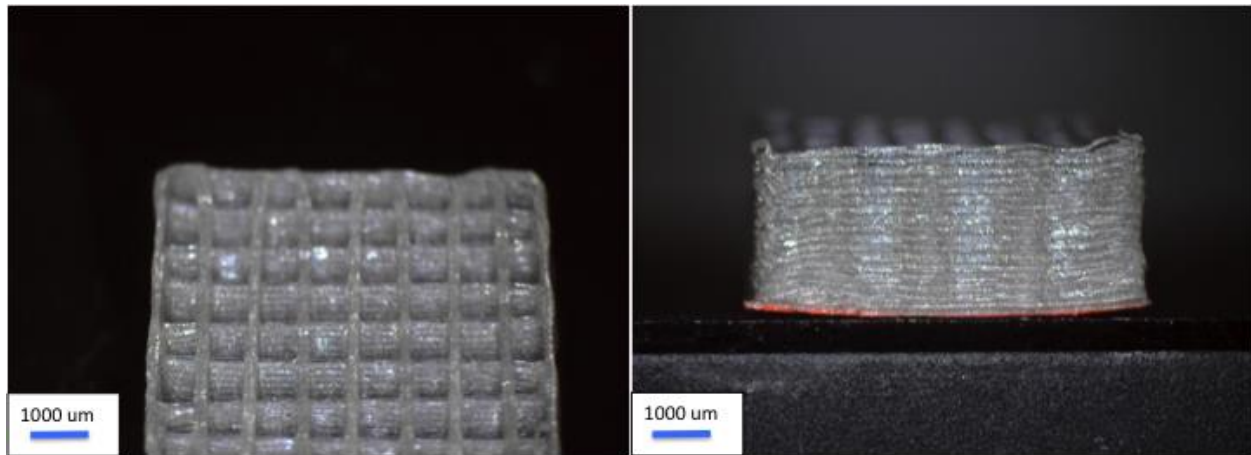
Bioprinting stands as one of the most promising application areas for DIW. The ambient processing temperatures and lack of curing medium (UV, laser, etc.) allows the facile extrusion

of sensitive materials including hydrogels, bioactive encapsulated materials, medicines, and biological cells. Nearly all organ and regenerative 3D printing efforts utilize the DIW technology. Through DIW it is possible to incorporate heterogeneous materials and synthesize composites which may promote healing or reduce inflammation. Moreover, DIW provides immense control over product geometry, allowing one to tailor both the microscopic geometry through ink design and the macroscopic geometry through the print path.

In bioprinting, polymers typically constitute the primary volume fraction.<sup>11,32</sup> For DIW purposes, the polymeric inks are generally viscoelastic and display a yield stress. What kind and which fundamental interaction(s) generate(s) the yield stress? Within polymers, chemical and physical crosslinks form from attractive interactions. Hence, most bio DIW formulations are attraction-dominated yield stress fluids. Additionally, particulate phases may be added for further functionalization. In low volume fractions, the particulate phase minimally impacts the nature of the yield stress.

As an example, we synthesized an attraction dominant yield stress fluid with a small magnesium fraction. Magnesium microparticles add an element of a jammed microstructure, but the repulsive interactions are likely not dominant. Therefore, this ink may be classified as an attraction-dominated yield stress fluid stemming from the crosslinked PLA chains. However, at higher Mg microparticle concentrations, it may transition to repulsion dominant fluid, where the yield stress and shear properties are dominated by jammed, non-interacting spheres. From this, we print bone scaffolds with various pore sizes to examine the effects of pore size and Mg wt.% on cell compatibility. The inclusion of Mg aims to enhance the biocompatibility of an otherwise bio-inert polymer. Previous work by *Cifuentes et al.* suggests the inclusion of 1% Mg in a PLA scaffold improves biocompatibility by 160%.<sup>33,34</sup>

Briefly, PLA was dissolved in dichloromethane (DCM) to form a viscous polymer solution ranging from 15-30% PLA by weight. Magnesium particles (325 mesh,  $\sim 50 \mu\text{m}$ ) were added to the PLA solution ranging from 2-5 wt.%. With this ink, a range of scaffolds were fabricated to demonstrate the utility of DIW in fabricating composite complex geometries (Figure 3).



*Figure 3: Mg-PLA composite bone scaffolds fabricated with DIW.*

### 1.3.2 Soft Robotics

Recently, numerous groups have employed direct ink writing for the manufacturing of soft robotics.<sup>26,35,36</sup> In comparison to their rigid counterparts, soft robots offer high conformability, inherent compliance, and the ability to perform delicate tasks. Conventionally, these robots are fabricated with polydimethylsiloxanes, polyurethanes, and moisture cure silicones in multi-step casting techniques.<sup>37–39</sup> These techniques are not only time consuming but tend to introduce defects via entrapped air bubbles or poor interfacial bonding, leading to reduced soft robotic life cycles.<sup>40</sup> Direct ink writing offers a one-platform alternative. Additionally, utilizing multi-material DIW, embedded sensing elements can be simultaneously deposited.<sup>36,41,42</sup>

One-part moisture cure silicones are highly compatible with direct ink writing as curing begins when exposed to moisture in the atmosphere. Moisture cure silicones feature HIGHLY attractive dominant microstructures whereby hydrolysis of Si-H and Si-N bonds which facilitate crosslinking. As such, this attractive mechanism facilitates bearing of the static load, making this an attractive yield stress fluid. To simultaneously explore DIW of purely attractive yield stress fluids and soft robotics we printed a soft robotic pneumatic network (PneuNet) using a moisture-cure silicone (GE Silicone 1). To integrate embedded sensing elements, a strain gauge was printed within the silicone elements. A conductive carbon grease (MG Chemicals 846-80G) served as the conductive material. For demonstration, the manipulator was installed on a BAXTER robot and used to manipulate a range of test geometries (Figure 4).

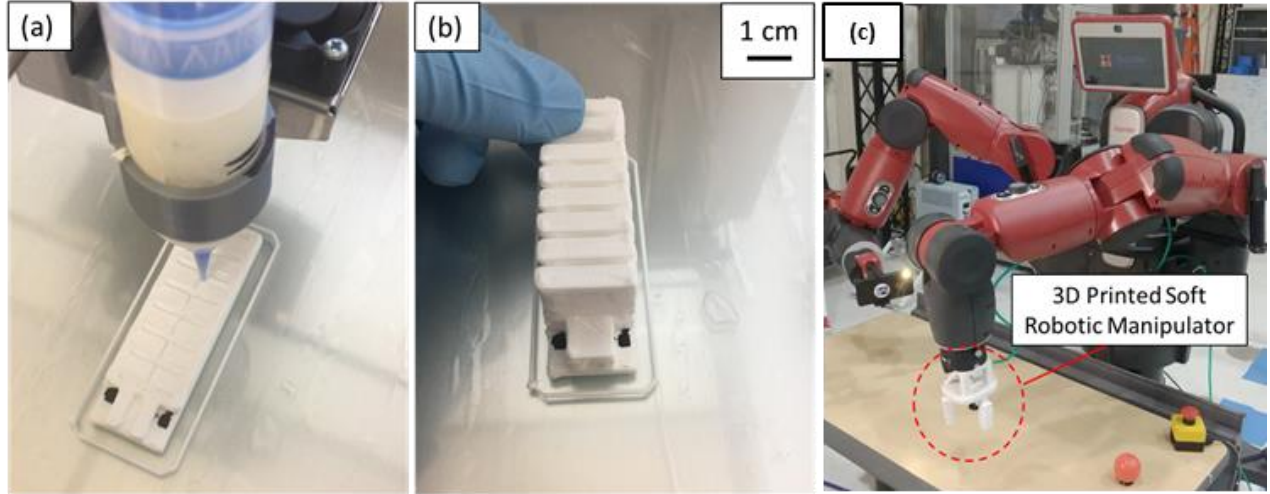


Figure 4: (a) DIW of the PneuNet with embedded strain sensor, (b) completed PneuNet, and (c) 3D printed soft robotic PneuNet used to demonstrate the ability to manipulate delicate and difficult to grasp objects.

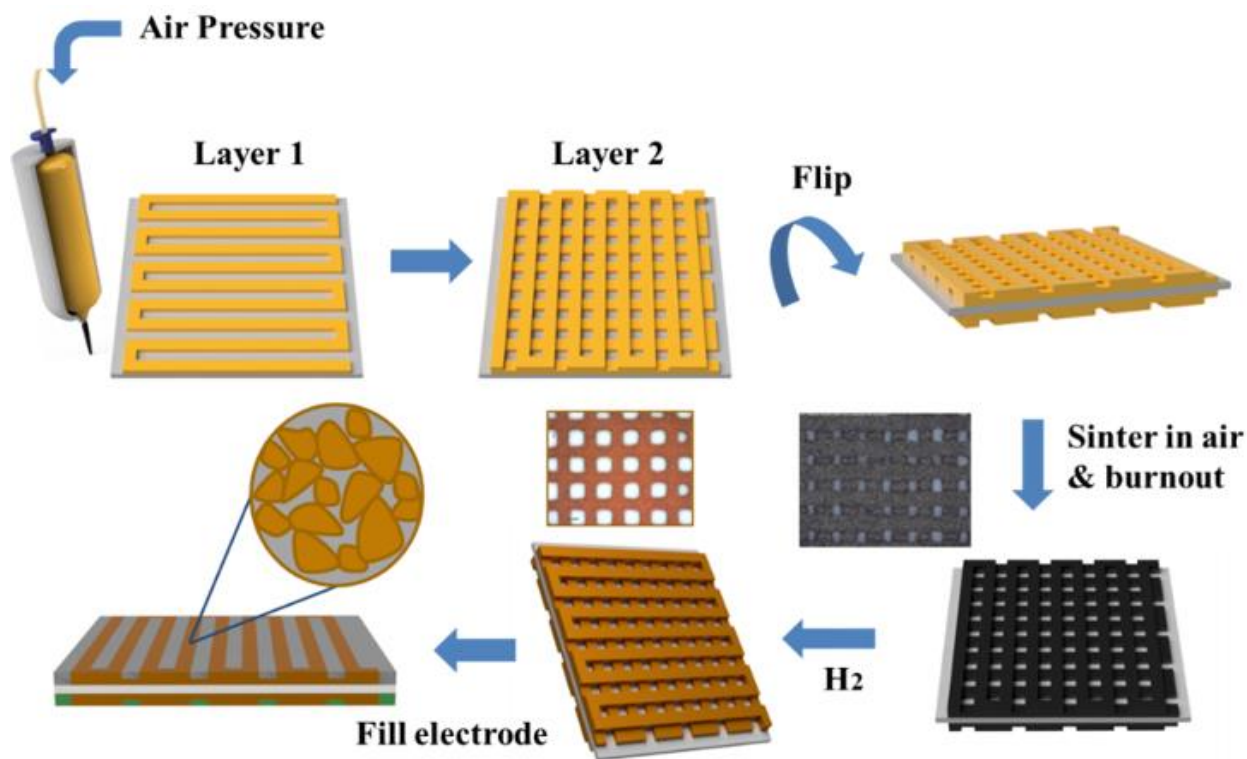
### 1.3.3 Energy Devices

Repulsion dominant yield stress fluids stand in contrast to the attractive and attraction dominant microstructures discussed in the above DIW applications. Here, high-volume fraction particulate phases of colloids or microparticles near  $\phi_{rcp}$  effectively crowd and repel one another. The particles, trapped in “cages”, arrest fluid-like motion and can bear a static load.<sup>43,44</sup>

A series of repulsion-dominated yield stress fluids consisting of an ethyl cellulose binder and 10  $\mu m$  copper particles were synthesized to serve as 3D anode scaffold in solid-state lithium metal batteries. For clarity on the yield stress fluid microstructure, the system consists of a co-solvent mixture, a polymer, and copper microparticles. The static load is borne primarily by the jammed microparticles. However, some load may be borne by the ethyl cellulose polymer matrix. As such, this yield stress fluid is classified as repulsion dominated. Solid-state batteries (SSBs), specifically lithium metal SSBs, promise higher energy density and safer electrochemical alternatives. On one hand, SSBs replace the flammable liquid electrolyte with a solid ionically conductive electrolyte. Organic solvent electrolytes suffer from inadequate thermal stability and a risk of leakage.<sup>45</sup> Therefore, significant attention has been paid to solid-state electrolytes because of their enhanced safety features and great potential in use with



lithium metal anodes.<sup>46–48</sup> Importantly, lithium metal anodes have high theoretical specific capacity (3860 mA h g<sup>-1</sup>), low density (0.534 g cm<sup>-3</sup>) and the lowest negative electrochemical potential (3.040 V vs. SHE).<sup>49</sup> Ultimately, we demonstrated the ability of DIW to enable a range of scaffold geometries and pore sizes using repulsion-dominated inks. This work swiftly explored the effects of scaffold geometry on cell and anode-electrolyte stability. An overview of the process is provided in Figure 5. Additional details of the design process can be found in Chapter 4.



*Figure 5: Schematic detailing the DIW process for patterning Cu scaffolds directly onto the LATP electrolyte. The ink is printed directly onto both sides of the electrolyte and placed in the furnace for sintering and binder burnout. The scaffolds are reduced in a hydrogen atmosphere and are then ready for infiltration of melted Li metal into the open space in the 3D copper grid as an anode.*

#### 1.3.4 Ceramics

Ceramics find use in myriad applications - specifically those involving high-temperatures. 3D printing offers the ability to rapidly prototype and manufacture complex ceramic geometries, which may be inaccessible using typical manufacturing techniques such as slip



casting. Furthermore, ceramics offer significant flexibility for ink design and engineering. The wide ranges of particle sizes, from nano to micro, provide the freedom to design colloidal, multimodal, or microparticulate inks. Importantly, multimodal ceramic distributions provide the ability to maximize the packing fraction and minimize shrinkage.<sup>50</sup> Minimizing or matching shrinkage is paramount in ceramic applications to prevent cracking and maximize compatibility with dense substrates.

To evaluate attractive glass printability within DIW, we explored the synthesis and deposition of a bimodal alumina ink for *in-situ* structural health monitoring.<sup>51</sup> The inks contain a solvent, a minimal amount of polymeric binder, nano ( $D_{50}$  0.5  $\mu m$ ) and micro ( $D_{50}$  3  $\mu m$ ) alumina particles, surfactant, and pH modifiers. Within the ink, the introduction of NaOH as a pH modifier flocculates the nanoparticles, enabling attractive forces such as Van der Waals or depletion forces to dominate. Flocculation of colloids typically results in a colloidal gel, like the PLZT and silica colloidal gels synthesized by *Smay et al.*<sup>52,53</sup> However, there is a solids volume fraction, contributing to a caging effect. Therefore, this yield stress fluid, with a small volume fraction of methylcellulose, but attractive contributions from colloids and jammed contributions from microparticles at high volume fraction may be classified as an attractive glass. Further discussion regarding attractive glasses can be found in Chapter 2.

Ultimately, utilizing our developed ceramic coaxial DIW technique, we demonstrated the ability to pattern attractive glass conductor-ceramic features. In this work, indium tin oxide inks constituted the conductive core, while the bimodal alumina ink served as the protective shell material. The inks are engineered such that the hydrophobic core ink maintains a high-fidelity interface with respect to the hydrophilic shell. Through this coaxial approach, the ink may be extruded onto both planar and rough substrates, while maintaining core continuity through the viscoelastic shell (Figure 6).

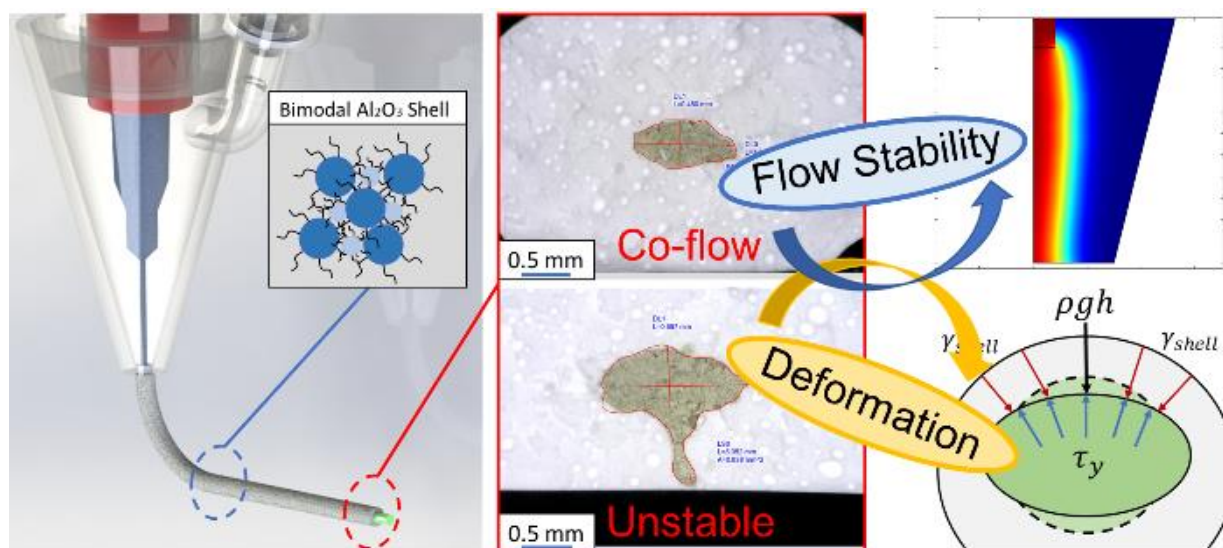


Figure 6: Coaxial ceramic DIW in which a conductive ceramic core-shell features are extruded. COMSOL flow simulations were used to analyze the processing effects on core stability. Similarly, a force balance was employed to analyze core deformations post-extrusion.<sup>51</sup>

#### 1.4 DIW Remarks

The broad application space detailed in sections 1.3.1 - 1.3.4 begs the questions: what is a printable ink? What properties unite or differentiate these materials? When engineering an ink for DIW, what design specifications does one target? It is clear one needs a shear thinning, yield stress fluid, but what yield stress is sufficient? Likewise, what combination of yield stress and degree of shear thinning is sufficient? What ranges of storage moduli, flow stresses, and static yield stress are acceptable? What yield stress fluid microstructures could one exploit to design DIW inks with different rheological properties but the same degree of printability? The following chapter explores the concept and current understanding of printability. We begin with a brief introduction to yield stress fluid characterization then pivot towards current definitions and quantifications of printability.

## 2 Yield Stress Fluids and Printability

What common characteristics do DIW compatible inks share? Within much of the direct ink writing literature, an 'optimal' ink is a shear thinning yield stress fluid. These fluids are further described as Pseudoplastic or Herschel-Bulkley fluids. Ideally, the complex fluid is a solid

at rest/low shear-stress, but quickly fluidized at a critical shear stress, referred to as the yield stress. Essentially, the ideal fluid undergoes a reversible transition from solid-like to liquid-like at a critical applied stress, flows readily through a nozzle, and then rapidly transitions once again to a solid-like material. How does one characterize a shear-thinning yield stress fluid and which metrics are targeted within the DIW field?

### 2.1.1 Steady-State Flow Curve Models

Ultimately, one can characterize yield stress fluids with steady state and oscillatory rheological measurements. Within steady state measurements, a linear or logarithmic increase in shear rate strains the material. The resultant flow stress is measured, and viscosity calculated. To characterize the fluid, many then fit rheological models to the flow curves. For yield stress fluids broadly, the Bingham plastic model is one of the most common yield stress model. The Bingham model (Equation 1) contains two parameters, the static yield stress, and the plastic viscosity:

$$\tau = \tau_y + K\dot{\gamma}$$

*Equation 1*

where  $\tau$  is the shear stress,  $\tau_y$  is the yield stress,  $K$  is the consistency index ( $Pa \cdot s$ ), and  $\dot{\gamma}$  is the shear rate.<sup>54</sup> Within the Bingham model, Newtonian flow behavior dominates upon reaching the yield stress. After yielding, the model provides a linear relationship between the shear rate and shear stress

When the post-yield behavior is non-Newtonian, a yield stress fluid may be modelled with the Herschel-Bulkley model, shown in Equation 2:

$$\tau = \tau_y + K\dot{\gamma}^n$$

*Equation 2*

where  $K$  is the consistency index ( $Pa \cdot s^n$ ),  $n$  is the shear-thinning index, and  $\tau_y$  is the yield stress.<sup>55</sup> The yield stress term within the Herschel-Bulkley equation will be the static yield stress

when fit to a flow curve with an increasing shear rate. When applied to a flow curve with a decreasing shear rate, the yield stress is the dynamic yield stress. This is a key distinction overlooked when characterizing yield stress fluids. The static yield stress is the stress required to initiate flow, while the dynamic yield stress is the stress required to keep the fluid flowing. Importantly,  $K$  possesses units of  $Pa \cdot s^n$ , where  $n$  is the shear-thinning index. As such  $K$  is dependent on  $n$  and cannot be used in its native form as a transferable metric. Instead, several authors, such as *Nelson* and *Jaworski*, have used a ‘critical shear rate’ to replace  $K$ , shown in a modified version of the Herschel-Bulkley equation (Equation 3):<sup>56,57</sup>

$$\tau = \tau_y \left[ 1 + \left( \frac{\dot{\gamma}}{\dot{\gamma}_c} \right)^n \right]$$

Equation 3

One can convert from  $K$  to  $\dot{\gamma}_{critical}$  using Equation 4:

$$\dot{\gamma}_{critical} = \left( \frac{\tau_y}{K} \right)^{1/n}$$

Equation 4

Hence, when  $\dot{\gamma}_c = \dot{\gamma}$ , the flow stress is twice that of the yield stress. Roughly, this stress translates to the stress at which the viscous forces dominate the shear properties and the material exhibits fluid like behavior.

Within DIW, as most target shear-thinning behavior, the Herschel-Bulkley model is typically applied. However, the power-law model is occasionally erroneously applied even when describing yield stress fluids:

$$\tau = K\dot{\gamma}^n$$

Equation 5

The Power Law model is identical to the Herschel-Bulkley except for the lack of a yield stress term. Commonly, the Power law model is not valid at low and high shear rates and is valid only

between shear rates of 10 – 100 1/s. Thus, the Power Law model may not capture the shear rates experienced by a DIW ink under extrusion and does not incorporate a yield stress term.<sup>21</sup>

Figure 7 provides a comparison of the common DIW rheological models and their general behavior.

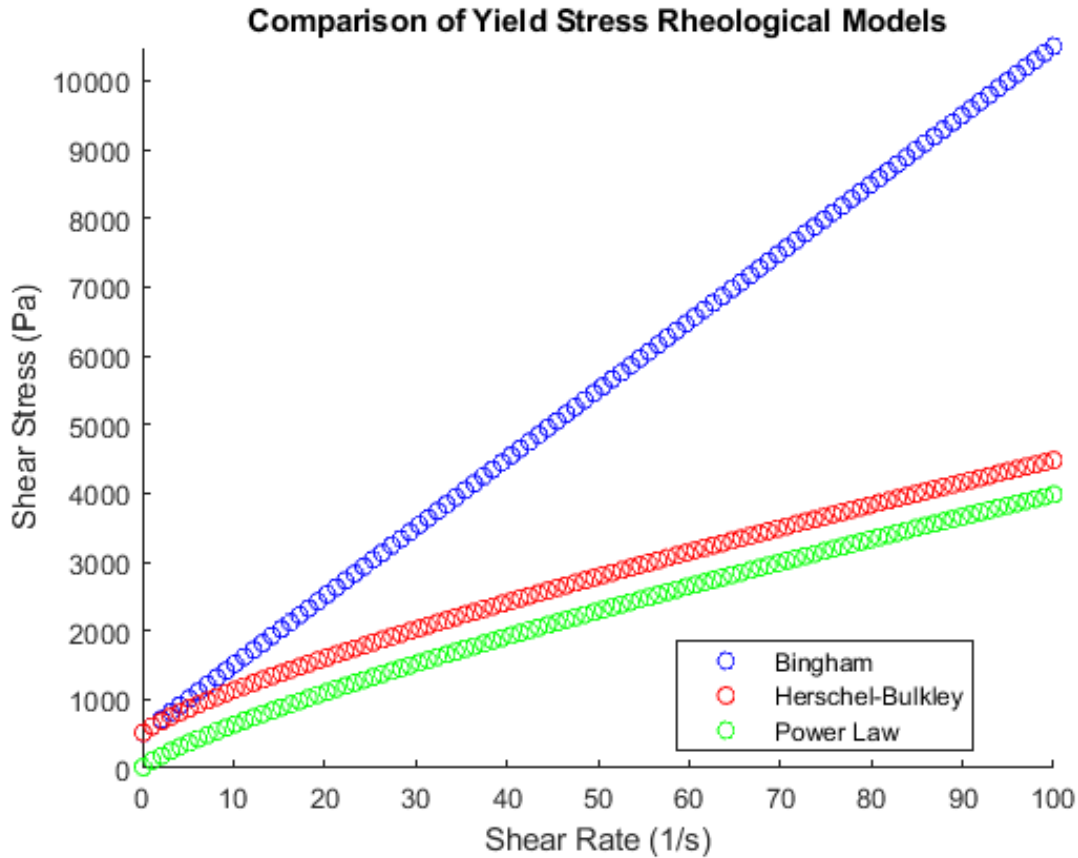


Figure 7: Comparison of the Bingham, Herschel-Bulkley, and Power Law rheological models.

### 2.1.2 Oscillatory crossover

The ink's viscoelastic properties may further be characterized through oscillatory rheology. Typically, a small volume of fluid is placed between parallel plates. Then, a sinusoidal strain is applied with varying amplitude. Likewise, the strain amplitude may be fixed, and the oscillatory frequency varied. From these tests, the complex shear modulus may be obtained as a function of stress or strain, depending on the operating mode of the rheometer (Equation 6):

$$G^* = G' + iG''$$

Equation 6

where  $G^*$  is the complex shear modulus,  $G'$  is the storage modulus, and  $G''$  is the loss modulus.<sup>58</sup>

$$G' = G^* \cos (\delta)$$

Equation 7

$$G'' = G^* \sin (\delta)$$

Equation 8

Here,  $\delta$  is the phase angle, or angle describing the shift in a material response following an applied stress or strain.

In the DIW literature, the storage modulus ( $G'$ ) is typically interpreted as the 'stiffness' of the ink.<sup>53,59</sup> In a common oscillatory measurement known as an amplitude sweep, the stress or strain amplitude is increased, while the oscillation frequency is held constant. From this measurement technique, distinct changes in the storage and loss modulus can be observed (Figure 8). Regions in which  $G' > G''$  signal solid-like behavior. Moreover, through analysis of the variation of  $G'$ , the linear viscoelastic region (*LVR*) may be defined. Within this region the ink elastically deforms. Eventually, the stress or strain will exceed the static yield stress,  $\tau_y^{static}$ , and begin to flow. As the amplitude increases, a crossover point will be reached where  $G'' > G'$ , and the ink begins to exhibit dominant viscous or fluid like behavior. This crossover point is interpreted by many as the flow stress, though some continue to interpret this point as the yield stress. In practice, the fluid has been stressed well beyond the linear viscoelastic region. Given time, the fluid will regain some percent of the original elastic properties.

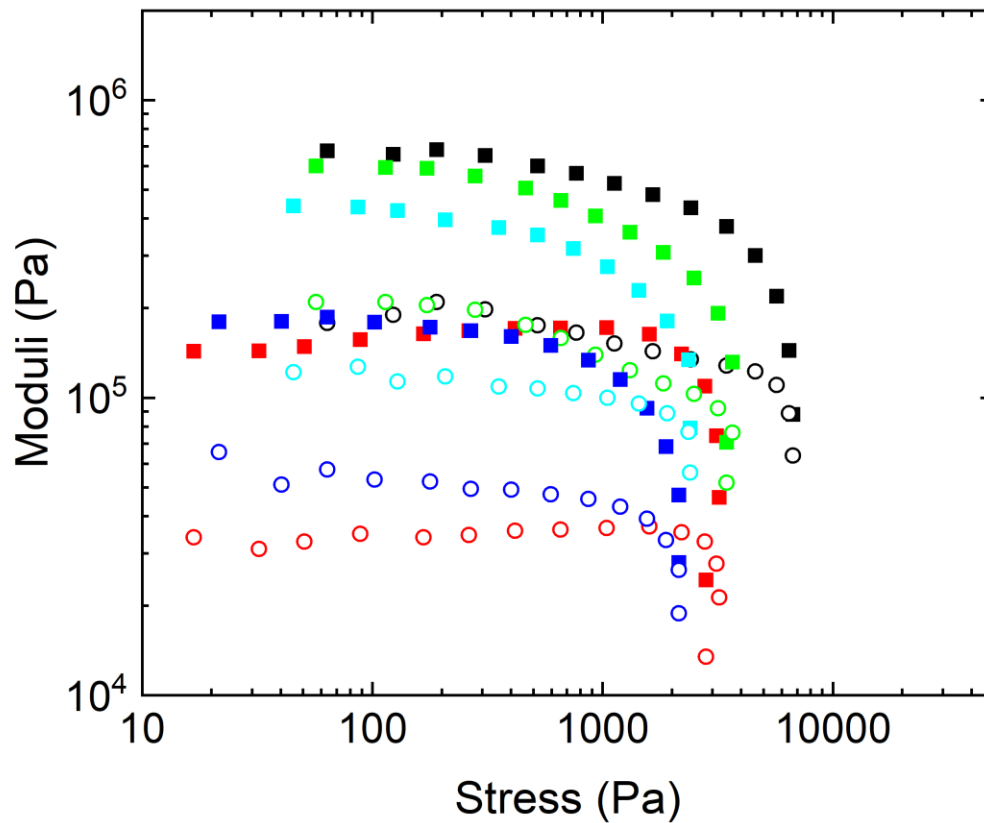


Figure 8: Shear moduli characterization for a range of copper inks.  $G'$ : solid squares,  $G''$ : hollow circles.<sup>18</sup>

### 2.1.3 Alternative Empirical Yield Stress Approximations

In addition to the methods described above, the yield stress is often approximated through various fits of the oscillatory curves. Some of the methods include: viscosity decrease steady stress sweep method, the oscillatory tangential intersection method, and the  $G'$ - $G''$  crossover (Figure 9). All give varying measures of the yield stress, and some such as the  $G'$ - $G''$  crossover are interchanged with the 'flow stress'.

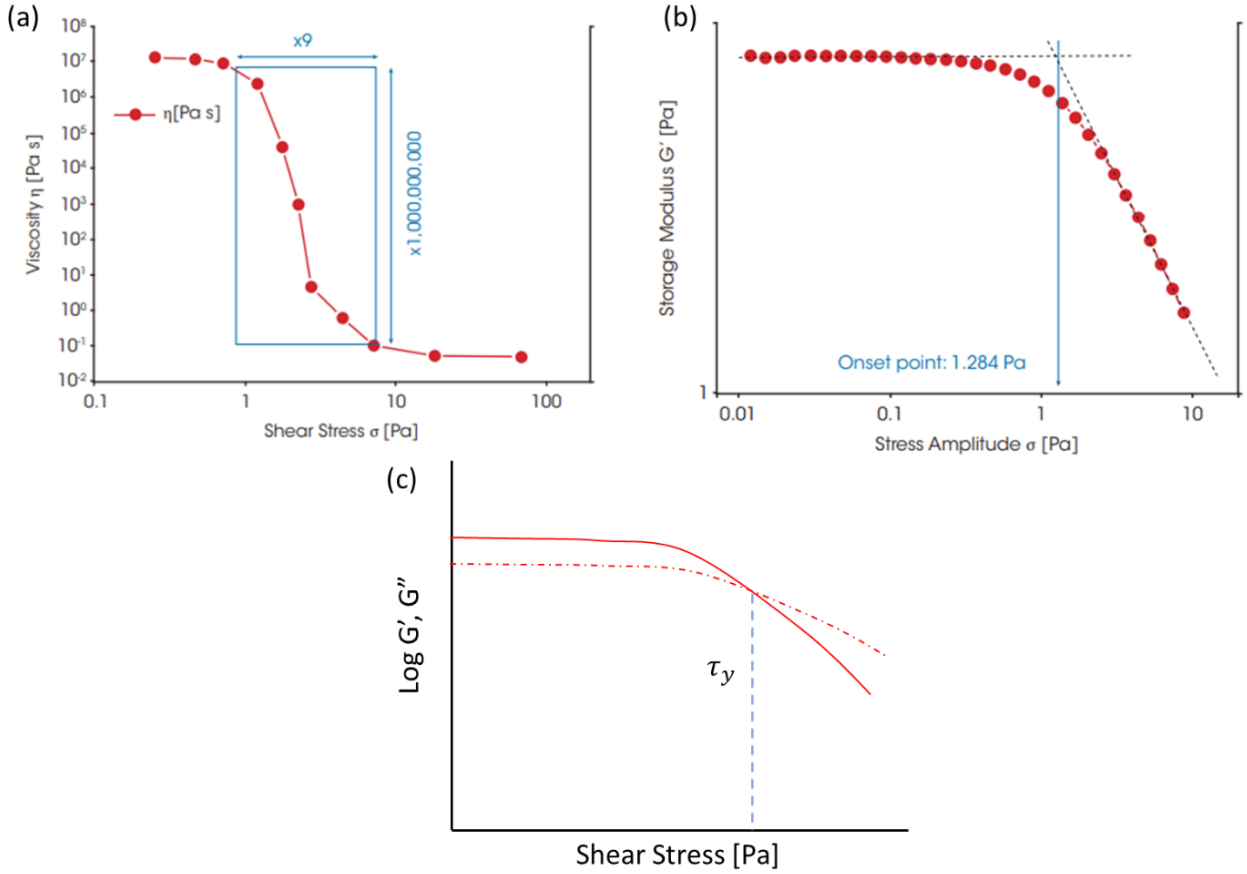


Figure 9: Various methods of yield stress measurement: (a) viscosity decrease stress sweep<sup>60</sup>, (b) oscillatory tangential intersection<sup>61</sup>, and (c)  $G'$ - $G''$  crossover. The  $G'$ - $G''$  crossover point is frequently referred to as the flow stress.

#### 2.1.4 Theoretical Yield Stress Approximations

In addition to empirical yield stress approximations, several theoretical models have been developed to approximate the yield stress for a range of yield stress fluids. Yield stress fluids include attractive polymers, colloidal fluids, and composites.<sup>62–64</sup> Additionally, electro and magnetorheological fluids demonstrate finite yield stresses in the presence of an external field.<sup>65</sup> Generally, for particulate systems, the yield stress increases according to a power law.<sup>66</sup> Likewise, there exists some critical volume fraction,  $\Phi_c$ , which results in a finite yield stress. This volume fraction varies depending on the fluid microstructure and interparticle attractive potential. For example, in non-Brownian (non-colloidal) repulsive yield stress fluids, the yield stress arises at a jammed volume fraction.<sup>44,67</sup> However, for colloidal repulsive spheres, the



yield stress arises at a smaller volume fraction due to the presence of thermal vibrations. The following sections provide a brief description of theoretical yield stress approximations for hard sphere inks and particulate gels.

#### 2.1.4.1 Colloidal Glasses and Hard Spheres

One observes a finite yield stress in inks of colloidal glasses and hard spheres upon realizing a critical volume fraction. This volume fraction marks the point at which the rheological properties (viscosity included) are dominated by the properties of the solid phase. For athermal non-Brownian particles, the interactions are physical, arresting the structure.

*Cates et al.* provide a model for the yield stress estimation of jammed microstructures, above a critical volume fraction (Equation 9):<sup>68</sup>

$$\tau_y = \tau_c + 112\sqrt{\Phi - \Phi_c}$$

Equation 9

where  $\Phi$  is the particulate volume fraction,  $\Phi_c$  is the critical volume fraction,  $\tau_c$  is the critical yield stress, and  $\tau_y$  is the yield stress. Here, the equation is valid when  $\Phi > \Phi_c$ .

#### 2.1.4.2 Particulate gels

Model particulate gels include monodisperse polystyrene spheres with attractive forces modulated by the addition of surfactant. For these systems, the yield stress corresponds to the maximum force per unit area that the network can withstand before rupturing. This force is proportional to the maximum force acting between each pair multiplied by the number of bonds per unit area. In this case, though, one assumes that yielding requires the rupture of only one bond per particle, so that:

$$\tau_y \sim \frac{\Phi^2}{\alpha^2} W'_{max}$$

Equation 10

where  $\tau_y$  is the yield stress,  $\Phi$  is the particulate volume fraction,  $\alpha$  is the particle radius, and  $W'_{max}$  is the maximum spatial gradient of the interaction potential. This equation is valid for  $\Phi < 0.64$ , the close random packing fraction maximum for spheres. When  $\Phi > 0.64$ , the fluid may transition to a repulsion dominated jammed microstructure (repulsive glass). One can see that within particulate gel systems the yield stress is proportional to the square of the volume fraction, and inversely proportional to the square of the particle radius. Likewise, the yield stress scales linearly with the interaction potential. Hence, surface charge induced flocculation is an effective strategy to tailor the yield stress within colloidal gels. Such methods were used within the alumina coaxial system to tailor the yield stress several orders of magnitude.<sup>51</sup>

#### 2.1.4.3 Additional Theoretical Yield Stress Approximations

Beyond colloidal glasses and gels, the yield stresses of emulsions, foams, electrorheological fluids, and others may be theoretically approximated. I refer readers to *Nelson et al.*'s table summarizing scaling relationships for other yield stress fluid microstructures (Table 2).<sup>57,69</sup>

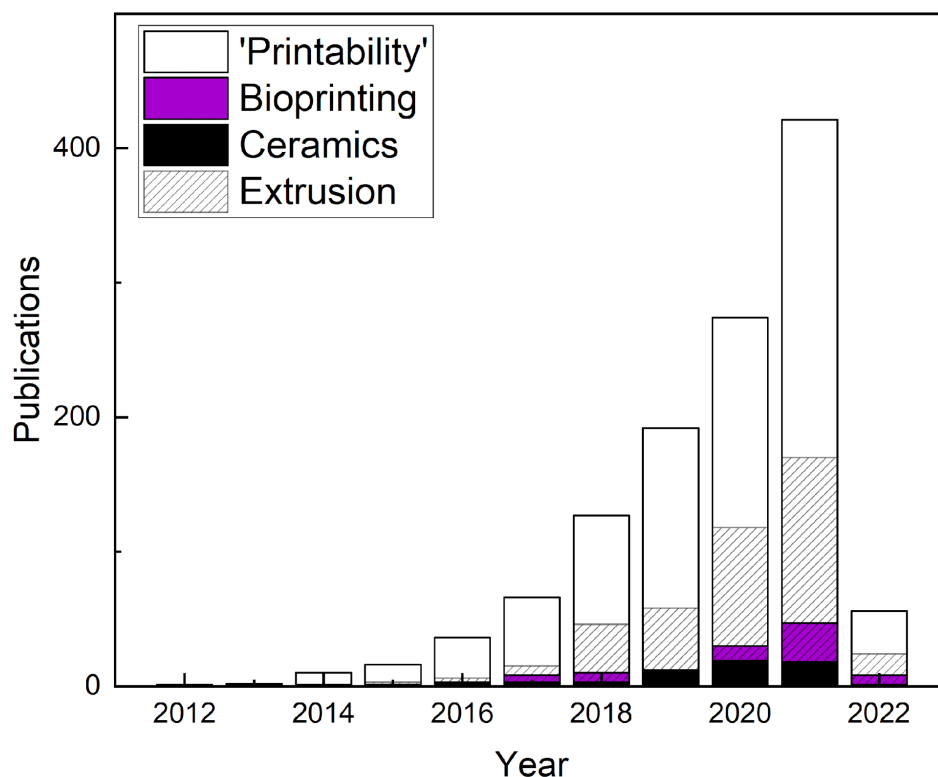
*Table 2: Theoretical yield stress scaling relationships for various yield stress fluid classes.*

Material class	Scaling relationship	(Eqn #)	Notes
Hard spheres <sup>87</sup>	$\sigma_Y = \sigma_{\text{Crit}} + 112\sqrt{\phi - \phi_{\text{Crit}}}$	(1)	$\phi > \phi_{\text{Crit}}$
Charged particles <sup>88</sup>	$\sigma_Y \approx K \left( \frac{W(r_m) - k_B T}{(r_m/2)^3} \right)$	(2)	$r_m < d_{\text{eff}}$ $K = \text{constant}$
Soft particles <sup>61</sup>	See reference		
Emulsions and foams <sup>57</sup>	$\sigma_Y = \frac{\Gamma}{R_{\text{mean}}} \phi^{\frac{1}{3}} Y(\phi)$	(3)	$\phi > 0.9069$
Particulate gels <sup>89</sup>	$\sigma_Y \sim \frac{\phi^2}{a^2} W'_{\text{max}}$	(4)	$\phi < 0.64$
Electrorheological fluids <sup>78</sup>	$\sigma_Y \sim \phi \epsilon_0 \epsilon_s \beta^2 E^2 f_{\text{max}}$	(5)	
Magnetorheological fluids <sup>80</sup>	$\sigma_Y \sim H^2$	(6)	Low field strength
	$\sigma_Y = \sqrt{6} \phi \mu_0 M_S^{1/2} H^{3/2}$	(7)	Intermediate field strength
	$\sigma_Y^{\text{Sat}} = 0.086 \phi \mu_0 M_S^2$	(8)	Fully-saturated induced dipoles

## 2.2 What is printability in direct ink writing?

Ultimately, from the broad application space demonstrated in Chapter 1, DIW holds promise as a manufacturing technique. The material library of DIW suits numerous applications needs and enables robust design freedom. Despite advancements, progress is still needed to

drive 3D printing beyond its established role as a rapid prototyping technology and expand its application in scalable manufacturing of functional materials and structures. DIW maturation will be assisted by: (1) the development of new high-performance inks, and (2) a complete understanding of the material and process-properties relationships that drive the printing process. These governing material and process-properties relationships form the basis of 'printability'. Interest in the concept of printability continues to grow across the DIW community, as shown in Figure 10.



*Figure 10: Printability by year. Sub Sections of the bar graph represent articles published for field specific printability, with bioprinting and ceramic applications growing.*

From bioprinting to ceramics printing, researchers attempt to determine ranges of rheological, formulation, and DIW processing parameters. However, the current analysis-based method of modifying inks and optimizing process parameters is limited. Inks are certainly synthesized with an application in mind and must be printable – *but what does that mean?* In some instances, a printable ink implies the capability to print a 200  $\mu\text{m}$  feature and span a 500

$\mu\text{m}$  gap. In a thin film application, a printable ink may be one in which the surface roughness is controllable. In bioprinting applications, printability may equate to cell survival, which is a function of the ink's rheological properties and the associated maximum shear stress. Consequently, the scope of printability is broad, with printability remaining globally undefined, subjective, and application dependent. Irrespective of niche objectives, three basic scopes of printability prevail broadly across the DIW community:

1. Reliable extrusion
2. Feature Fidelity
3. Spanning and three-dimensional capability

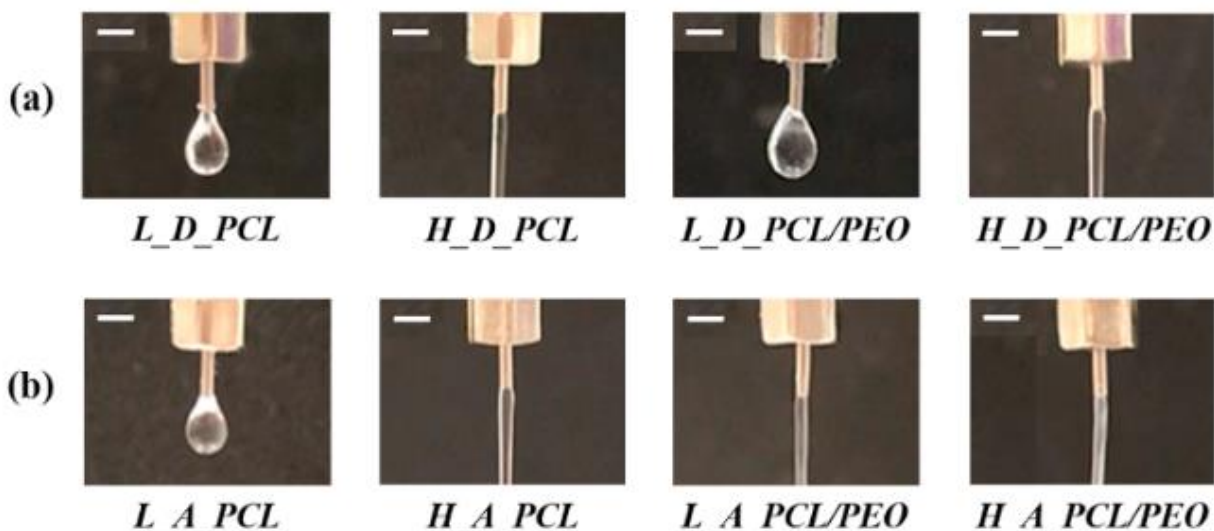
The following sections briefly discuss the three basic printability scopes. Within each section, the analysis-based approach is highlighted with examples from literature. Ultimately, the analysis approach results in ink formulations with significantly different rheological properties and microstructures. However, all these inks are 'printable'. What aspect of characterization is potentially missing? What further ink information, from a design standpoint, may researchers be overlooking?

## 2.3 Common Scopes of Printability – analysis approach

### 2.3.1 Reliable Extrusion

The most immediate scope of printability involves reliable extrusion (i.e., can the ink flow through the nozzle and extrude as a filament?). Extrudability can be defined as the ability of an ink to obtain a target flow rate. This flow rate is a function of the shear-thinning properties and nozzle geometry. However, researchers tend to task themselves with formulating an ink that achieves a qualitative metric such as limited clogging or 'controllable' extrusion through a nozzle. The analysis of extrudability is typically coupled with an exploration of processing parameters, such as nozzle diameter, printing speed, or applied pressure. For example, *Muth et al.* generated an extrusion processing map for an alumina emulsion based upon the nozzle diameter and printing speed.<sup>59</sup> From this exploration, they define regions that produce 'stable printing' or 'clogging'. Likewise, *Zhang et al.* performed extrusion tests for a

series of attraction dominant inks. Here, they observe which formulations form droplets, and which form filaments (Figure 11).<sup>70</sup>



*Figure 11: Extrusion printability assessments of various polycaprolactone formulations. Acceptable extrudability occurs when the formulation extrudes as a filament instead of a droplet.*<sup>70</sup>

Generally, formulations will be tweaked to analyze the impact on the rheological properties. However, an ink capable of extrusion can still be a long way from application compatibility. For example, an extrudable fluid could possess an inadequate static yield stress, rendering it incapable of supporting layer-by-layer printing. Likewise, the extrudable fluid could possess an inadequate storage modulus, and thus be incapable of spanning even small gaps. In this case, 2 of the 3 printability qualifications are not met. Moreover, the work to find a reliably extrudable ink is performed through experimental trial and error, or with the guidance of an experienced chemist/engineer, adding layers of analysis to ink engineering. For example, *Dolganov et al.* analyzed the impacts of titania, solvent, and polymer weight ratios on ink extrudability through a 0.5 mm nozzle for a series of repulsion dominant inks (Figure 12).<sup>71</sup> Their goal was to synthesize a titania ink which was self-supporting and controllably extrudable. In their analysis-based methodology, a range of inks are synthesized, varying the titania weight ratio, as well as modifying the polymers and surfactants (i.e., switching between polyvinyl alcohol and polyethylene glycol).


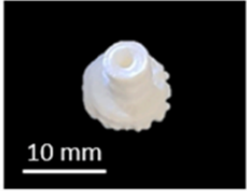
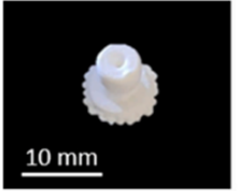
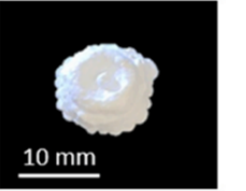
The 3D model of the investigated rivet:  	The weight ratio of TiO <sub>2</sub> :H <sub>2</sub> O		
	1:0.8	1:0.9	1:1
	Unextrudable	Unextrudable	Unextrudable
	The weight ratio of TiO <sub>2</sub> :H <sub>2</sub> O:PEG		
	1:0.8:0.1	1:0.9:0.1	1:1:0.1
	Controllably extrudable	Controllably extrudable	Extrudable with occasional inconsistencies
			
	10 mm	10 mm	10 mm
	The weight ratio of TiO <sub>2</sub> :H <sub>2</sub> O:PVA		
	1:0.8:0.05	1:0.9:0.05	1:1:0.05
	Uncontrollably extrudable	Uncontrollably extrudable	Uncontrollably extrudable

Figure 12: Extrudability exploration for a series of titania inks. Solids loading and polymer content are varied and analyzed to synthesize a printable ink.<sup>71</sup>

A series of rheological tests were then performed to evaluate shear thinning behavior. Most characterized inks were shear-thinning, though some were entirely non-extrudable and others uncontrollably extrudable. Unfortunately, the flow curves were not fit with any rheological models, and the flow curves only visually inspected. Quantitative descriptions of the systems, such as the yield stress, shear-thinning index, consistency index, storage modulus, and critical shear rate were not noted. Furthermore, no design specifications, such as target height, line width, or spanning distance were stated. How tall did the structure need to be? What static and dynamic yield stress were needed to support the structure? Optimization objectives and design constraints can help guide discussions of printability. Ultimately, the analysis approach taken by Dolganov is the approach of most DIW work to date.

### 2.3.2 Feature Fidelity

The next scope of printability is feature fidelity – where the final dimensions of the DIW geometry must match those designed in a CAD or slicer software. Extrudability – the ability to

achieve a target minimum flow rate – and print fidelity are intimately linked. Typically, addressing printability through feature fidelity is the most pragmatic course one can take, especially when limited to a single material in the case of most research experiments. Commonly, an ink is synthesized and experimental processing maps generated to achieve a target output.

In these instances of a single material, one optimizes feature fidelity through parametric studies of the printing parameters – nozzle height, nozzle diameter, printing speed, and applied pressure (i.e., first order processing parameters). Some combination of these parameters, achieved through trial and error, are likely to result in a feature close to the desired fidelity. For example, in our previous work designing copper inks for DIW, processing maps were developed to relate the feature width nozzle diameter, applied pressure, and printing speed (Figure 13).<sup>18</sup>

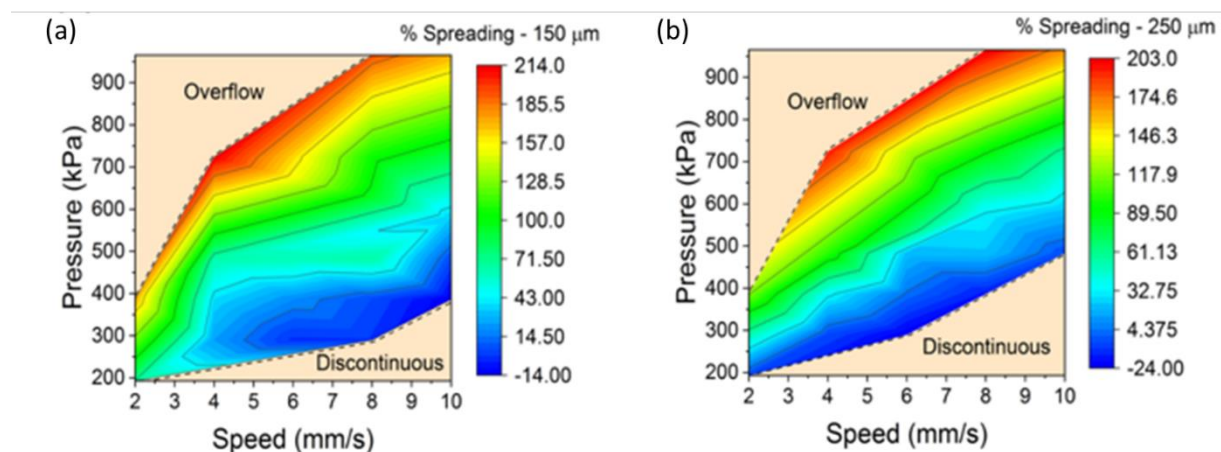


Figure 13: (a) Processing map for a 200-um nozzle with a 150-um distance to substrate and (b) a processing map for a 200-um nozzle and 250-um distance to substrate.<sup>18</sup>

Likewise, in previous work, *Torres et al.* synthesized a range of printable titania inks aimed at patterning thin films for photocatalytic applications.<sup>8</sup> Specifically, they aimed to pattern titania thin films compatible with low-temperature substrates. In their work, surfactant type, surfactant quantity, and solids loading were varied to tailor the inks' wetting properties and extrudability. Ultimately, several processing maps were developed which relate the printing fidelity with extrusion pressure and printing speed. Areas of overflow, no extrusion, and



discontinuous features are displayed. Additionally, the maps serve to target specific spreading regimes for given combinations of speed and pressure.

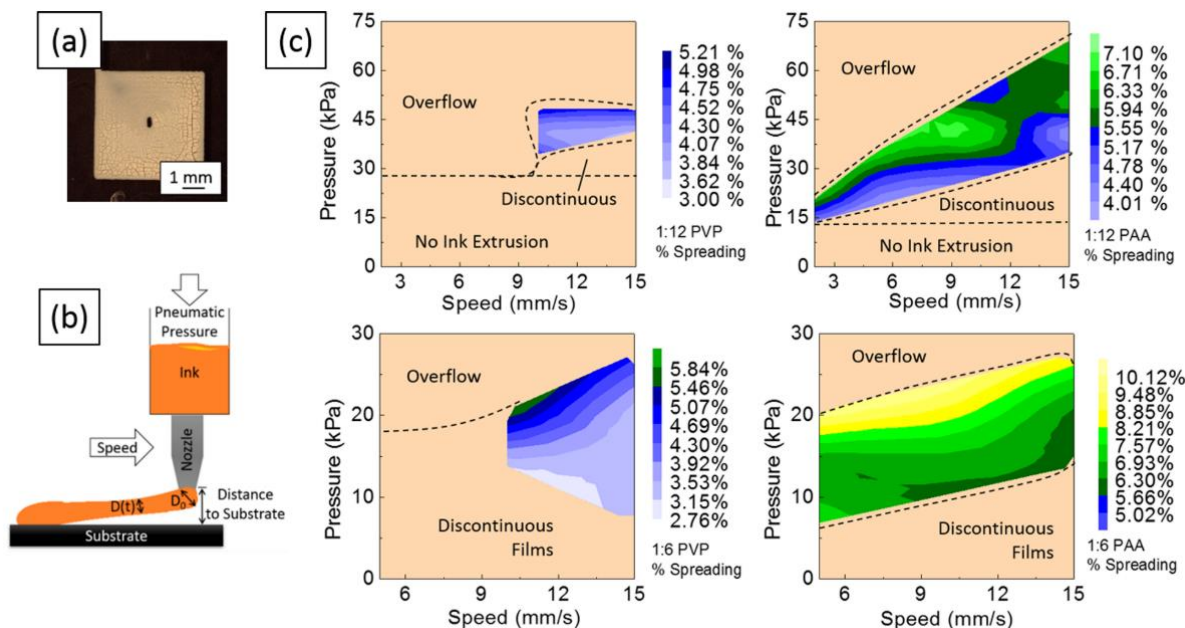


Figure 14: Titania ink processing overview and processing maps developed for thin film printing. (a) Printed dye-sensitized anode, (b) DIW schematic and (c) processing maps for a titania ink formulations with polyvinylpyrrolidone (PVP) and poly-acrylic acid (PAA).<sup>8</sup>

### 2.3.3 Spanning and three-dimensional capability

One of the most promising analytical printability approaches focuses on developing rheological specifications for spanning and three-dimensional capability. The literature efforts focus both on colloidal gels (attraction dominated inks) and emulsions (repulsion dominated inks). However, no explicit microstructural classification is provided by the authors. Generally, in addition to reliable extrusion and high fidelity, the most common definition of printability continues to be the ability to print defect free spanning and three-dimensional structures. The printability of inks as it relates to spanning and 3D structures has mostly aimed to be defined with workable ranges of rheological parameters. These parameters frequently include the components of the complex shear modulus ( $G'$  and  $G''$ ), dynamic and static yield stress, shear-thinning index, and time dependent recovery metrics such as the recovered storage modulus ( $G'_{recovered}$ ).<sup>53,72</sup> Printability in spanning and 3D geometries is commonly defined as an ink



capable of spanning a given gap with a defined minimum deflection. Similar, but slightly different printability criteria aim to achieve some percent of the theoretical/as-designed cross-sectional area which demonstrates minimal ink slumping. Ultimately, in these approaches, ink engineering becomes an optimization problem, a topic which will be explored in detail in Chapters 3-5. Briefly, given one desires a shear thinning yield stress fluid, the primary design variables could be:

*Table 3: Primary design variables for a DIW ink.*

Static yield stress
Dynamic yield stress
Storage modulus
Shear thinning index

These variables are obtainable through the steady-state and oscillatory rheological characterizations described in previous sections. The following sections describe prominent attempts at devising target specifications for the primary design objectives in Table 3. However, as we will see, significant disagreement remains. We will eventually attribute the disagreements to a lack of distinction in the yield stress fluid microstructure and yield stress mechanism.

*Smay et al.* published one of the seminal inequalities relating the inks' rheological properties to slumping and spanning behavior.<sup>53</sup> In this work, Smay applies a simple beam bending model to a colloidal gel, attraction dominated fluid:

$$G'_{LVR} \geq 1.4\rho^*s^4D$$

*Equation 11*

Above,  $G'_{LVR}$  is the ink stiffness (storage modulus in the linear viscoelastic region, LVR),  $\rho^*$  is the specific weight of the ink,  $s$  is the reduced span distance ( $L/D$ ),  $L$  is the distance between the

center of adjacent filaments, and  $D$  is the filament diameter. When applied to a colloidal silica ink, the metric was capable of reasonably predicting the spanning behavior.<sup>53</sup>

Similarly, *M'Barki et al.* used a fundamental approach to define the printability and slumping of ceramic boehmite pastes.<sup>73</sup> Due to the relatively low volume fraction, the inks may be classified as a colloidal gel. Higher volume fractions, coupled with the moderate attractive potential (induced through charge screening or polyelectrolytes), could transition the inks to an attractive glass. An analysis of the forces acting on the printed system resulted in Equation 12, which helped guide their ink development:

$$\tau_y^{dyn} \geq \gamma D^{-1} + \rho g h$$

Equation 12

where  $\tau_y^{dyn}$  is the dynamic yield stress,  $\gamma$  is the suspension's surface tension,  $D$  is the filament diameter,  $\rho$  is the fluid density,  $g$  is the acceleration due to gravity, and  $h$  is the printed structure's height. A simple rearrangement of Equation 12 provides a dimensionless quantity,  $\mathcal{E}$ .

$$\mathcal{E} = \frac{\tau_y^{dyn}}{\gamma R^{-1} + \rho g h}$$

Equation 13

The dimensionless number  $\mathcal{E}$  describes the ratio of the competing forces and parameters which influence slumping and deformation after exiting the nozzle, which can be seen in the force diagram below (Figure 15). Using  $\mathcal{E}$ , the group was able to refine the ink synthesis process and produce inks with targeted dynamic yield stresses which minimize slumping. Inks which possessed a  $\mathcal{E} > 1$  were more resistant to slumping, as the dynamic yield stress could adequately resist the combined inward pull of gravity and capillary forces. As was discussed, this metric proved useful in describing the slumping of both clay suspensions but did leave room for improvement.

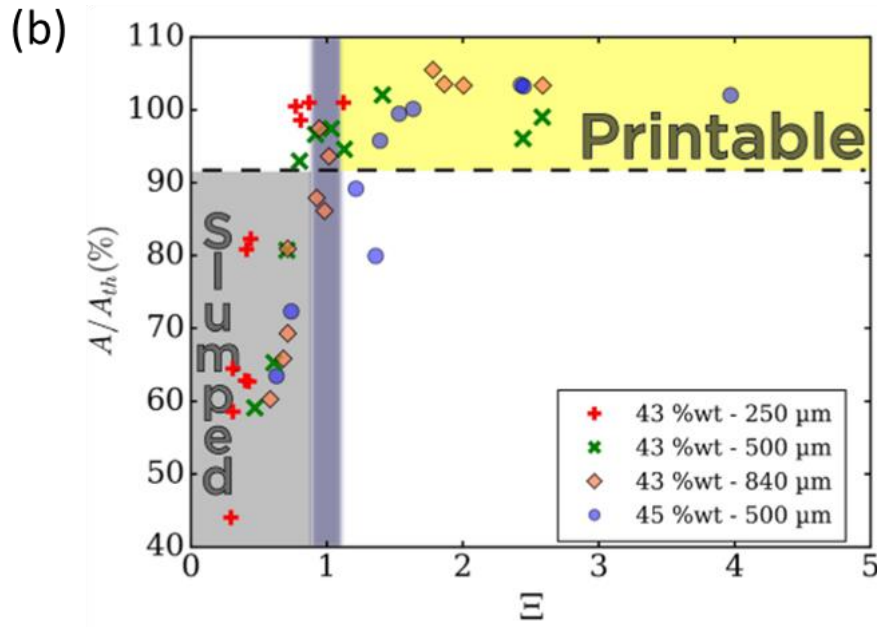
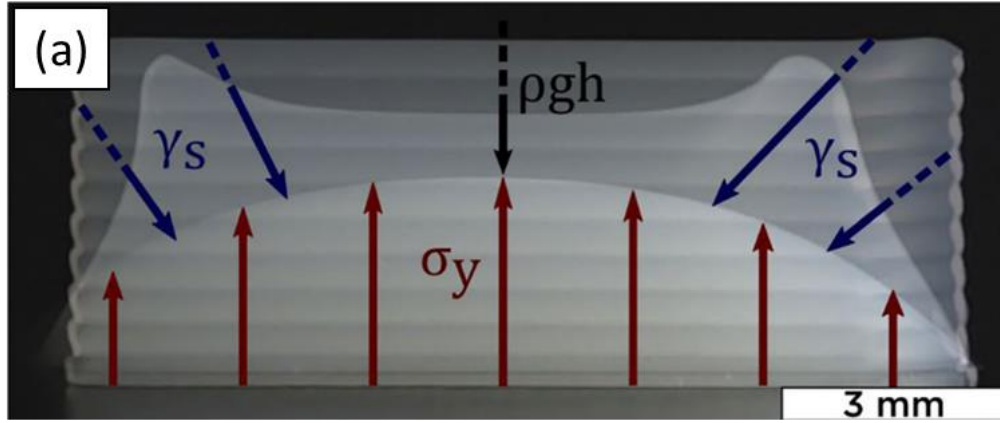


Figure 15: a) Force body diagram of printed boehmite gels, detailing the competing forces used to define  $\Xi$ . (b) A printability map which shows how an increasing  $\Xi$  tends to increase the ratio of the measured cross-sectional area to the theoretical cross-sectional area  $A/A_{th}$  of the printed ceramic structures.

Chan *et al.* performed a small meta-analysis of these two aforementioned printability criteria using clay and alumina stabilized emulsions.<sup>74</sup> The clay suspensions, with volume fractions ranging from 25-50 vol%, constitute primarily attraction dominated gels. However, volume fractions approaching 50% begin the transition into the attractive glass regime. On the other hand, alumina stabilized emulsions constitute a repulsion dominated ink. For their study however, no specific slumping or deformation criteria were given. Printability was determined qualitatively through observations of structural slumping. Regardless, their work failed to find

significant agreement with the inequality proposed by *Smay*. The criteria proposed by *M'Barki* were found to be more useful regarding the clay ink but struggled to predict slumping in the alumina emulsion. *Chan* continued the search for an improved printability criterion related to the storage modulus and dynamic yield stress. Their work notes that visible slumping tends to occur for suspensions with lower values of both the storage modulus and dynamic yield stress. Given this observation, *Chan* proposed a product relationship between  $\tau_y^{dyn}$  and  $G'_{LVR}$  (Equation 14):

$$G' = \frac{C}{\tau_y^{dyn}}$$

*Equation 14*

where  $C$  is an empirical constant,  $G'$  is the storage modulus, and  $\tau_y^{dyn}$  is the dynamic yield stress. For their clay system, the constant  $C$  was found to be in the range of  $6 \times 10^6$  to  $1 \times 10^7$ .

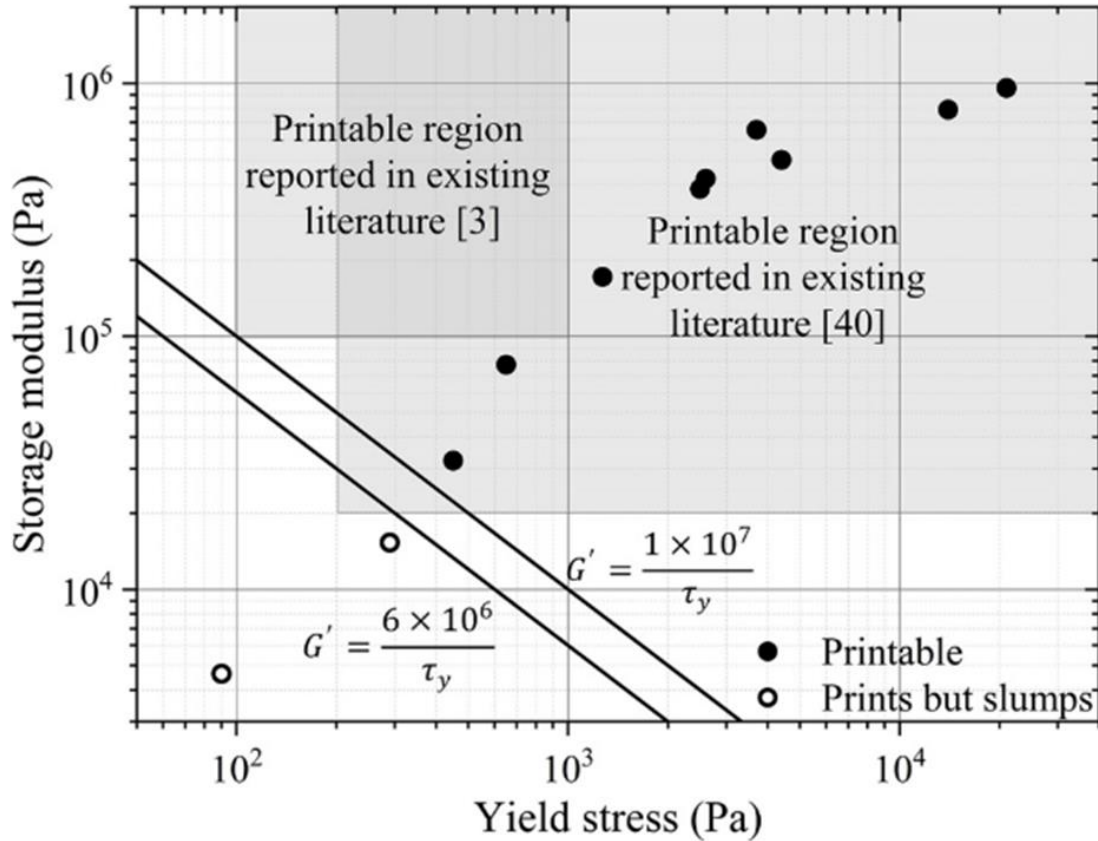


Figure 16: A printability map relating the yield stress and storage modulus of clay suspensions as they relate to visual slumping. Chan et al. used these plots to define empirical relationships of printability. The 'printable regions reported in existing literature' are representative of studies performed by Smay et al. and M'Barki et al.<sup>73</sup>

Across the alumina emulsions, the constant was approximately  $5 \times 10^6$ . This constant was derived by placing a linear fit on plots of the storage modulus vs. dynamic yield stress, demarcating the region in which 91.8% of observations were described. Furthermore, Chan briefly explored the recovery of the storage modulus following a breakdown of the ink structure (applied stress greater than the limit of the linear viscoelastic region). They note that pastes which do not recover to at least  $\sim 10,000$  Pa within the first 15 seconds after deposition will slump. This recovery was again a function of the initial storage modulus, dynamic yield stress, and a constant (Equation 15):

$$G'_{recovered} = \frac{C_2}{G' \cdot \tau_y^{dyn}}$$

Equation 15

Furthermore, *Corker et al.* devised a rheological protocol to define printability of graphene oxide pastes for DIW.<sup>66</sup> The inks within this work were low volume fraction graphene suspension with a strong attractive potential. As such, these fluids may be classified as attraction dominated gels. In their case, a printable ink was one which readily retained shape after deposition and spanned across supports with minimal deflection. Using this definition, they relied upon critical values of the storage modulus,  $G'$ . Their rheological protocol uses a combination of small and large amplitude oscillatory rheology to replicate the ink's structural changes during the printing process, as well as to illuminate any 'history'. Through a parameter, the Flow Transition Index (FTI), which relates the flow stress and yield stress  $\sigma_f/\sigma_y$ , the group was able to predict the brittleness and spanning potential of newly devised inks. Typically, as the FTI approaches 1, the internal structure tends to become more brittle and susceptible to breakage when sheared.<sup>66</sup> Additionally, as the FTI decreases, the inks display increasingly brittle behavior, as less force is required to break the interparticle networks. Those inks in which the  $FTI < 20$  and a  $G'/\sigma_f \geq 20$ , are found to be within their 'printability window'.

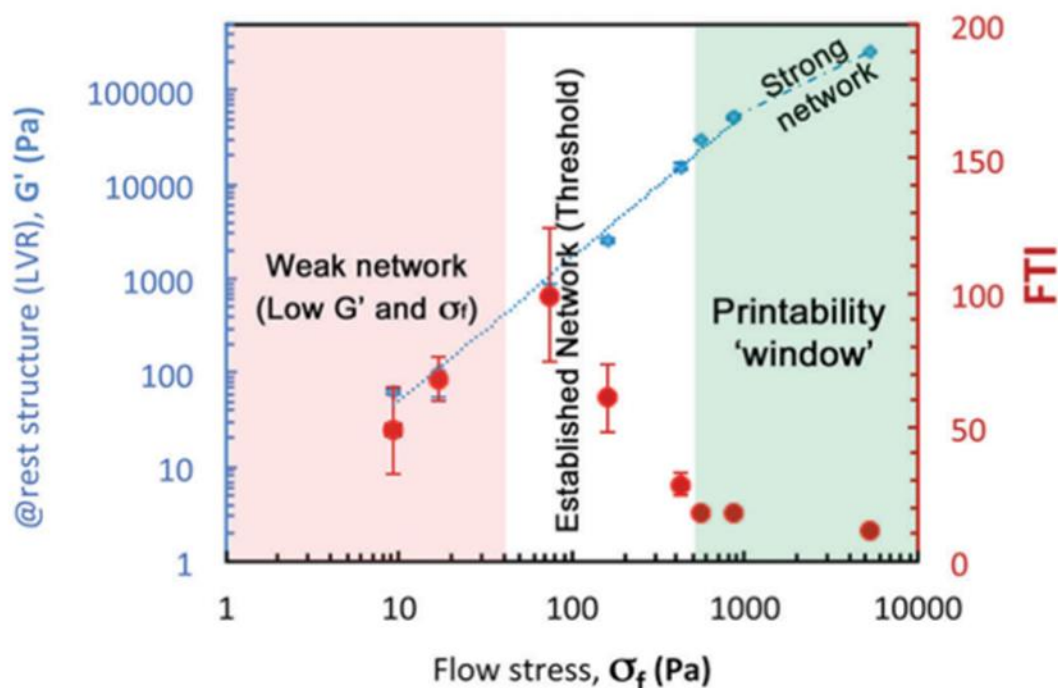


Figure 17: 'Printability' map relating the flow stress, storage modulus, and FTI for graphene oxide inks.<sup>66</sup>

Finally, in recent work, *Ji et al.* aimed to quantitatively evaluate printability using two criteria: the extrusion stress and the storage modulus.<sup>75</sup> They evaluated a series of alumina, yttria, and neodymium oxide aqueous slurries, with rheology tailored via the addition of hydroxyethyl cellulose and a dispersant (Dolapix CE 64). Classification of these slurries is challenging due to the relatively high solids volume fraction (48-52 vol%), and unknown particle size. However, the addition of the dispersant, providing electrosteric repulsion, and hence a repulsively borne yield stress, contributed to a repulsion dominated classification.<sup>76</sup> Inks were synthesized and analyzed with a combination of steady-state and oscillatory rheology. Ultimately, they demonstrate the ability to quantify printability from the extrusion stress and storage modulus. For printable formulations, the extrusion stress ranges from 401 – 430 Pa, while the storage modulus ranges from 2300 – 6000 Pa. Additionally, they note that the recovery index – the fraction of the original storage modulus retained post-extrusion – is a critical printability metric.

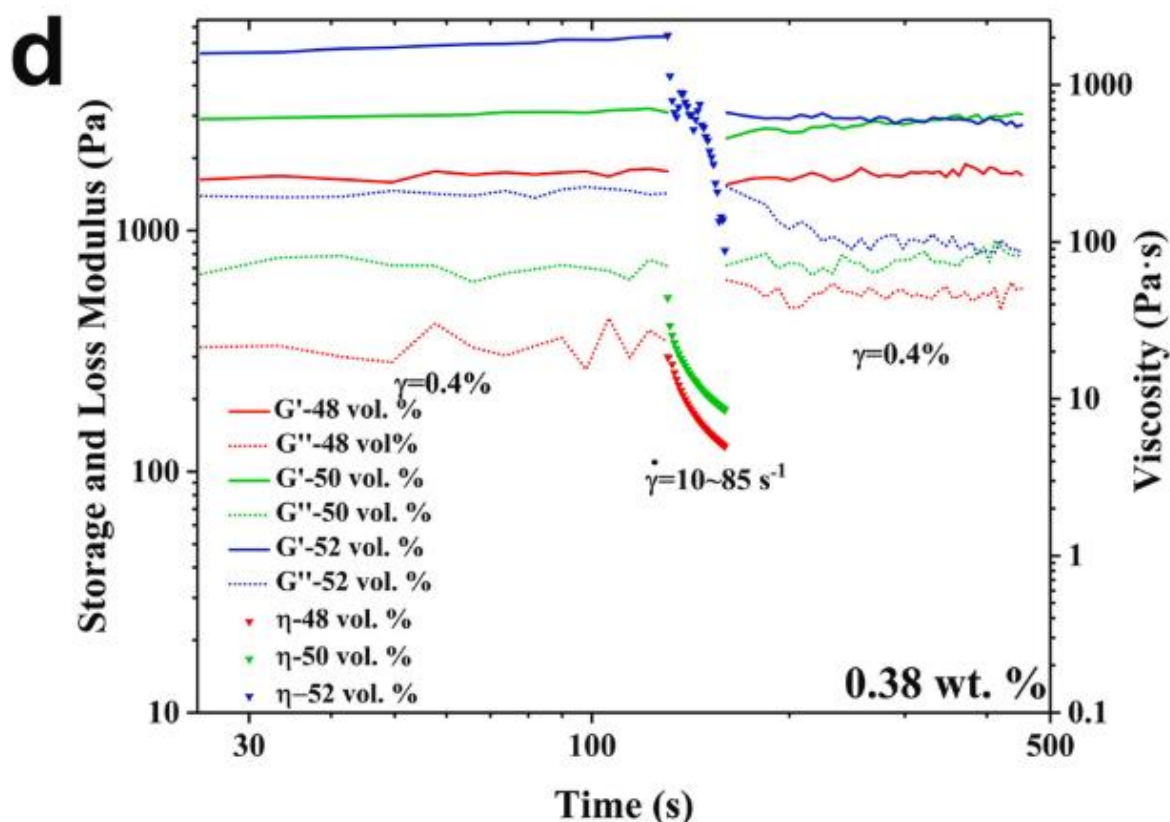


Figure 18: Storage and Loss modulus recovery post extrusion.

The research progress highlighted above shows promise in defining printability for slumping and spanning behavior through rheological properties such as the storage modulus and yield stress. At the same time however, the disagreement on a singular universal metric is evident and the governing relationships appear to depend on the ink system. For example, *Zocca et al.* state printable DIW pastes should have a storage modulus of  $10^5 - 10^6 \text{ Pa}$  and a yield stress of  $10^2 - 10^3 \text{ Pa}$ .<sup>77</sup> *Bonilla-Cruz et al.*, modeling repulsion dominated ink systems, state a flow stress ( $G'=G''$ ) greater than  $10^3 \text{ Pa}$  enables printability.<sup>78</sup> Other groups report the storage modulus should be greater than  $2 \text{ kPa}$  and the yield stress more than  $200 \text{ Pa}$  for printable emulsions.<sup>79</sup> In our previous work, printable copper inks (repulsion dominated hard sphere systems) had a dynamic yield stress ranging from  $700 - 1500 \text{ Pa}$ , static yield stresses ranging from  $1800 - 5000 \text{ Pa}$ , and storage moduli ranging from  $10^5 - 10^6 \text{ Pa}$ .<sup>18</sup> Table 4 provides a further summary of acceptable rheological parameters ranges found in literature.



Table 4: Ranges of optimal rheological parameters for DIW. Asterisks denote attraction or repulsion dominated fluids.

Metric	Symbology	Range(s)	Ink Class	Publication
Static Yield Stress	$\tau_y^{sta}$	116 – 191 6.8 – 25 75 – 300 300 – 1000 122 – 359 274 – 1502 86 – 175 100 – 700	Glass* Gel Gel*, Glass* Gel Glass* Glass Glass Glass	Rueschhoff et al. <sup>80</sup> Smay et al. <sup>53</sup> Karyappa et al. <sup>81</sup> Tunon et al. <sup>82</sup> Costakis et al. <sup>83</sup> Cipollone et al. <sup>18</sup> Ji et al. <sup>75</sup> Zhu et al. <sup>84</sup>
Storage Modulus	$G'$	$10^4 - 10^5$ > 2000 $\sim 10^5$ 2300 – 6000	Gel* Glass Gel Glass*	Chan et al. <sup>74</sup> Minas et al. <sup>79</sup> Smay et al. <sup>53</sup> Ji et al. <sup>75</sup>
Recovery Index	$G'_0 / G'_{end}$	0.8	Glass*	Ji et al. <sup>75</sup>
Flow Transition Index (FTI)	$\tau_f / \tau_y$	10 – 190	Gel	Corker et al. <sup>66</sup>
Shear Thinning Index	$n$	0.28, 0.62 0.06 – 0.075 0.57 – 0.72 0.56 – 0.64 0.15 – 0.29	Gel* Glass* Gel Glass* Glass	Fu et al. <sup>85</sup> Bonilla-Cruz et al. <sup>78</sup> Smay et al. <sup>53</sup> Rueschhoff et al. <sup>80</sup> Cipollone et al. <sup>18</sup>
Critical Shear Rate	$(\tau_y^{sta} / K)^{1/n}$	22 – 32 0.01 – 0.14 37 – 71 0.02 – 7.6 6.6 – 109	Glass* Gel Gel*, Glass* Gel* Glass*	Rueschhoff et al. <sup>80</sup> Smay et al. <sup>53</sup> Karyappa et al. <sup>81</sup> Herrada et al. <sup>32</sup> Costakis et al. <sup>83</sup>
Flow Stress	$\tau_f$	20	Gel*	Smay et al. <sup>53</sup>

		> 200	Glass	<b>Minas et al.</b> <sup>79</sup>
		> 350	Gel*	<b>Chan et al.</b> <sup>74</sup>
		> 100	Glass*	<b>Ji et al.</b> <sup>75</sup>
		> 10 <sup>3</sup>	Glass*	<b>Bonilla-Cruz et al.</b> <sup>78</sup>
Extrusion Stress	$E_p$	401 – 430	Glass*	<b>Ji et al.</b> <sup>75</sup>

Overall, important elements to successful DIW include the existence of a yield stress, the ability of the ink to quickly fluidize, and the ability of the ink to quickly recover solid-like behavior. Again however, authors disagree with the rheological specifications, and fail to achieve global printability criteria. It is my thesis this dispute in printability criteria arises from overlooking the yield stress mechanism and the general microstructure of the ink. It is possible that the rheological specifications are correct locally – for a specific class of yield stress fluid. In the above examples, no author discusses the microstructure of the ink. Instead, printability is discussed globally, ignoring the key fundamental factor – the yield stress mechanism.

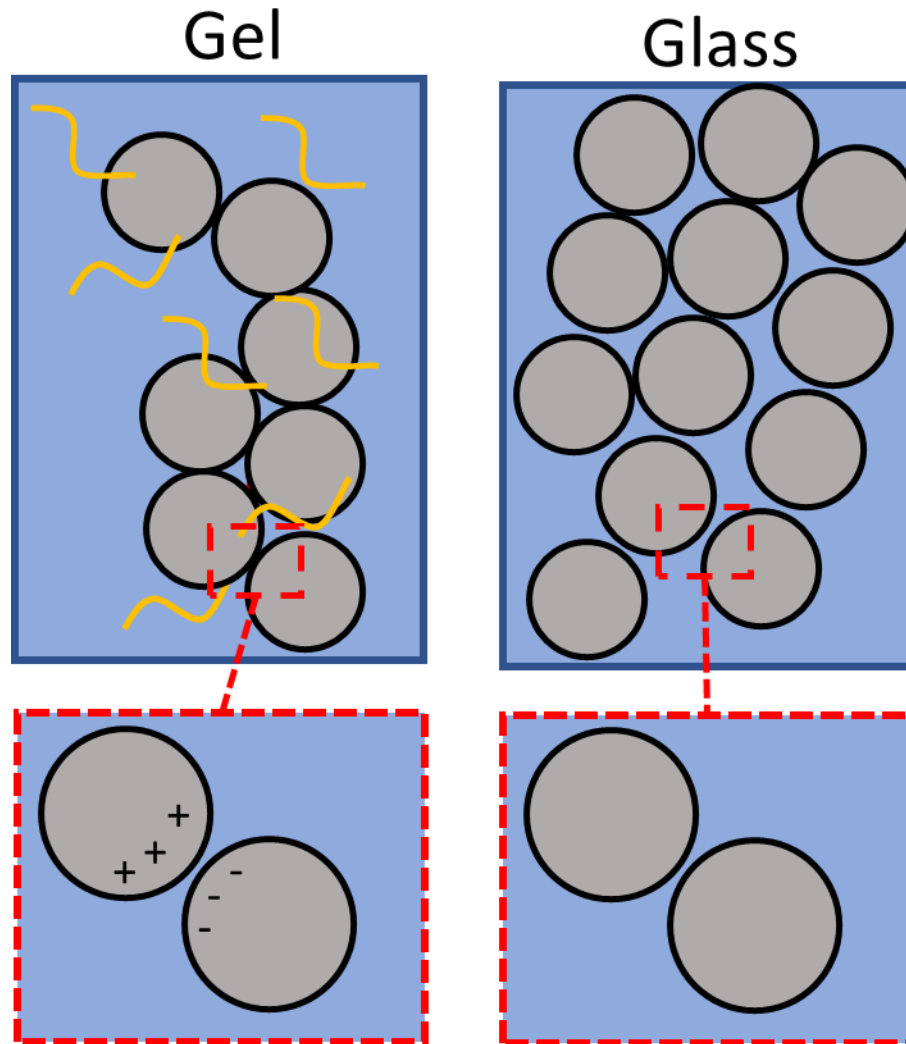
### 3 Design for Direct Ink Writing

Ultimately, the disagreements in printability specifications arise from a lack of analysis of the yield stress mechanisms and ink microstructures. The following sections discuss yield stress fluid fundamentals, attractive and repulsive yield stress mechanisms, and the particle or polymeric networks which comprise each class. Further in the discussion, Ashby-like plots are generated and presented which map yield stress fluid microstructure to printable regions of the rheological parameter space. All data points within the Ashby-like plots are reported to be printable – self-supporting, high fidelity, and reliably extrudable – inks.

#### 3.1 Yield Stress Fluid Classes – An Overview

One can broadly characterize yield stress fluids as glasses and gels.<sup>44,86,87</sup> Yield stress in glasses results from jammed, repulsive interactions. On the contrary, yield stress in gels stems from networked, attractive interactions (Figure 19). Additionally, a system's yield stress can arise from a combination of both attractive and repulsive interactions. This is the case for

attractive glasses, which feature a high-volume fraction and jamming with attractive interparticle forces such as depletion or Van der Waals forces.<sup>87</sup>



*Figure 19: Schematic of gel and glass yield stress fluid microstructures. Gels arise from attractive interparticle attractions due to Van der Waals or depletion forces. Repulsion dominated fluids produce a yield stress from jammed, infinite potentials.*

### 3.1.1 Repulsion Dominated Yield Stress Fluids for DIW

Inks containing particulate phases are very common in DIW. These phases may be ceramic colloids, ceramic microparticles, polymeric microbeads, conductive microparticles, or conductive colloids. As the particulate volume fraction increases, the fluid transitions from a liquid regime with no discernible shape, to an arrested glassy state. However, glassy, repulsion

dominated systems are still disordered systems, as opposed to crystalline. They arrest when some external parameter such as density, attractive potential ( $U/k_B T$ ), or external stress is varied.<sup>67</sup> *Trappe et al.* developed a phase diagram, noting combinations of relative attractive potential ( $k_B T/U$ ), volume fraction, and applied stress which result in jammed microstructures (Figure 20).<sup>67</sup>

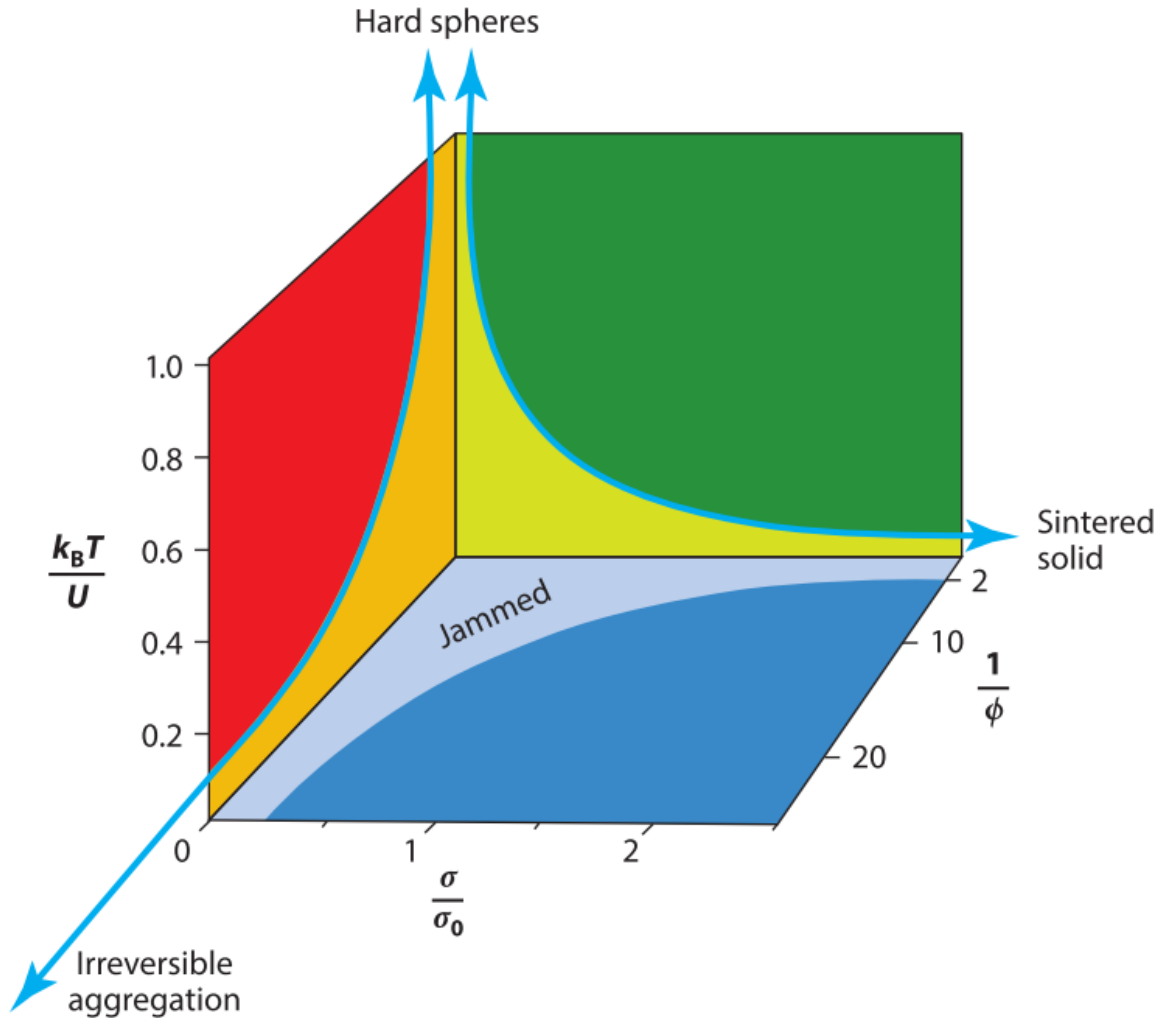


Figure 20: Jamming phase diagram for attractive colloidal particles. The diagram suggests that decreasing interparticle interactions (or increasing temperature), increasing stress, and decreasing concentration induces a solid to liquid phase transition.

From Figure 20, the jammed region surrounds the origin. A transition from solid to fluid-like dominant behavior comes about from increases in the applied stress, increases in  $\Phi^{-1}$ , and increases of  $U^{-1}$ . Notably, the phase boundary in the  $\sigma$  plane represents the critical stress, commonly defined as the static yield stress. Within this diagram, the fluid to solid transition represents a kinetic arrest through caging.

It is generally observed that at low  $\phi_v$ , these materials are in a fluid state. As concentrations approach  $\Phi_{rcp}$  ( $\Phi = 0.64$ ), the systems demonstrate a finite elastic modulus and yield stress. There, particles are effectively ‘caged’ and interact as *hard spheres* (Figure 21).<sup>67,86</sup> At interparticle distances,  $r$ , less than the particle diameter,  $\sigma$ , an infinite repulsive potential appears. Hard sphere systems contrast soft sphere systems, where the same principle of volume exclusion does not apply. In soft sphere models, the repulsive potential increases according to a function and not a step (Figure 21).

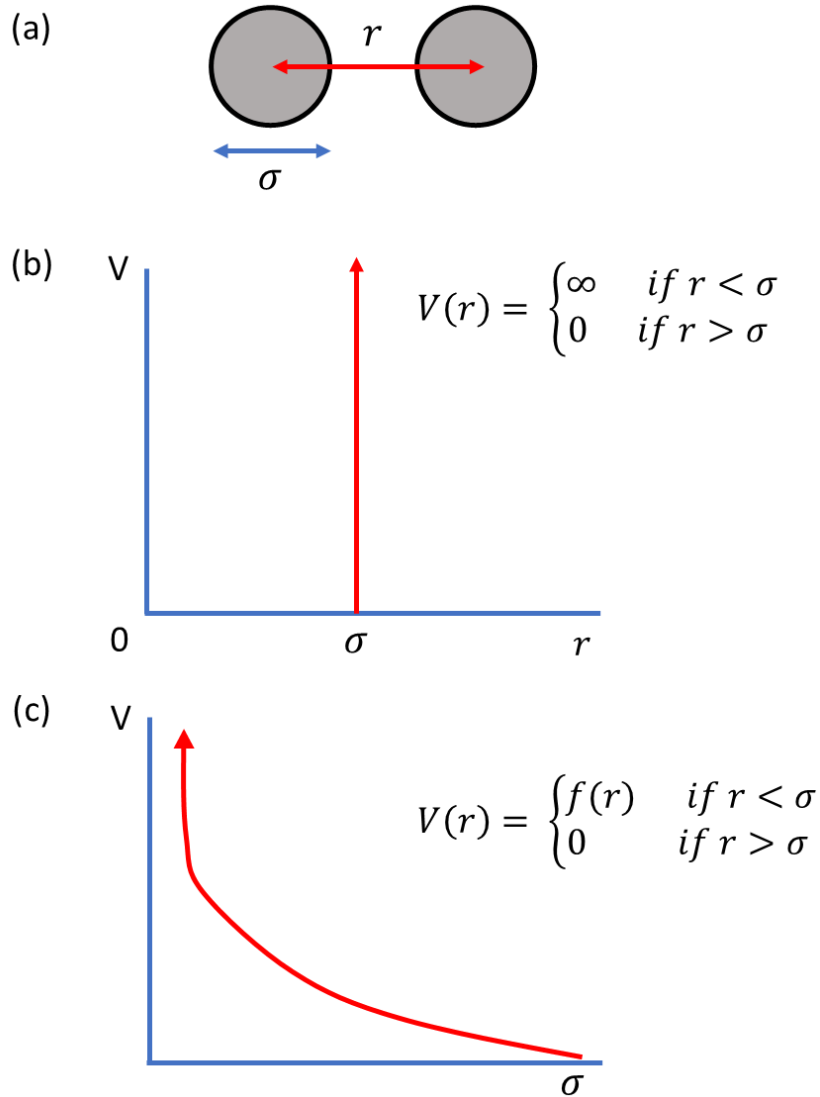


Figure 21: (a) Simplified schematic of two spheres in solution. (b) Hard sphere model potential. (c) Soft sphere model potential.

Jammed microstructures further include particle filled suspensions, foams, polymer microgel particles, and emulsions. Foams and emulsions are generally more challenging to engineer for DIW but do provide the ability to manufacture hierarchical microstructures.<sup>12,14</sup> In emulsions and foams, the dispersed phase is in the form of droplets or bubbles that are electrostatically or sterically stabilized. Common DIW examples of repulsion dominated fluids include suspensions of hard particles (colloidal and non-Brownian, athermal, granular matter), and suspensions of charged-particles, which are effectively jammed through electrostatic

repulsion. Similarly, sterically repulsed colloids are commonly modeled as hard spheres. As the adsorbed surfactant molecules come into proximity, the potential reduction in available conformations imparts a thermodynamic penalty to the Gibbs free energy.

Additionally, non-colloidal particles ( $> 1\mu m$ ) are commonly utilized in repulsion dominated DIW formulations, reducing the need for colloidal chemistry and simplifying ink synthesis. In contrast, for colloidal inks, care must be given to tailor the surface charges and prevent (or induce) flocculation. For macroscopic particles, one must only prevent sedimentation through the introduction of a sufficient binder yield stress or density matching.<sup>88</sup> In many cases, one employs a small volume fraction of polymeric binder to prevent sedimentation. Though the chemistry varies widely within and across these material classes, yield-stress fluid behavior is caused by the same fundamental mechanism of effectively crowded microstructural elements interacting repulsively.

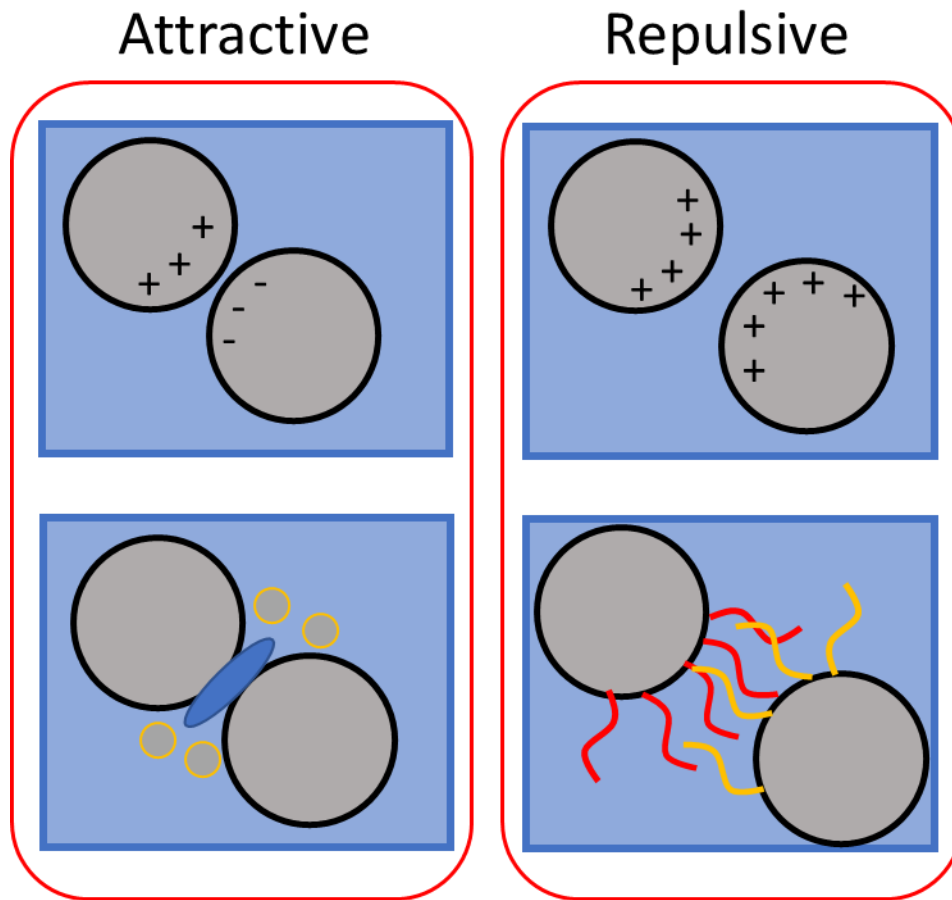


Figure 22: Attractive interactions generally result from Van der Waals (top left) or depletion forces (bottom left). On the other hand, repulsive interactions result from electrostatic repulsion (top right) or steric repulsion (bottom right).

### 3.1.2 Attraction Dominated Yield Stress Fluids for DIW

In attraction dominated yield stress fluids, elements “pull” on nearest neighbors.<sup>69</sup> Inks, such as those composed by colloids, typically possess attractive borne yield stresses, yielding when the reformable attractive bonds break. However, in gel systems, the particulate volume fractions are lower in comparison to repulsion dominated, arrested systems.<sup>44,86</sup> Gel solid volume fractions range from  $\varphi \approx [0.1, 0.5]$  depending on the magnitude of the attractive potential. In many cases, one can tailor the yield stress of the colloidal ink by changing the surface charge of the particle, inducing flocculation, and hence the magnitude of the neighbor-to-neighbor “pulling”. For example, in previous work involving coaxial ceramic ink DIW, the ink stiffness varied by nearly an order of magnitude by flocculating colloidal alumina through



titration.<sup>51</sup> Likewise, PZT gel stiffness was tailored via electrostatic screening, inducing flocculation.<sup>53</sup> Within attractive structures, gravitational forces play little role, while Van der Waals, electrostatic, and depletion forces govern the particle interactions, attractive potential, and ink stability.

Similarly, polymeric yield stress inks contain numerous physical and chemical crosslinks capable of bearing a static load. Such inks form the foundations of bioprinting including attraction dominated inks formulated with alginate<sup>89</sup> and algae/gelatin composites.<sup>62</sup> Hydrogels such as xanthan gum, and hard-sphere-polymer composites which contain a low volume solid phase, are contained within this group.<sup>44</sup> External electric or magnetic fields induce attractive interactions and produce attraction dominant yield stress fluids. Additionally, low volume fraction 2D particulate inks, such as those incorporating graphene and graphene oxide, form percolated, weakly attractive networks.<sup>66</sup> Morphologically, material microstructures within this group typically are sparse percolated networks spanning the sample which must be destroyed for yielded flow to occur.

Attraction-dominated microstructures resist being pulled apart, eventually yielding once these re-formable attractions have been broken. Notably, upon release of the stress, the attractive network reforms. However, the restructuring times of weak attractive networks is longer than those of repulsive microstructures. In a potential design scenario where, one requires rapid post-extrusion stiffness recovery, a repulsive or repulsion-dominated yield stress fluid may be appropriate. Likely, given the repulsive structure, the recovered storage modulus ( $G'_{recovered}$ ) will near 100% of the initial storage modulus ( $G'_0$ ), signaling a high degree of bulk recovery. Again, these are potential considerations as we progress to *design* for DIW.

### 3.1.3 Attractive Glasses

Attractive glasses, named after the arrested glassy state of polymers, feature properties of both attraction and repulsion dominated fluids and are commonly found within DIW. These, typically colloidal, inks feature high volume fractions ( $\Phi > 0.5$ ) as well as short range attractive forces. Examples of attractive glasses include bimodal ceramic formulations and biocompatible ceramic nanoparticle inks.<sup>51,80</sup> With a decrease in  $\Phi$ , a primarily attractive gel phase forms.

However, with a decrease in the attractive potential ( $U/k_B T$ ), a repulsive glass forms.

Flocculation and titration, altering the surface charges of colloidal inks, can induce transition from repulsion dominated to attractive glass-like microstructures.<sup>90,91</sup> For attractive glasses to yield, they must break both attractive bonds and repulsive cages. In contrast, repulsion dominated fluids must only break cages, while attraction dominated fluids must only break bonds. Generally, attractive glasses first break bonds, and then at a higher strain amplitude break cages.<sup>43,92</sup>

### 3.2 Transitioning to DIW Design

In DIW, yield stress fluids include high volume fraction ceramic slurries, colloidal gels, and cell-laden bio-inks. In all these applications, how the yield stress (and its origin) is achieved is irrelevant to researchers. The important element of these fluids is that they exhibit yield stress. In essence, the objective of ink design is functionality, not the chemistry that achieves it. To progress the field and make progress in understanding printability, we challenge this approach. It is not necessarily a focus on the exact chemistry, but how the chemistry relates to microstructure and ink component interactions. This coupling opens the door for design of yield stress fluids – relating potential target rheological properties to fluid microstructure.

Without microstructural classification, printability is only *locally* defined. Does that however mean that the author's rheological specifications are wrong? No. It just may mean they do not apply globally. Unbeknownst to them, authors define local printability and to great effect. Most literature in the field of rheology, complex fluids, non-Newtonian fluid mechanics, and soft matter, is often framed in terms of analyzing and understanding how materials or systems will behave. Design builds upon the knowledge from analysis, but frames problems differently and requires organizing the available information in different ways, e.g., to contrast how different concepts could achieve a specific desired outcome.

When taking a design approach, a set of material specifications are chosen. Then, from a comparison of the available classes and material properties, one can down-select a specific material for a particular application. The design methodology is frequent in mechanical design, where the number of materials available is overwhelming. Ashby states that as of 1999, the

total number of available engineering materials ranges between 40,000 – 80,000.<sup>93</sup> How could one select a material without a clear demarcation of key properties? This is essentially the dilemma faced by materials engineers in the current 3D printing paradigm.

In mechanical design, without material properties compared and displayed, many engineers may default to a traditional material, such as steel. Not only is this default possibly application limiting (cost or weight ineffective), but limits design freedom and the development of new materials and the fractal nature of material evolution. Again, such is the case in fledgling DIW design. Engineers default to a given yield stress fluid microstructure and ignore the rich design landscape. This default not only impacts the application targets but hinders the development of new ink microstructures and functionalities.

Ashby plots are one tool that provides a visual method of material down selection. Such plots are common in mechanical and civil engineering materials selection, providing a visual comparison of properties such as elastic modulus and density, or tensile strength and cost. Their convenience lies in the fact that they provide useful information not only on which material displays the highest (or the lowest) property reported on the x- or y-axes, but also which one presents the highest ratio between the two properties. It is useful, in addition, to compare properties values with relation to material dimensions or density and offer the possibility to condense a large body of information into a compact, but accessible form ( Figure 23).

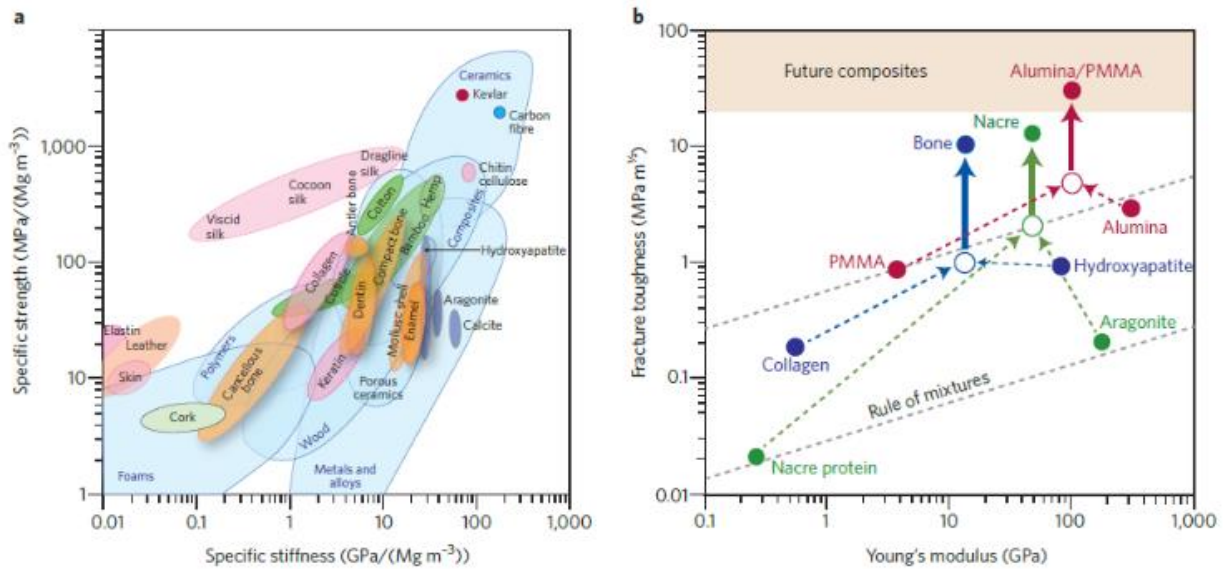


Figure 23: a) Specific properties normalized by density allow easy comparison with synthetic materials like polymers and ceramics. b) Visualization of how nanocomposites can display dramatically improved properties with respect to the starting building blocks.<sup>94</sup>

These plots were proposed by Michael Ashby throughout his design focused work. As stated by Ashby, there are three general types of design:

1. *Original design*
2. *Adaptive design*
3. *Variant design*

*Original design* begins from scratch and implements a new material (e.g., yield stress fluid microstructure) to exploit the unique properties and develop a new application. For example, high-purity glass enabled the optical fiber. In DIW, an emulsion templated polymer (repulsive-attractive hybrid microstructure) enables drug laden bio-scaffolds. In *Adaptive design*, one aims to make an incremental advance. For example, one could replace a metal with a polymer, improving the strength to weight ratio. In DIW, one could modify the particle size distribution to increase packing and reduce shear apparent viscosity. Finally, in *Variant design*, one simply changes the scale of the device, without changing the function or method. Ashby provides

examples of scaling boilers, pressure vessels, or turbines. The functionality remains the same across scales. In 3D printing, one could seek to implement a large area additive manufacturing process, instead of the typical bench scale process.

The mechanical design process is best shown with case studies, as illustrated in the Appendix. One can find further examples in *Materials Selection in Mechanical Design*.<sup>93</sup> The case studies follow a similar procedure: 1) developing a problem statement, 2) identifying limiting functions and application target properties, 3) material screening and selection, and 4) philosophy and postscript. Current DIW engineering typically skips from step 1 to step 4. Inks or materials are pre-selected for an application and the properties are analyzed post-application. Skipping steps 2 and 3 limits DIW progress and ignores microstructure while simultaneously hindering the development of new knowledge (i.e., the relationship between fluid microstructure and valid rheological target properties).

### 3.2.1 Utility in Direct Ink Writing Design

Ashby-like plots can be a useful step towards design for DIW, if the governing first and second order design variables can be identified. This is one area that certainly lacks attention and could benefit from the development of a rheological database and consensus regarding rheological characterization. Before establishing DIW Ashby-like plots, the design variables must be noted. Since a particular value of yield stress can be achieved by multiple materials, applying additional design constraints on secondary parameters or properties is a critical step in converging on a final design choice in a rational, non-arbitrary way. However, due to the function-valued nature of rheologically- complex material properties, low-dimensional representations are necessary for their easy comparison. Table 5 displays potential first, second, and third order design parameters, as well as the key design variables within each one.

Table 5: First, second, and third order DIW design variables.

First order	Second order	Third Order
$\tau_y^{static}$	$G' / G''$	$E = \frac{We}{Re} = \frac{v\mu}{\gamma}$
$\tau_y^{dyn}$	$Re$	
$\varepsilon_{stb}$	$We$	
$\tau_{thixo}$	$\dot{\gamma}_{critical}$	
$G'$	$\Xi = \frac{\tau_y^{dyn}}{\gamma R^{-1} + \rho gh}$	
$\rho$	$FTI$	
$n$		
$\gamma$		
$\tau_{flow}$		

As a researcher designs for printability, this table can serve as a reference or as a method to calculate target rheological specifications given some known processing requirements or limitations, such as the desired maximum wall shear stress, the recovery index, or the minimization of plug flow and minimum target flow rate (i.e., extrudability). These limitations could be mundane such as an extrusion pressure regulated by hardware, or a maximum shear stress cells will experience within a nozzle. Moreover, as the Ashby plots are built relating the comparison of the rheological parameters to material classes, certain yield stress fluids – attractive or repulsive – can be down selected.

The selected first order fluid properties are those directly measurable from steady state and oscillatory rheological experiments. Likewise, material properties such as fluid density and surface tension are included. The first order properties are common in most DIW printability studies and can be utilized within second order design parameters. For example, if a second order design constraint is an elastic, non-brittle ink, the flow transition index (FTI) may be a guideline, which is constructed from the flow stress and static yield stress. Additionally, if the ability of the ink to withstand gravitational forces is a concern,  $\Xi$ , which conveys the ratio of the supporting (dynamic yield stress) to opposing (gravitational and capillary) forces, can be employed. Figure 24 displays a mock design process for a bio ink in which cell survivability is the

primary objective. Fluid constraints could include a minimization of plug flow and a stiffness recovery index greater than 0.9.

Table 6: Design objective for a cell-laden bio-ink.

Function	3D scaffold for bone cells
Objective	Maximize cell survivability during deposition
Constraints	<p>(a) Minimize plug flow</p> <p>(b) Recover Index <math>G'_{end}/G'_0 &gt; 0.9</math></p> <p>(c) <math>\tau_{max} &lt; 100 Pa</math></p>

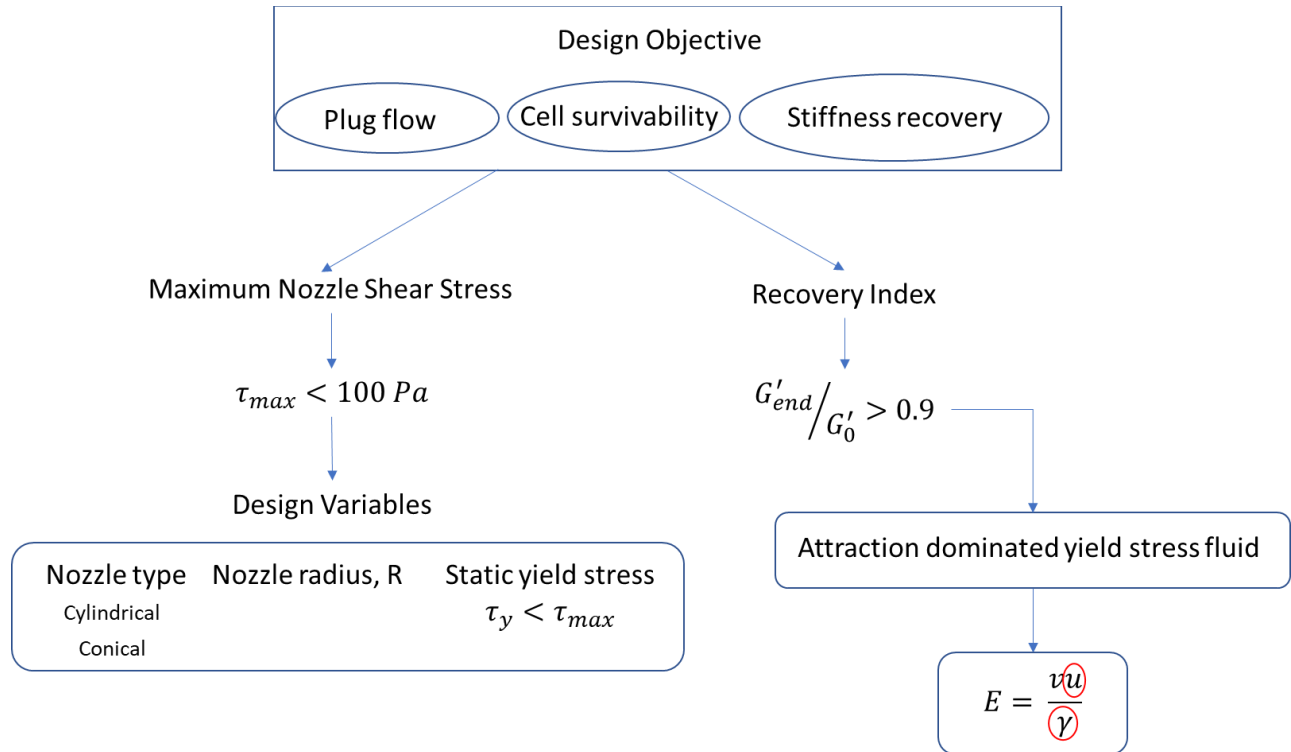


Figure 24: Example of down selecting a yield stress fluid and rheological parameters to meet design specifications.

As shown in Figure 24 , a challenge arises not only in establishing the constraints, but in identifying the necessary process parameters and printing hardware. For example, selecting the proper nozzle radius and nozzle type (cylindrical or conical) will greatly influence the required

extrusion pressure, flow rate, and maximum shear stress.<sup>81,95</sup> The DIW parameter space is dense because it places process-property relationships front and center. Ashby-like plots can aid in material selection and viable rheological parameters for a given microstructure. Though outside the scope of this thesis, future work will aim to fully couple the property dependent process parameters. Table 5, which outlines first, second, and third order DIW rheological and process parameters may serve as a starting point. As a final note, the lack of DIW Ashby-like plots greatly impedes a key step with the design process: the Postscript. If one is unaware of the range of microstructures which could achieve similarly enabled ‘printability’, no effective self-reflection can be made.

However, before first meeting the challenge of coupling property dependent process/hardware parameters, the identification of the rheological parameters for DIW design must be established. As demonstrated in the above case study, for non-rheologically complex materials, selection methodologies are well developed. The key difference between standard materials selection outlined by Ashby and rheological materials selection (the search for printability), is that yield stress fluids are described through function valued properties. For example, the material behavior is not captured by a scalar such as elastic modulus – although one could argue the storage modulus substitutes – but through rate dependent measurements. Ultimately, it is a flow curve, an oscillatory curve, and a descriptive function that capture the material behavior. From these functions, if applied uniformly, one can extract transferrable parameters used to guide future design.

This work hypothesizes that, in part, the direct ink writing literature struggles to define printability because the functional requirements and functional concepts are ill-defined. Too broad and insufficiently vague definitions of printability lead to a varied reporting of metrics and an extremely broad range of ‘optimal’ (*local*) rheological values. For example, if one describes their functional requirements as being extrudable, one cannot reasonably narrow the potential materials. Identifying a printable fluid requires a multidimensional perspective.

Moreover, even if some design constraint is applied, such as a specific yield stress, secondary parameters are ignored. For example, inks may have the same static yield stress, but significantly different storage moduli, shear thinning indices, and dynamic yield stresses. In this



common case, which ink is printable? Which ink is optimal? We argue it is microstructurally dependent. Direct ink writing must be more specific, but not overly-limiting, in the required printability metrics. Following the design process established by Ashby is a reasonable place to start.

*Nelson and Ewoldt* further state that although a lack of a database of rheological properties in the public domain has been identified previously, along with the necessity for a standard that these data sets conform to for facilitating comparison, none exists.<sup>57</sup> In addition, several unique difficulties must still be addressed to establish effective organization and design databases for yield-stress fluids. These include the recognition of function-valued properties, and the notice that some rheological phenomena are not achieved by all materials. These issues are generally not present in solid materials which all have a basic set of simply-defined material properties such as density and Young's modulus.

Regardless of these issues, *Nelson and Ewoldt* demonstrate the utility of design within DIW. For example, from the Herschel-Bulkley model, one can generate 2D projections of the three-parameter function.<sup>57,69</sup> One can plot the shear-thinning index and critical shear rate versus the static/dynamic yield stress. Likewise, given a proper problem statement and functional constraints, one can relate first order parameters such as the extensional strain to break and yield stress to yield stress fluid microstructure. *Nelson* demonstrates the ability of these plots to generate novel yield stress microstructures (essentially composite yield stress microstructures similar in nature to the modulus-density improvements suggested by Ashby in the oar case study, see Appendix).

However, these can plots also guide printability within DIW. Ashby-like plots developed for printable – self-supporting and extrudable – yield stress fluids, reduce the need for laborious analysis-based engineering approaches. For a given microstructure and set of performance indices, one can compare several function valued properties. From here, one can guide the ink synthesis, develop printability targets, or identify alternative viable microstructures.

### 3.3 DIW Ashby-like Plots

In the end, data is critical. To advance the field of DIW, a database must be established. For all materials, intrinsic materials properties such as density and particle size must be reported. Furthermore, one must characterize inks identically. Inks should undergo both steady-state and oscillatory measurements. To capture the steady-state flow curve properly, the Herschel-Bulkley model should generally be applied, and the parameters tabulated. Moreover, the storage modulus, loss modulus, yield stress, and flow stress must be reported from oscillatory measurements. Tertiary parameters such as the  $G'/G''$  ratio or the flow transition index (static yield stress/flow stress) can be calculated.

Table 7 provides the framework for a DIW focused rheological database. Relevant first and second order rheological parameters are included, as well as descriptions of the system and a 'yes-no' printability report. Moreover, details of the particle size and solids weight or volume fraction are included. To establish the first DIW focused Ashby-like plots and guide future printability, this work collected and organized 276 inks synthesized for direct ink writing. From each work analyzed, the relevant function valued properties were collected and organized. It is my hope this will inspire data uniformity in the field, functionally structure the scattered data, and aid the development of novel DIW microstructures.

*Table 7: Example DIW rheological database. Regular reporting of these parameters will guide continuous Ashby plot development and improvement.*

Class	General Structure	$n$	$K$	$\tau_y^{stat}$	$\tau_y^{dyn}$	$G'$	$G''$	$\dot{\gamma}_{crit}$	$\tan\delta$	$\tau_f$	FTI	Printable (y/n)	Particle Size

To aid design for DIW, Ashby-like plots of the storage modulus, critical shear rate, and shear thinning index versus the static yield stress have been developed using the assembled rheological database. These parameters are consistently some of the most reported within DIW. However, different acceptable or optimal values are reported, with little attention given to the microstructure.

Data analysis, performed in Python using the Pandas and Seaborn libraries, helps explore variable relationships and guide Ashby-like plot generation. The code can be found in

the Appendix and will be hosted on GitHub ([Code Repo](#)). First, a pair plot was generated for each permutation of the Herschel-Bulkley parameters and storage modulus (Figure 25). A pair plot of all continuous variables within the database can be found in the Appendix. Then for each continuous variable, a box plot with respect to fluid class was generated. The box plot provides the minimum, first quartile, median, third quartile, and maximum values. Finally, for continuous pairs of data, such as the static yield stress and storage modulus, or the static yield stress and critical shear rate, scatter plots with respect to fluid class were generated. Importantly, the scatter plots detail the relationships between the variables for both printable and non-printable fluids. To generate Ashby-like plots, a convex hull capturing 70% of the data was drawn and shaded for each key pair of variable relationships.

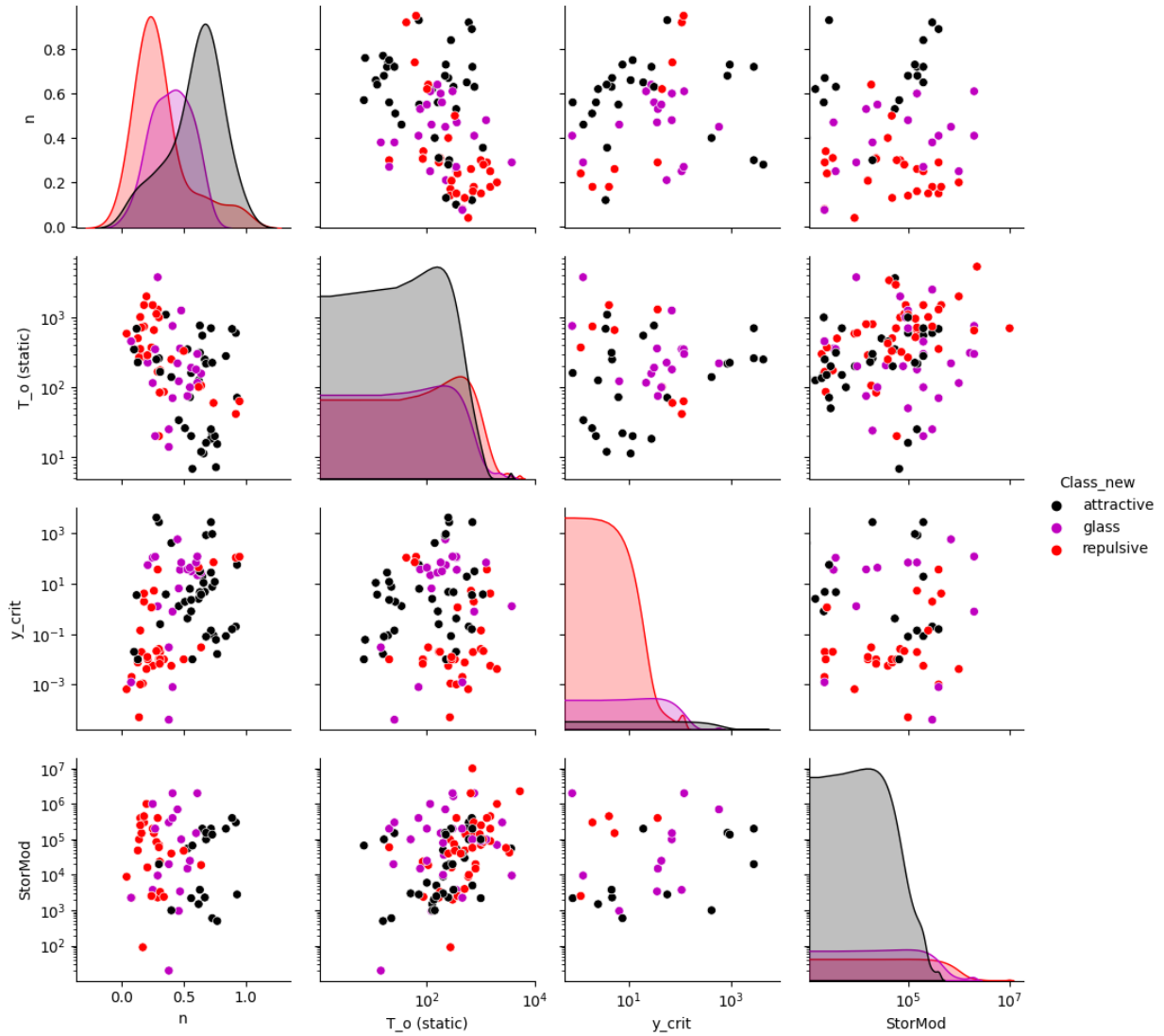


Figure 25: Pair plot of variable combinations of the Herschel-Bulkley parameters and Storage Modulus.

Before pair analysis and Ashby plot generation, each of the four rheological metrics were explored individually across fluid class. Figure 26 shows a box plot of each. The first quartile, median, and third quartile are shown below, in Table 8-Table 10.

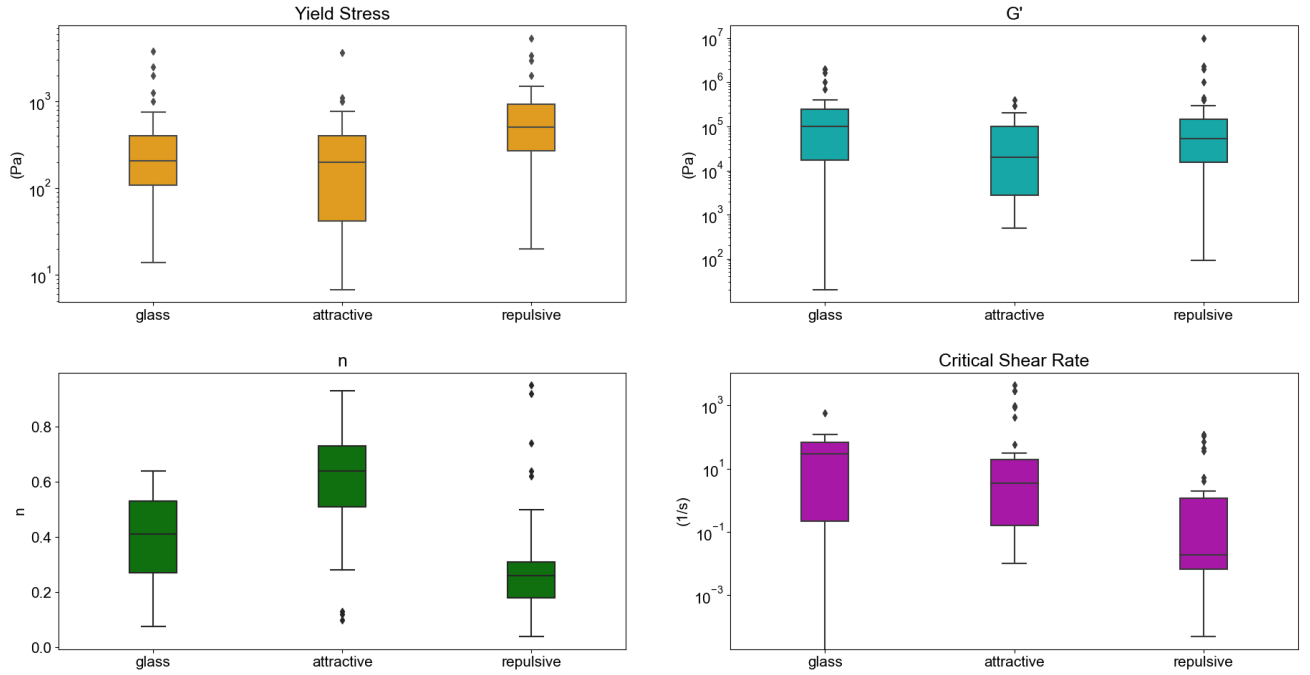


Figure 26: Box plots of the rheological properties by fluid classification.

Table 8: Q2, Median, and Q3 for Attractive Glass Printable Inks

Attractive Glass				
Quantile	$\tau_y^{static}$ (Pa)	$G'$ (Pa)	$n$	$\dot{\gamma}_{crit}$
0.25	107.5	17500	0.27	0.22
0.5	206	100000	0.41	29.72
0.75	404.5	250000	0.53	66.47

Table 9: Q2, Median, and Q3 for Attraction Dominated Printable Inks

Attraction Dominated				
Quantile	$\tau_y^{static}$ (Pa)	$G'$ (Pa)	$n$	$\dot{\gamma}_{crit}$
0.25	41.91	2800	0.51	0.16
0.5	200	20000	0.64	3.56
0.75	400	100000	0.73	19.41

Table 10: Q2, Median, and Q3 for Repulsion Dominated Printable Inks

Repulsion Dominated				
Quantile	$\tau_y^{static}$ (Pa)	$G'$ (Pa)	$n$	$\dot{\gamma}_{crit}$
0.25	268.75	15305	0.18	0.00668
0.5	501.5	53100	0.26	0.01935
0.75	920	147500	0.31	1.16023

From Figure 26 and Table 8-Table 10, a trend is observed for the shear-thinning index,  $n$ . Repulsive fluids have the lowest median shear thinning index of approximately 0.26, which is consistent with previous findings of non-Brownian suspensions with increasing solids volume fraction.<sup>96</sup> It is hypothesized this rapid reduction in shear-thinning index is related to a lack of interparticle friction in formulations with Newtonian or moderately shear-thinning solvents. On the other hand, many purely attractive fluids possess borderline Newtonian characteristics, and are mildly shear thinning, with a median shear-thinning index of  $\sim 0.64$ . Attractive glasses mark the transition region and possess a median shear thinning index of  $\sim 0.41$ .

A similar trend is observed with the critical shear rate, defined as the shear rate at which the shear stress is twice that of the yield stress. At the critical shear rate, the viscous component of the material is dominant, and the viscoelastic fluid has yielded. Again, the dominant attractive behavior of a yield stress fluid typically results from chemical or physical crosslinks, which provide greater resistance to inelastic shear deformation. Repulsion dominated fluids tend to have lower critical shear rates, as the lack of polymeric binders and attractive network forces contribute to a rapid internal breakdown under an applied shear rate. As such, the median critical shear rate increases as attractive forces dominate the fluid. For comparison, the median critical shear rate of repulsion dominated fluids is  $\sim 0.02$ , while the median rate for attraction dominated fluids is  $\sim 3.56$ . Interestingly, attractive glasses possess a significantly higher median critical shear rate. This may be due to the two-phase yielding process of attractive glass yield stress fluids, in which the attractive bonds first break, followed by breaking of the cages.<sup>86,87</sup>

The storage modulus and static yield stress alone differentiate the fluid classes to a lesser degree. This finding likely contributes to the challenges in defining printability and is

related to the function valued nature of yield stress fluids. From this data analysis, several variables are needed to ‘locate’ or define a yield stress fluid. However, some degree of separation is found through the yield stress and storage modulus alone. Generally, inks with a high particle loading will have a higher linear viscoelastic range storage modulus, as is shown by the higher median storage moduli of repulsive and attractive glass fluids. However, the yield stress of attractive glasses tends to be slightly lower than that of purely repulsion dominated fluids.

To lay the framework for DIW design, convex hulls were plotted which contain data within two standard deviations of the mean. Data which falls outside of the interquartile range was excluded from the convex hulls. While not capturing the full nature of the yield stress fluid classes, the shaded convex hulls, referred to herein as Ashby-like plots, visually capture the general behavior of each ink class. Moreover, in future design scenarios, the shaded regions provide design criteria ranges. For example, if the critical shear rate and storage modulus are design constraints, one may consult the  $G'$  and  $\dot{\gamma}_{crit}$  Ashby co-plot.

The Ashby-like plots contain attraction dominated, repulsion dominated, and attractive glass yield stress fluids. The inks are labelled “attractive”, “repulsive”, and “glasses”, respectively. Attraction dominated inks typically contain systems with a low volume fraction solids and significant polymer volume fraction. Many hydrogels, polymers, and low volume fraction colloid-polymer composites fall within this label. Repulsion dominated systems contain inks with a particle volume fraction greater than 0.5 and particles with a diameter greater than  $1\ \mu m$ . At this size, attractive forces such as van der Waals have diminishing effect. Moreover, colloidal systems that are sterically or electrostatically stabilized with a volume fraction greater than 0.5 are labelled as repulsion dominated. Systems with a particle volume fraction greater than 0.5 but are flocculated through charge screening, adjustment of pH, addition of salt, etc. are labelled as attractive glasses. The defining element of the attractive glass label stems from high particle volume fraction ( $\Phi > 0.5$ ) and the inclusion of attractive interparticle potential. Ultimately, these maps form a framework, and are intended to change as more data is collected.

As a note, a potential source of error comes from my classification system. Reclassifying the inks based upon a different set of criteria will obviously produce different Ashby-like plots. In this case, the classes were determined from a combination of the particulate volume fraction, particle size, and binder volume fraction. Other factors, such as the particle surface roughness and shape were not considered, though they are known to impact the flow properties.

As an example, future efforts may significantly improve on the classification scheme through quantification of the degree of attraction and repulsion. This quantification will require more effort from the ink engineers in terms of system characterization, but reduce label (attraction-dominated, repulsion dominated, etc.) uncertainty and reduce experimental time on the back-end. Moreover, linking the quantification of attraction or repulsion to existing yield stress scaling laws for a system provides an additional classification metric. For example, existing scaling laws for charged particles and particulate gels utilize the interaction potential at an average interparticle separation ( $W(r_m)$ ) and the maximum spatial gradient of interaction potential ( $W'_{max}$ ), respectively.<sup>57</sup> Integrating additional quantitative metrics to the database opens the door for machine learning (ML) methods and ML prediction of printability.

One can quantify the interaction potential (repulsive or attractive) with several techniques. Conforming to DLVO theory, one could employ optical tweezers to manipulate particles and digitally track the particle interaction potential as a function of distance. Furthermore, characterization of the structure factor is commonly employed for colloidal and colloidal-polymer systems.<sup>97</sup> However, more practically, one could characterize the double-layer potential using zeta potential measurements. Strongly stable solutions ( $\pm 40mV$ ) coupled with solids volume fraction ( $\Phi > 0.5$ ) could be used to classify attractive and repulsive glasses.

### 3.3.1 Storage Modulus versus Static Yield Stress

Figure 27 details the  $G' - \tau_y^{stat}$  regions for self-supporting, 3D compatible inks. The magenta shaded region highlights printable attractive glasses, in which the yield stress results from a combination of attractive forces (van der Waals, depletion, electrostatic, etc.) and a high-volume fraction ( $\Phi_v > 0.5$ ). The static yield stress, taken from the Herschel-Bulkley model or initial ~5% change in storage modulus within the linear viscoelastic region, spans from 30 ~ 700 Pa. Note the eventual overlap with the repulsion dominated yield stress fluids (red),



containing jammed hard sphere inks. Contrasting the attractive glass region lies the red shaded region. Here exists repulsion dominated, glass-like printable inks. Many within the space are emulate hard spheres. Importantly, hard spheres are non-interacting, and the yield stress arises from repulsive interactions. Finally, in the black shaded region, exist the attraction-dominated yield stress fluids. The shear properties are a function (to varying degrees) of the attractive polymeric networks and any incorporated particulate phases. Importantly however, the particles do not interact attractively.

Broadly, we see the storage modulus increase with the yield stress throughout the attraction-dominated regime, likely due to increasing solids volume fraction. Upon transitioning into the attractive glass and repulsion-dominated spaces, one reaches a printable storage modulus plateau. No upper limit of storage modulus has been defined within literature for DIW printability. However, both the storage modulus and static yield stress tend to scale with solids volume fraction according to a power law. For example, in attractive colloidal gels the plateau storage modulus according to Equation 16:

$$G'_p = G_0(\Phi - \Phi_c)^{v_\Phi}$$

*Equation 16*

where  $\Phi_c$  is the critical volume fraction marking the fluid to solid phase transition,  $\Phi$  is the solids volume fraction,  $v_\Phi$  the power law scaling factor, and  $G'_p$  the plateau storage modulus.<sup>98</sup> Likewise, for hard sphere suspensions, the static yield stress scales with a power of 0.5 with solid volume fractions greater than the critical volume fraction:

$$\sigma_y = \sigma_{crit} + 112\sqrt{\Phi - \Phi_c}$$

*Equation 17*

where  $\sigma_y$  is the yield stress,  $\sigma_{crit}$  is the yield stress at the critical volume fraction,  $\Phi$  is the volume fraction, and  $\Phi_c$  is the critical volume fraction.<sup>99</sup> Ultimately, both the storage modulus and yield stress scale with increasing solids volume fraction. Lack of printability arises when the volume fraction fully arrests the structure, inhibiting the fluid's shear thinning ability and ability to flow under given DIW hardware constraints.

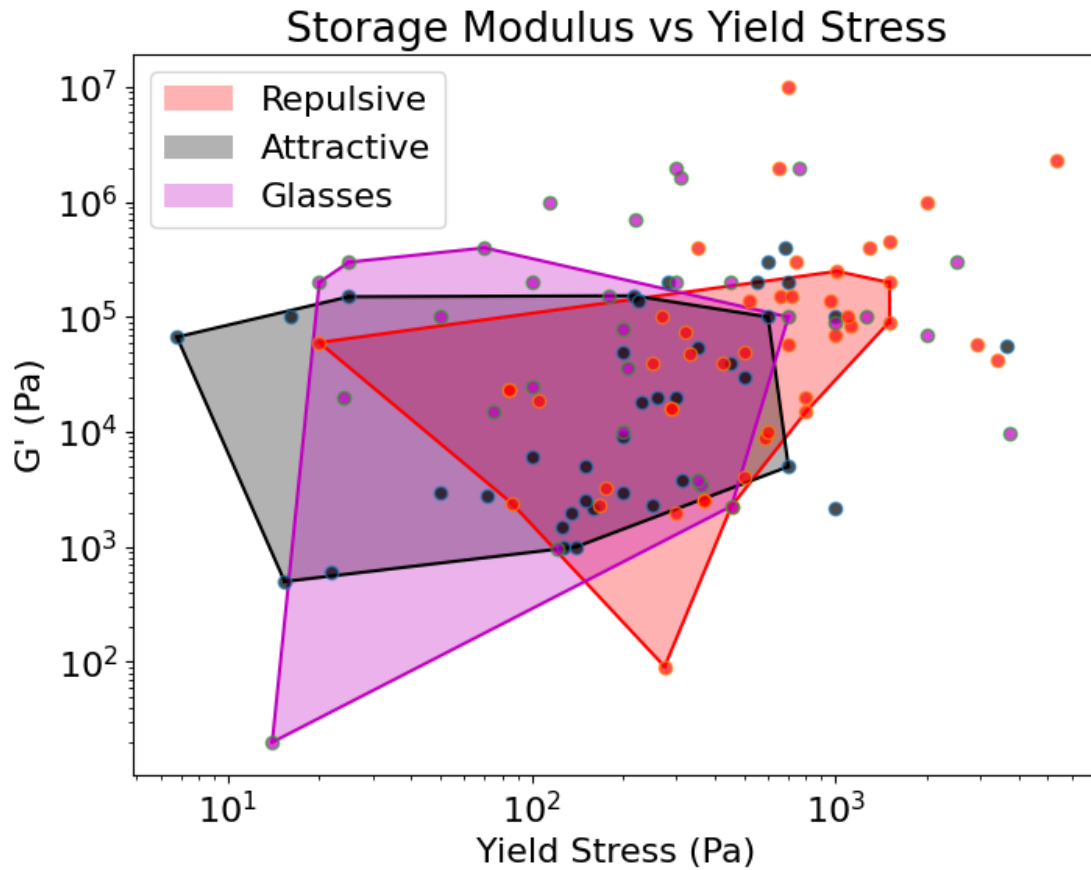


Figure 27: Storage modulus - static yield stress Ashby-like plot.

Furthermore, we explore the printability constraint adopted by *Chen et al.*, which proposes a product relationship between the storage modulus and yield stress ( $G' \cdot \tau_y = C$ ). For their work, the linearly discriminating line, which captured 91.8% of the printable data, had a slope of  $5 \cdot 10^6$ . This concept was applied to inks with attractive glass, repulsion dominated, and attraction dominated designations from the database (Figure 28 - Figure 30). Notably, the printable and non-printable boundary line slope varies depending on the yield stress fluid classification. As one progresses from attraction dominated fluids with low volume solids fraction to higher volume fraction attractive glass and repulsive inks, the boundary line increases, pushing the printable region further to the upper right. This result highlights the need for microstructural classification when discussing printability. The constant  $C$  is equal to

$5 \cdot 10^5$ ,  $1 \cdot 10^5$ ,  $1.5 \cdot 10^6$  for attractive glasses, attractive yield stress inks, and repulsive yield stress inks, respectively.

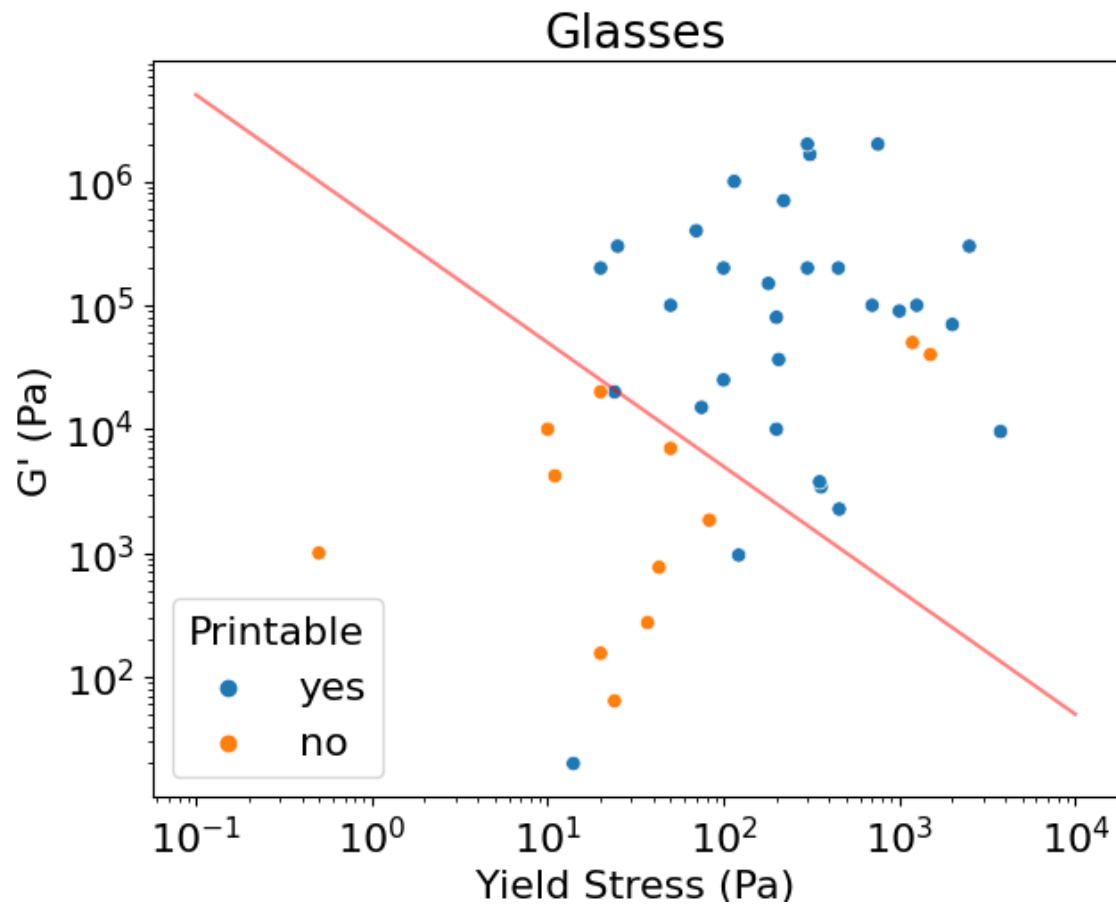


Figure 28: Printable and non-printable attractive glass designated inks. The boundary line has a slope of  $5 \cdot 10^5$ .

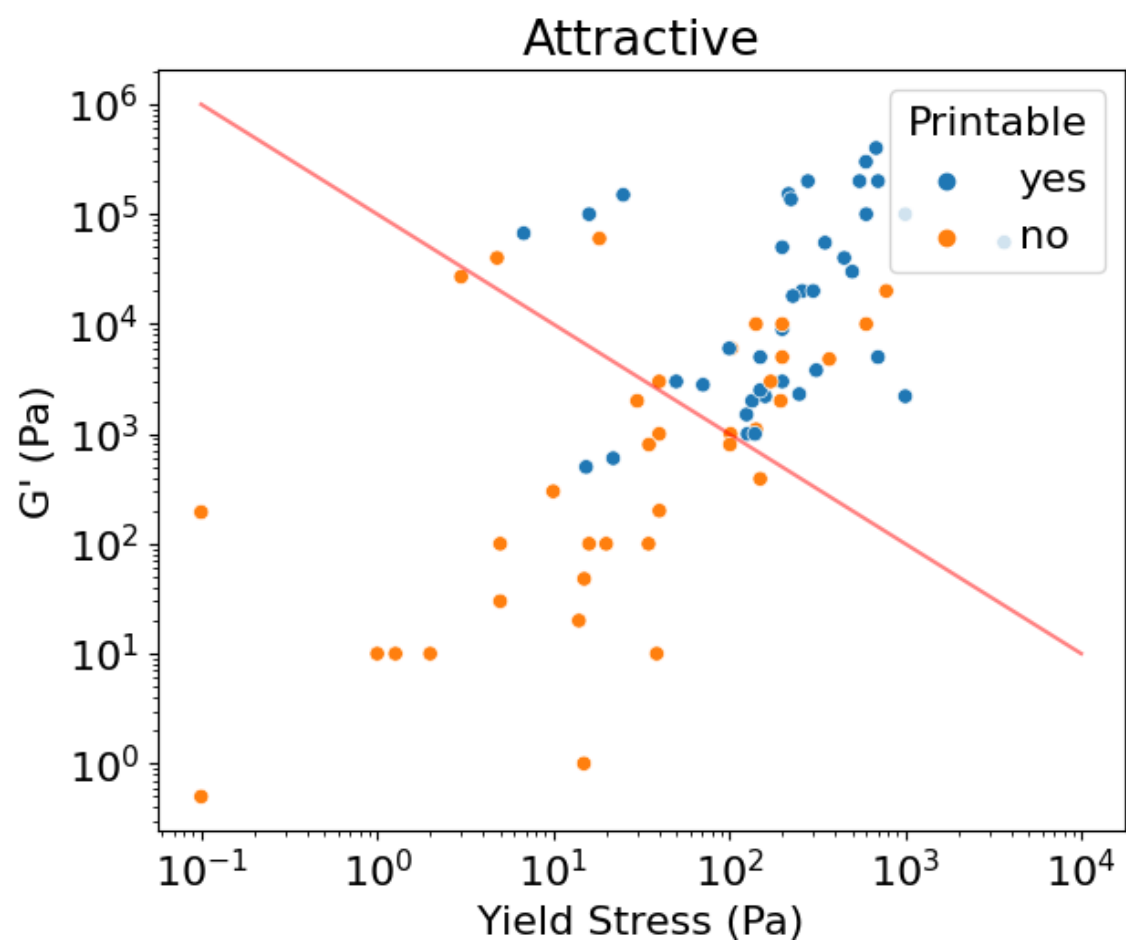


Figure 29: Printable and non-printable attraction dominated inks. The boundary line has a slope of  $1 \cdot 10^5$ .

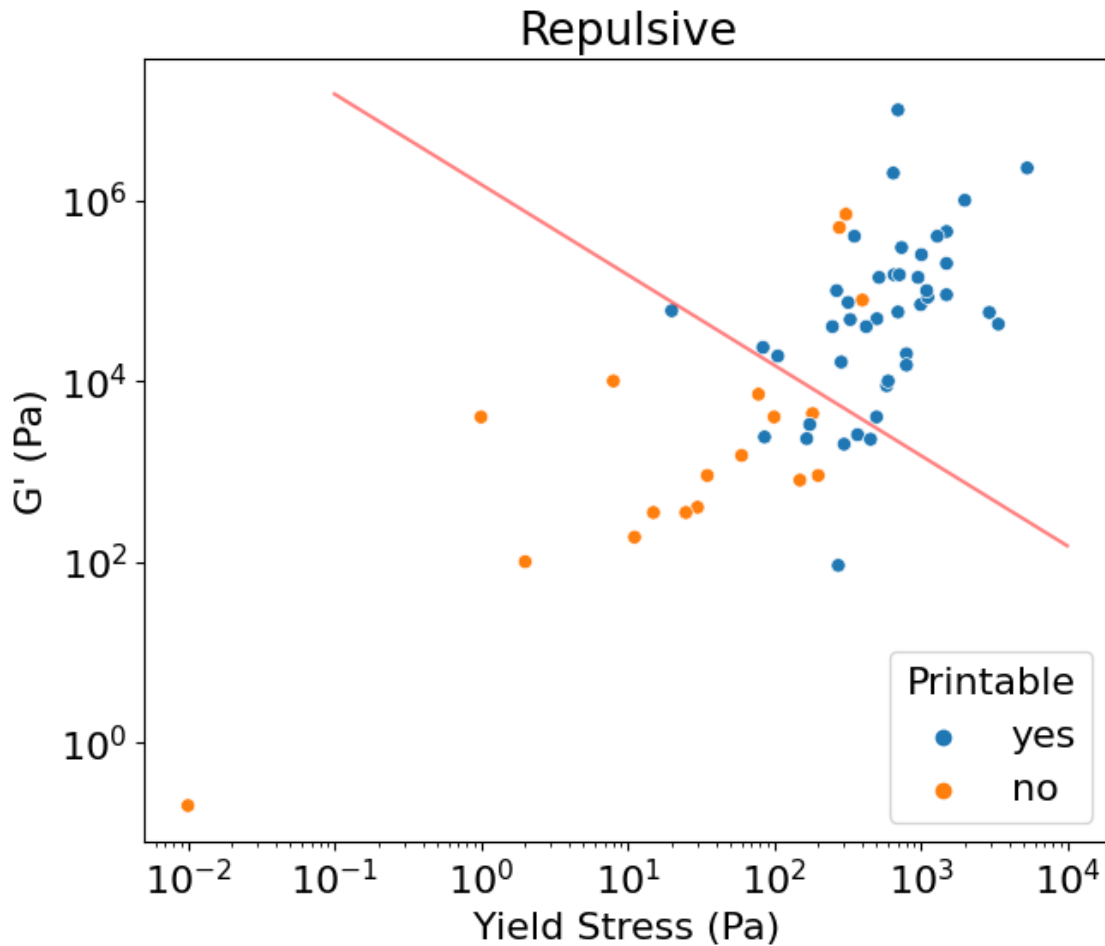


Figure 30: Printable and non-printable attraction dominated inks. The boundary line has a slope of  $1.5 \cdot 10^6$ .

To further aid visualization, Figure 31 depicts the  $G' - \tau_y^{stat}$  relationship for ‘purely’ repulsive and ‘repulsion dominated’ yield stress fluids. Inks in this region include nearly purely jammed inks, such as the copper ink (see chapter 4), and repulsion dominated suspensions, which include high particulate volume fractions in viscoelastic binders such as hydrogels. Though spanning a similar range of static yield stress, the storage modulus of printable strongly repulsive yield stress fluids tends to be higher by a half order of magnitude. In many instances, the transition from repulsion dominated to ‘purely’ repulsive is attained through increasing the particle volume fraction, utilizing a low binder volume fraction, or a comparatively less viscoelastic binder. For example, switching from a hydrogel such as xanthan gum to a polymer

such as ethyl cellulose while maintaining or increasing volume fraction will likely push the composition towards high storage moduli.

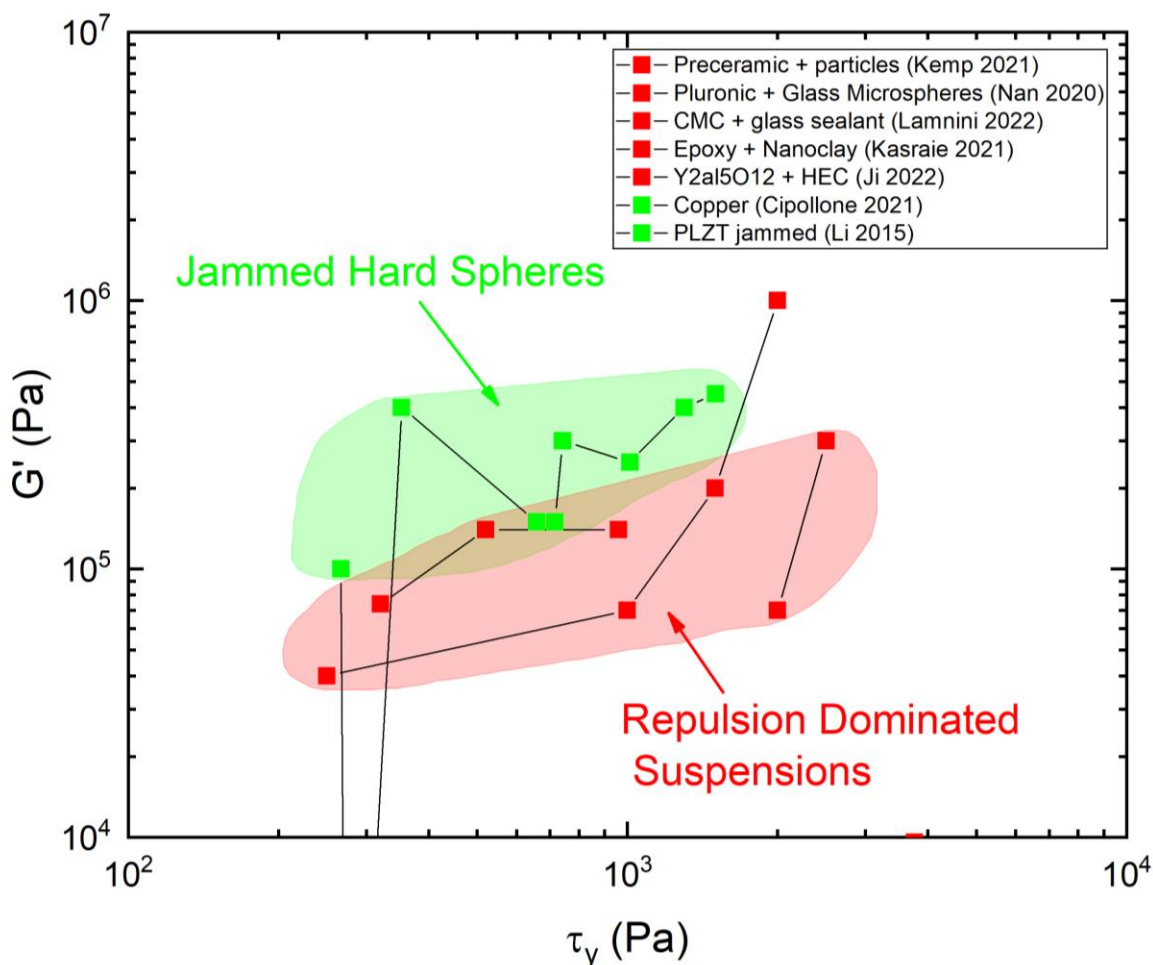


Figure 31: Storage modulus versus static yield stress for repulsive and repulsion dominated printable DIW inks.

Finally, Figure 32 details a higher resolution plot of attractive and attraction dominated printable yield stress fluids. Compared to the repulsive inks, which typically contain  $> 1$   $\mu\text{m}$  particles and a binder, the attractive categories are more diverse. Broadly, the inks tend to have lower static yield stresses by 0.5 -1 order of magnitude. Likewise, the storage moduli tend to be lower than repulsive fluids by 1-2 orders of magnitude. However, as the fluid transitions to the attractive glass region, the storage moduli compare to that of the repulsive fluids.

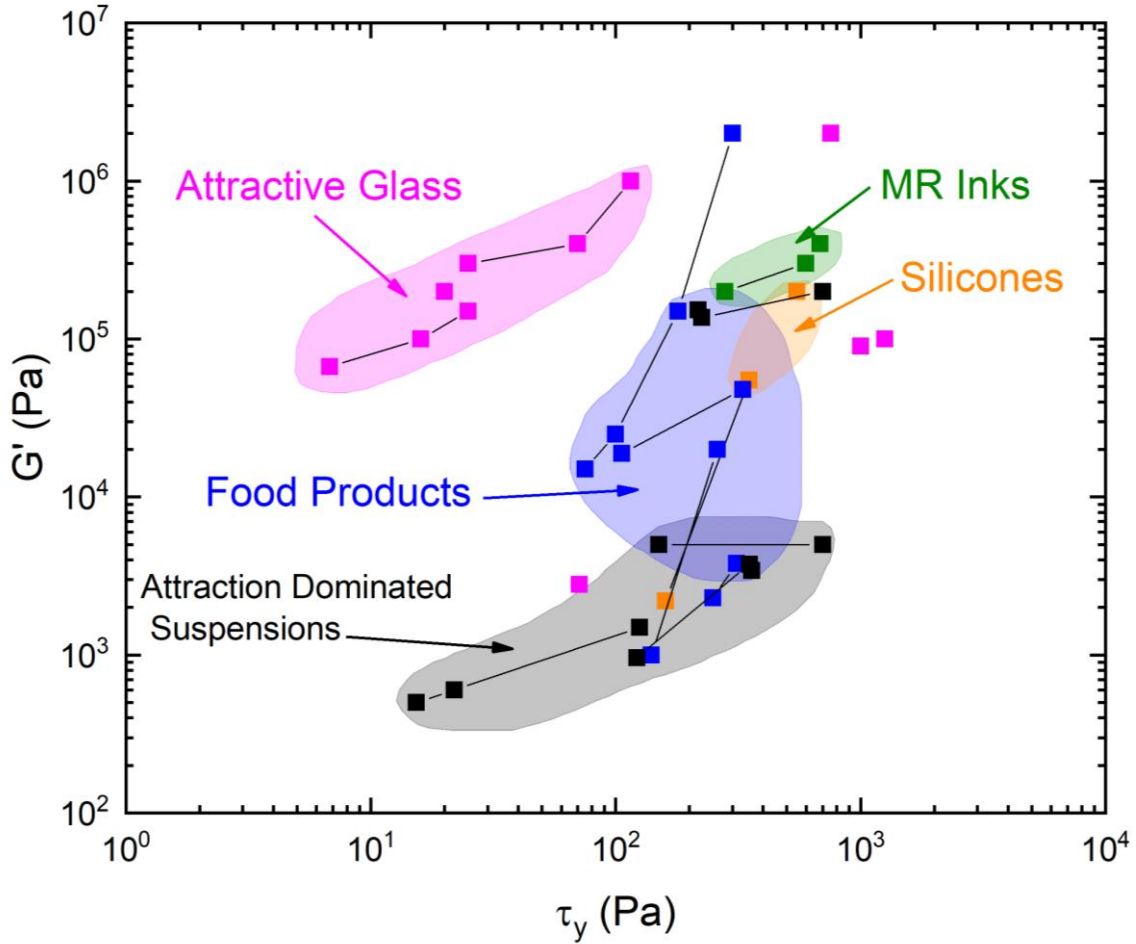


Figure 32: Storage modulus versus static yield stress for attractive and attraction dominated printable DIW inks.

In the lowest printable storage moduli regions exist attraction dominated suspensions and solubilized polymers/hydrogels. This region features comparatively high yield stresses, but low storage moduli, owing to the attractive networks dominating the strain behavior and low-volume particulate phases, which minimally impact the storage modulus. In the upper left corner, the magenta attractive glass regions ceramic colloidal inks with volume fractions of approximately 50%. In this region the yield stress is the result of attractive particle interactions and the high-volume fraction, giving them a storage modulus comparable to jammed inks, but static yield stresses like attraction dominated suspensions. Finally, silicones such as PDMS and GE silicone occupy an intermediate region with both high static yield and stiffness. Additionally, magnetorheological inks such as the one synthesized by *An et al.* occupy a similar static yield

space, but higher storage modulus.<sup>100</sup> For this specific ink, the binder was a polystyrene, with approximately 10% volume NiZn particles.

### 3.3.2 Shear Thinning Index versus Static Yield Stress

When the shear thinning index  $n < 1$ , the fluid is non-Newtonian. With relatively larger values of  $n$ , as is seen in the attractive systems, the experienced shear stress will increase more rapidly as the shear rate varies (considering the Herschel-Bulkley equation). Within Figure 33, the attractive fluids tend to occupy shear thinning indices ranging from ~0.5-0.9. As the static yield increases for the systems (due to the dependence of yield stress on particle volume fraction) progressing from attraction dominated to repulsion dominated fluids, the shear thinning index decreases. Similar trends were observed by *Nelson et al.*<sup>69</sup>

However, the nature of shear thinning behavior within highly loaded suspensions is still unclear. Generally, the shear thinning ability of a fluid is influenced by the flow response of the interstitial fluid and to a lesser degree by the particle volume fraction and size.<sup>101</sup> *Wilms et al.* demonstrate that suspensions of PEG, gum Arabic, wax, and sodium alginate tend to become more shear thinning as solid volume fraction increases.<sup>96</sup> They attribute part of this decrease to particle anisotropy, which enables shear alignment and further breaks down agglomerates. However, in DIW, solid volume fractions are typically maximized in pursuit of application compatibility, which further complicate the system through the effects of crowding and interparticle attraction. *Papadopoulou et al.* demonstrate that both friction and adhesion play a role in non-Brownian high volume fraction suspensions ( $\Phi > 0.5$ ).<sup>102</sup> In their system, the silica particles interacted strongly with a polar solvents. Interestingly, here, only rough silica particle suspensions display marked shear thinning, owing to increased frictional contact. On the other hand, in a non-polar solvent, with which the particles did not interact strongly, pronounced shear thinning was observed for both smooth and rough particles. It is hypothesized that particles covered by a solvation layer (*i.e.*, particles that more strongly interact with the interstitial fluid), do not experience 'direct' interparticle contact, and thus do not exhibit shear thinning behavior. In these cases, the shear thinning index of the suspension is very similar to that of the solvent. *Wilms et al.* further demonstrate semi-empirically that larger changes in the shear thinning index occur with increasing particle fraction when the shear thinning index of



the suspending liquid is relatively large ( $n_{liquid} > 0.5$ ), or the interstitial fluid is Newtonian.<sup>96</sup> Within DIW, common solvents include water, alcohols (*i.e.*, ethanol, isopropanol), and mildly shear thinning polymer solutions. In these cases, a decrease in shear thinning index with increasing particle volume fraction (*i.e.*, a transition from attraction dominated polymer solutions to repulsion dominated high volume fraction suspensions) is expected. The Ashby-like plots (Figure 33) and database analysis support this hypothesis for inks classified as repulsion dominated fluids. Moreover, the moderately strong shear thinning behavior of attractive glasses, which feature interparticle attraction and likely some degree of agglomeration (in DIW systems), can be attributed to the interparticle friction.

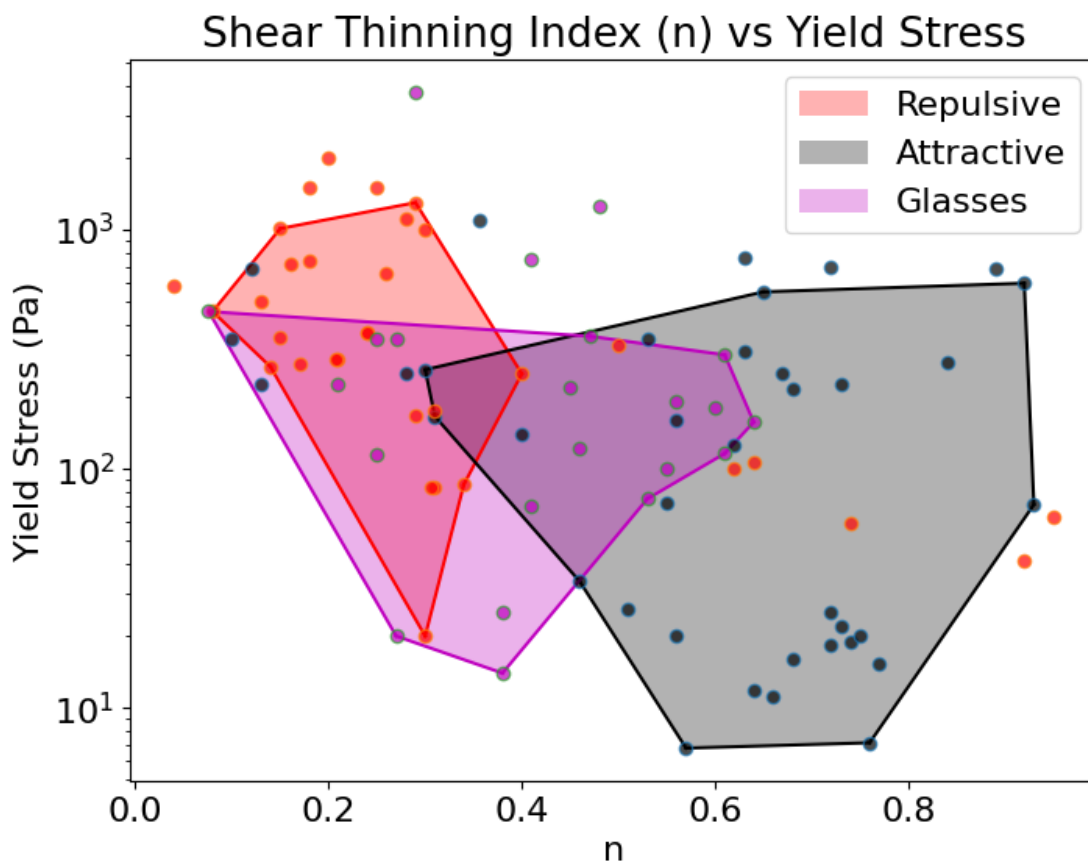


Figure 33: Ashby style co-plot of the shear thinning index vs. static yield stress for attractive, repulsive, and attractive glass printable inks.

Figure 34 displays an enhanced view of the attractive and attraction dominated DIW printable inks. As the systems transition from purely attractive (hydrogels, silicones, and weakly percolated networks), to attractive glasses (high volume fraction but attractive colloidal inks), the shear thinning index decreases. Again, many of the systems share a similar space of static yield stress, though printable attractive systems may have a lower static yield stress, on the order of  $10^1$ . Several systems, developed within the same study, can be seen to traverse the attractive region, well into and beyond the attractive glass region. This was the case with a colloidal chocolate syrup with increasing solids volume fraction.<sup>81</sup> As the volume fraction increases, and attractive network forces couple with jammed interactions, the yield stress increases while the shear thinning index decreases. This again highlights an important, and possibly the most important issue regarding printability – the rapidly changing microstructure.

Regardless, the ultimate choice of static yield stress will be application dependent, must conform to hardware constraints, and must be capable of filling spanning requirements. These plots, however, provide visual aid in either 1) selecting an appropriate microstructure, or 2) if working with a known microstructure, providing an optimization target for the shear thinning index. As we will see in a copper ink case study, blindly maximizing or minimizing the shear thinning index without microstructural context is sub-optimal.

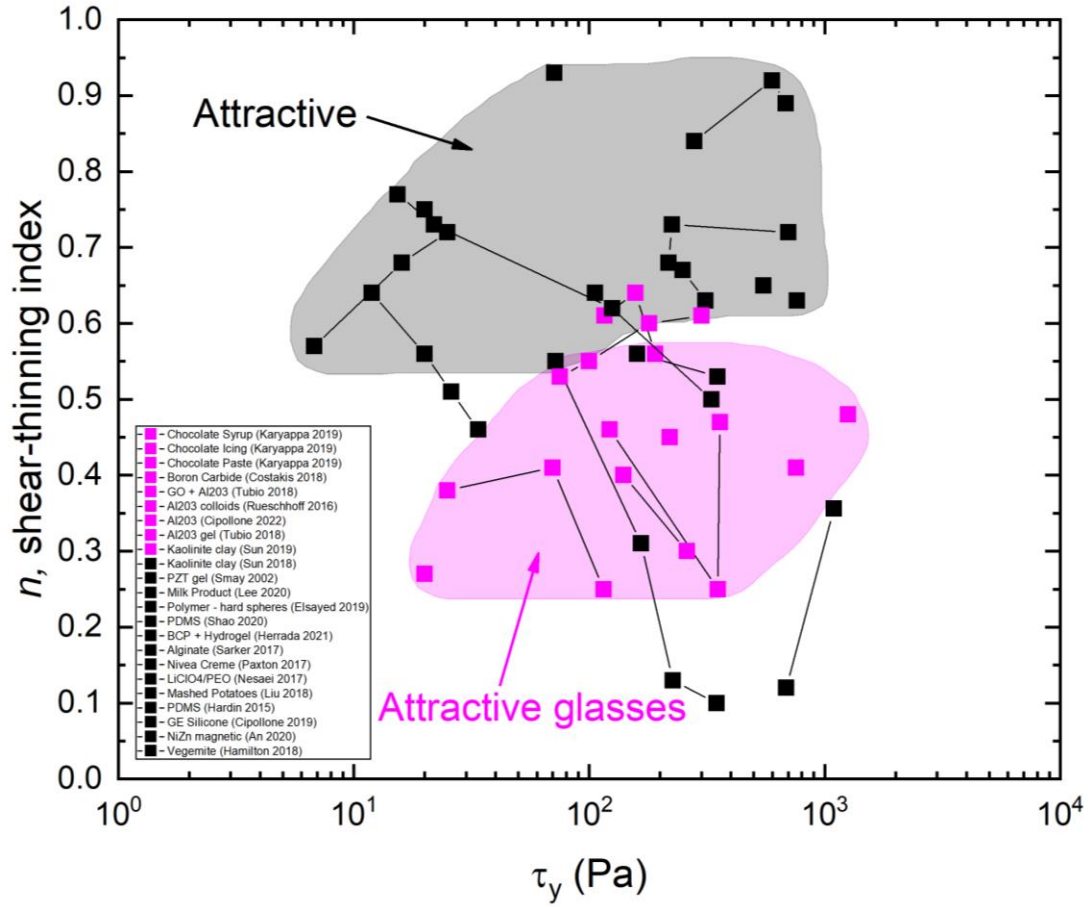


Figure 34: Ashby style co-plot of the shear thinning index vs. static yield stress for attractive and attraction dominated printable inks.

### 3.3.3 Critical Shear Rate versus Static Yield Stress

The consistency index,  $K$ , is the coefficient of the power-law component of the Herschel-Bulkley. Importantly,  $K$  possesses units of  $Pa \cdot s^n$ , where  $n$  is the shear-thinning index. As such  $K$  is dependent on  $n$  and cannot be used in its native form as a transferable metric. As mentioned in section 2.1.1, several authors, such as *Nelson* and *Jaworski*, have used a 'critical shear rate' to replace  $K$ , shown in a modified version of the Herschel-Bulkley equation (Equation 18).<sup>56,57</sup>

$$\tau = \tau_y \left[ 1 + \left( \frac{\dot{\gamma}}{\dot{\gamma}_c} \right)^n \right]$$

Equation 18

The critical shear rate,  $\dot{\gamma}_c$ , represents the shear rate at which the applied shear stress is twice that of the yield stress. Roughly, this stress translates to the stress at which the viscous forces dominate the shear properties. From analysis of 44 inks, the flow stress ( $G' - G''$  crossover), approximately corresponds to the point at which the shear stress is twice that of the static yield stress, and hence where the viscous behavior dominates the elastic behavior of the fluid. Ultimately, direct use of the critical shear rate allows one to mark the shear rate at which the flow stress (stress experienced by the ink in response to an applied shear rate) will deviate from the static yield stress by a factor of 2. Though this is a relatively new metric, *Nelson et al.* have mapped the critical shear rate for several yield stress fluids.<sup>57,69</sup> Figure 35 greatly expands on this work, and displays the critical shear rate for attractive, repulsive, and attractive glass printable DIW inks.

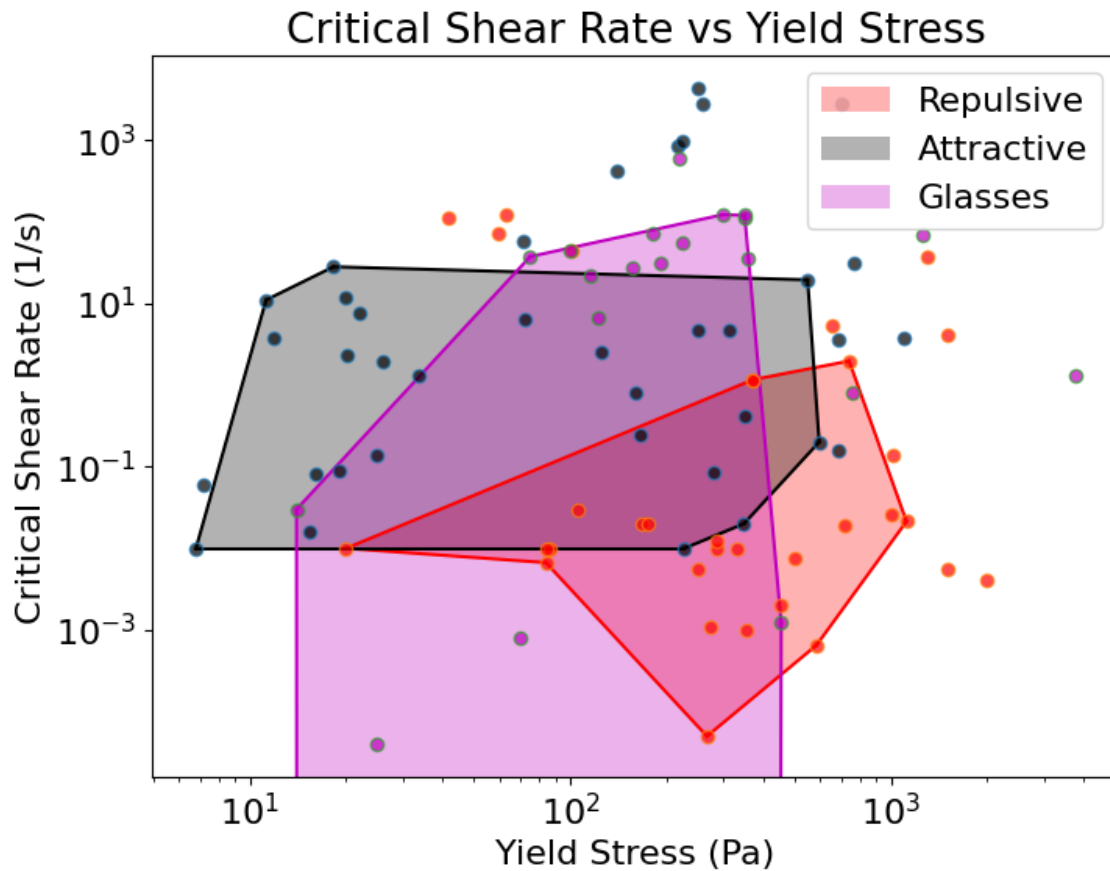


Figure 35: Ashby style co-plot of the critical shear rate versus static yield stress for repulsive, attractive, and attractive glass printable inks.

Across the printability space, critical shear ranges from  $10^{-4} - 10^3$ . Generally, and in agreement with *Nelson et al.*, repulsive systems tend to have lower values of critical shear rate but span nearly five orders of magnitude. As one transitions to attraction dominated systems, the critical shear rate tends to decrease and spans only three orders of magnitude. Finally, transition to the attractive glass region, the critical shear rate increases dramatically and concentrates on the orders of  $10^1 - 10^3$ . General insights about the steady state flow curves can be made from these plots, especially when coupled with the previous Ashby-like plots. For example, as the critical shear rate increases, the flow curves tend to flatten out as they are coupled with a decreasing shear thinning index.

Finally, if we consider the critical shear rate as a proxy for microstructural deformation, and the point at which the viscoelastic fluid has momentarily plastically deformed, we can infer properties of the ink microstructure. Attractive glasses undergo a two-step yielding process, in which the attractive bonds first break, followed by cage breaking.<sup>103</sup> These two inflection points on a stress-strain plot increase the ultimate strain and delay complete microstructural breakdown. This idea is reflected in the higher critical shear rates for attractive glass classified fluids in Figure 35. Interestingly, *Zhou et al.* note that within attractive glass systems, the first critical strain remains nearly constant, as it is a function of the attractive potential.<sup>103</sup> However, as volume fraction increases, the second critical strain decreases, eventually overlapping with the first critical strain, and emulate repulsion dominated glass behavior. At this point, the two yielding phenomenon occur simultaneously. This phenomenon could contribute to the lower critical shear rates demonstrated by repulsion-dominated systems in Figure 35.

### 3.3.4 What other Ashby plots may be useful?

In addition to the plots generated from the Herschel-Bulkley parameter and storage modulus, several other plots may guide an ink engineer depending upon the application. If print speed is a concern, and features need to be printed within a time constraint, extensibility and low brittleness may be a concern. Say also, you need to build features with a specific height, capable of supporting a defined stress. In this case, an Ashby coplot of  $\bar{E}$  vs.  $FTI$  may will provide candidate microstructures.

As the database expands, secondary printability metrics such as the FTI may be easily calculated. In fact, for formulations with a flow stress and static yield stress reported, the FTI exists in the current database iteration. For metrics such as  $\bar{E}$ , the community will need to adopt standard measurement of the dynamic yield stress and ink surface tension. The Ashby plots below provide relationships for future design scenarios.

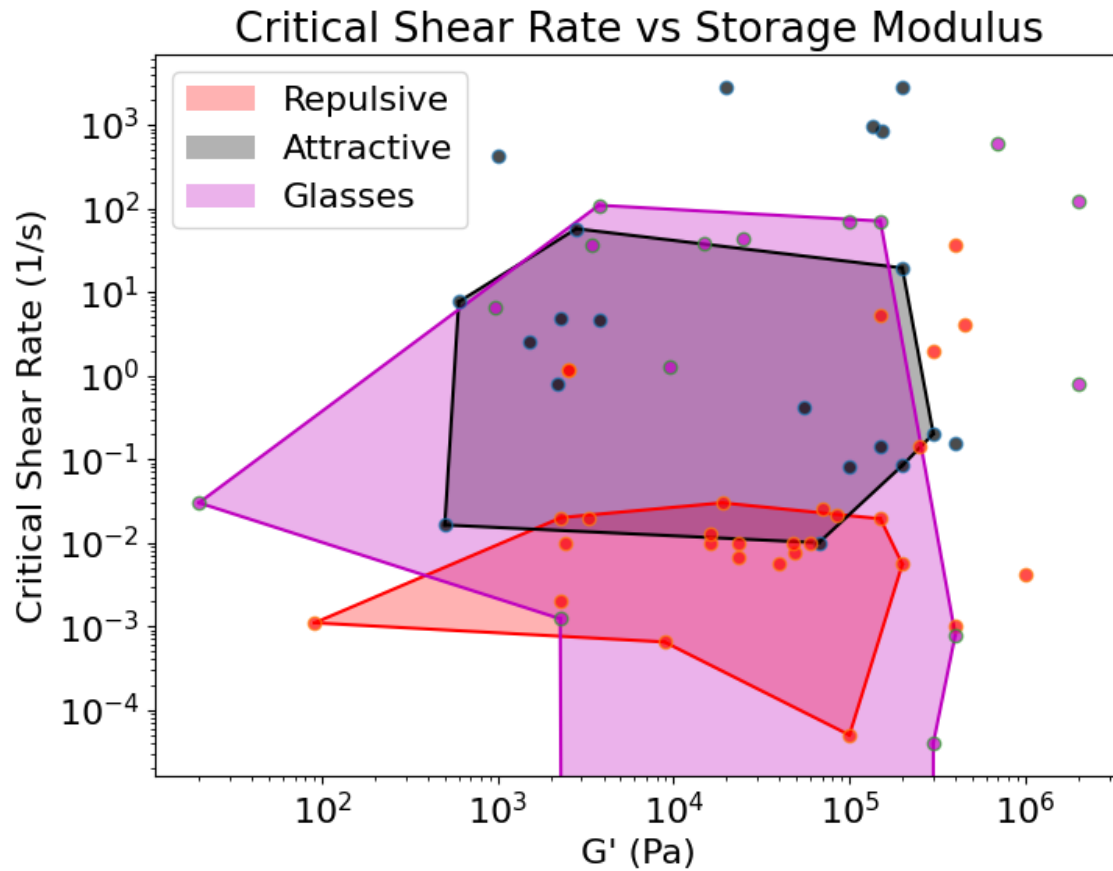


Figure 36: Ashby co-plot of the critical shear rate and storage modulus.

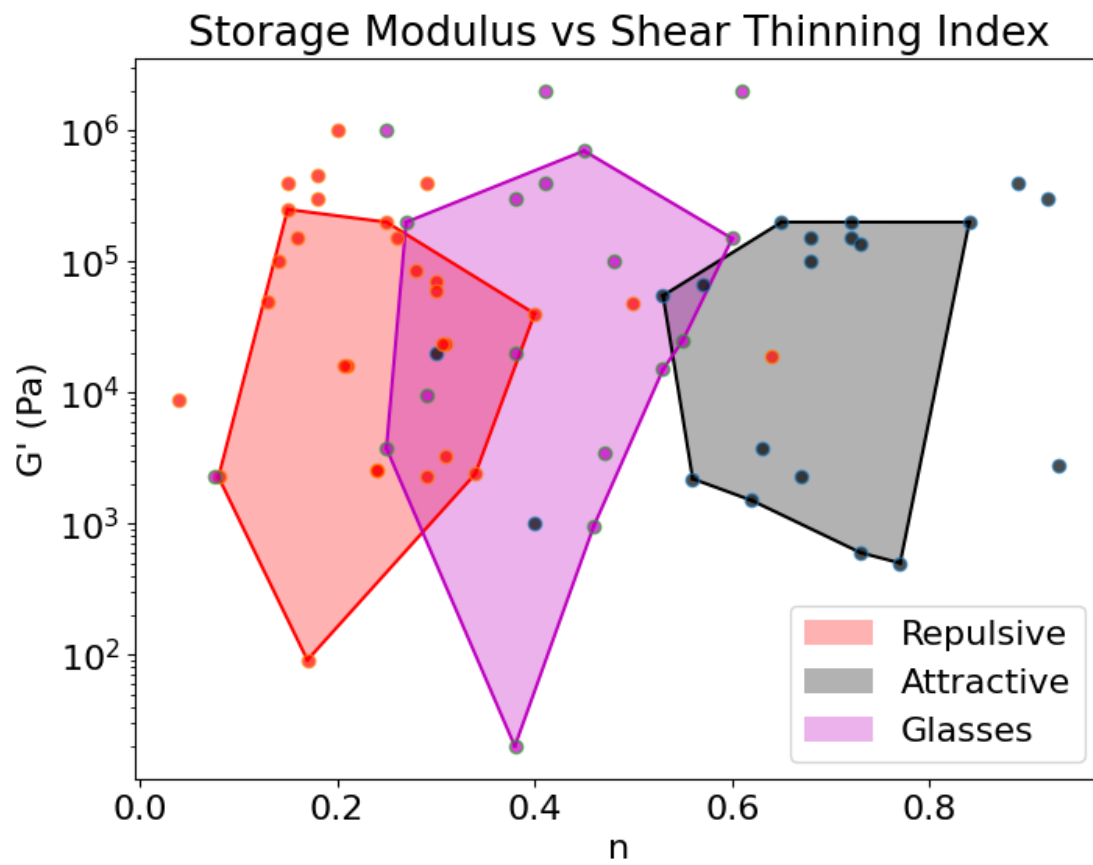


Figure 37: Ashby co-plot of the storage modulus and shear-thinning index.

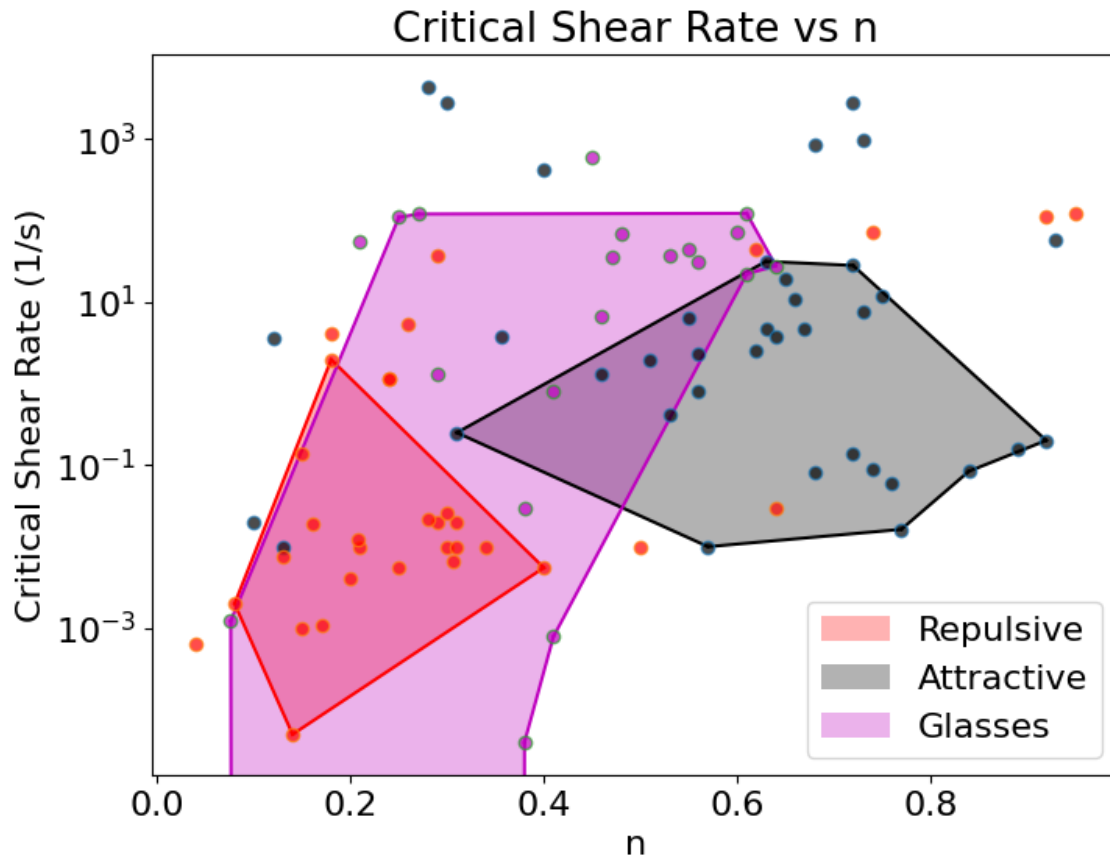


Figure 38: Ashby co-plot of the critical shear rate and shear-thinning index.

### 3.3.5 Additional Empirical Bounds

Several authors have recommended general rheological guidelines for printability.<sup>32,75,104,105</sup> However, a severe limitation is that these guidelines are developed using one or two ‘printability’ studies on one yield stress fluid microstructure. Hence, the yield stress fluid class is limited, and the definition remains highly local. This practice contributes to the uncertainty of printability and may be the source of debate between authors such as *Sun*, who finds variable printability regions for emulsions and clay suspensions.<sup>106</sup> To further the discussion, the printability rheological database is used to explore common bounds such as  $\tan(\delta)$  and the flow stress vs static yield stress ( $\tau_f$  vs  $\tau_y^{static}$ ), and provide class specific printability criteria.



Figure 39 shows the relationship between static yield stress and flow stress for the three major yield stress fluid classes – attractive, repulsive, and attractive glass dominant fluids. It is important to note the sample size of this plot is less than that used to generate the Ashby style co-plots. However, some trends can be identified. These trends are summarized in Table 11.

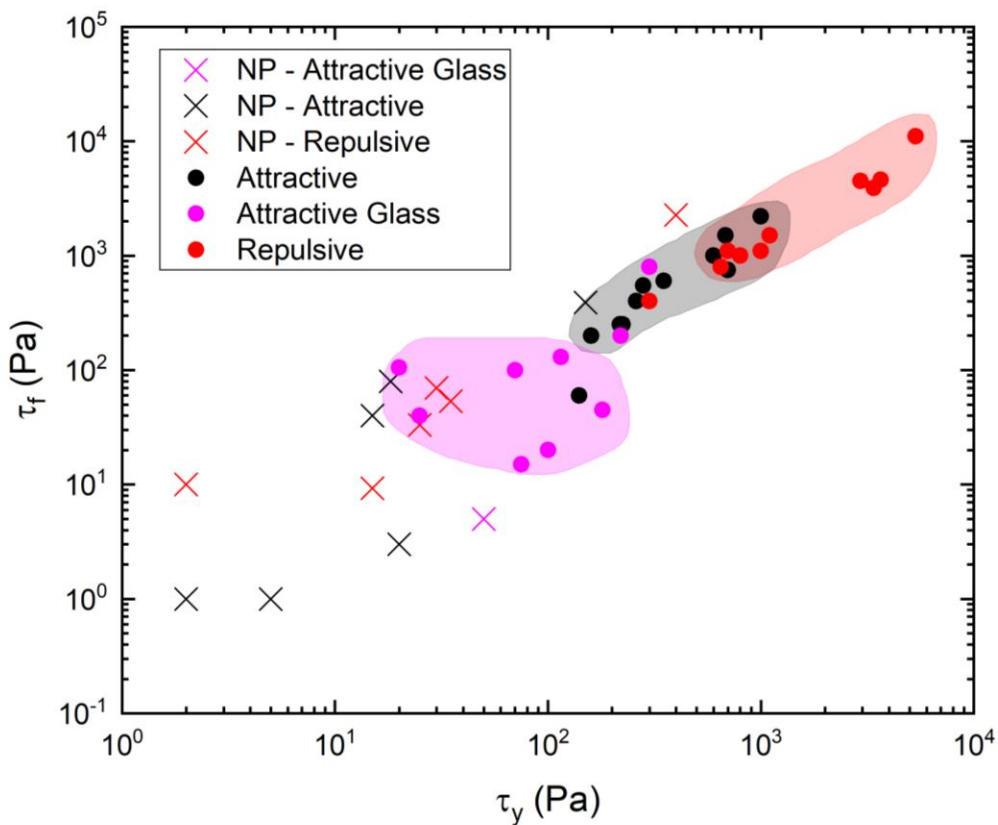


Figure 39: Flow Stress vs Static Yield Stress for printable (circles) and unprintable (crosses) by general yield stress fluid class.

Table 11: Printability minima for the flow and static yield stress for attractive, repulsive, and attractive glasses dominant inks.

Ink Class	$\tau_y^{static}$ (Pa)	$\tau_f$ (Pa)
Attractive	> 50	> 60
Repulsive	> 100	> 200
Attractive Glass	> 700	> 800

Figure 40 shows the relationship of flow stress and static yield stress for printable formulations, irrespective of yield stress class. From a linear fit, the flow stress is approximately 1.65 times that of the static yield. When employing the critical shear rate – the shear rate at which the induced stress is twice that of the static yield stress – one can reasonably presume the ink is a regime in which viscous forces dominate and the loss modulus has crossed the storage modulus. Therefore, the ink is in a dominantly viscous state.

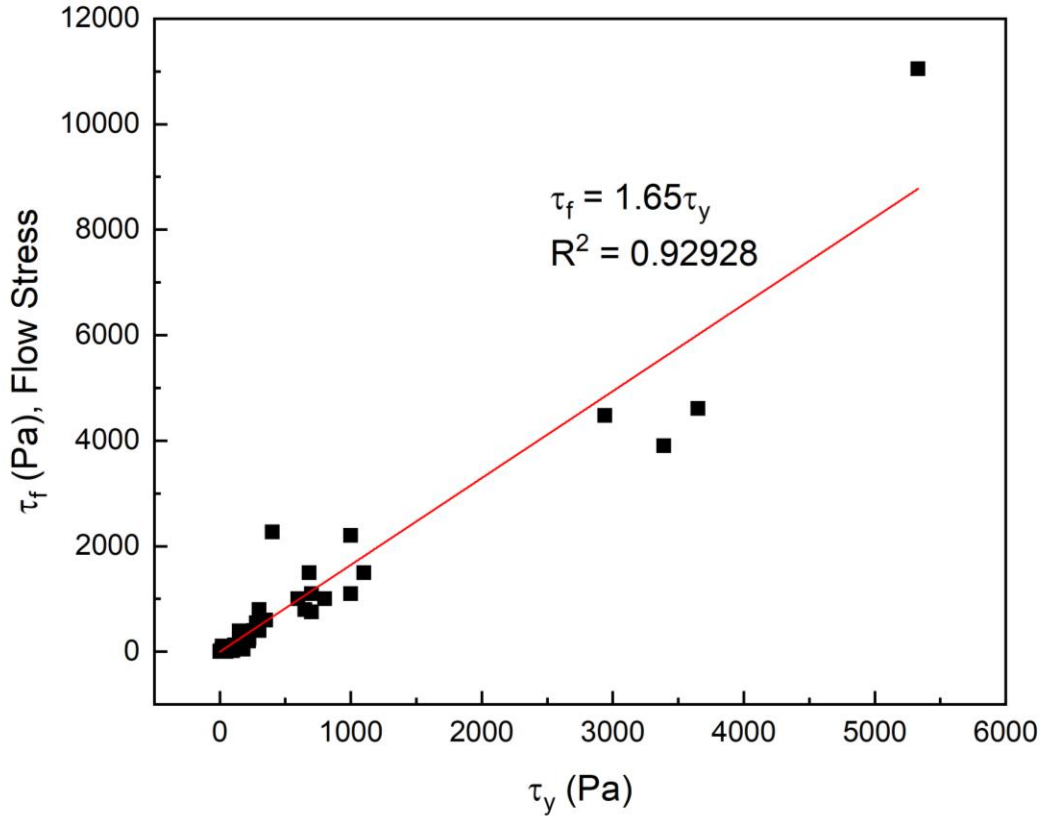
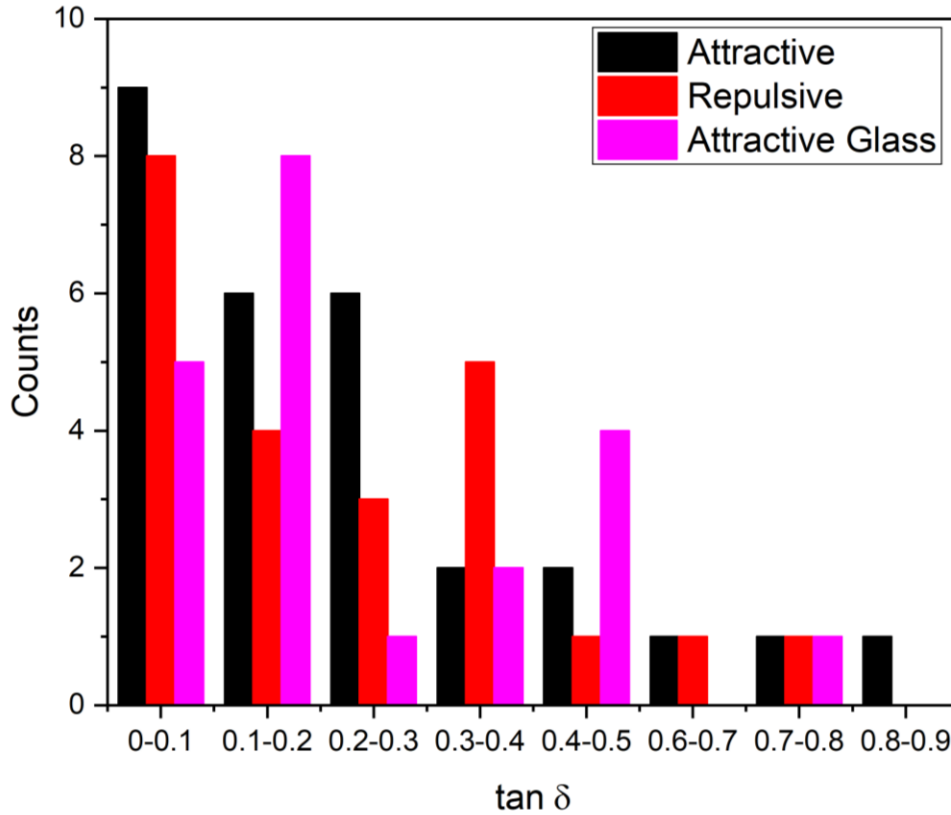


Figure 40: Empirical linear fit of flow stress and static yield stress. For printable formulations the flow stress is approximately 1.65 times that of the static yield.

Lastly, *Wilt et al.*, have noted that printable formulations tend to feature values of  $\tan(\delta) < [0.8 - 1]$ .<sup>107</sup> Figure 41 supports this observation, noting nearly all printable formulations feature a  $\tan(\delta) < 0.8$ . Notably, clusters of printability for all three major yield stress fluid classes occur when  $\tan(\delta) < 0.2$ , suggesting strongly dominant elastic behavior at rest or low strain. It must be noted, the data for this plot was *not* collected at a constant frequency. Typically,  $\tan(\delta)$  should be studied as a function of oscillation frequency. Here, the

storage and loss modulus were taken from the linear viscoelastic region during an oscillatory strain or stress sweep. Commonly for these studies, the oscillation frequency is fixed at 1 Hz, or 6.28 rad/s, though it can vary. The purpose of this figure is not to be definitive, but to help establish empirical bounds for a range of printable formulations.



*Figure 41:  $\tan(\delta)$  bins for printable yield stress fluids.  $\tan(\delta)$  was calculated using the storage and loss modulus of the linear viscoelastic region. Most measurement frequencies are  $\sim 1$  Hz, though may vary slightly. This plot is to be used as a general guideline and source of future work.*

### 3.4 Conclusions

Ultimately, the Ashby-like plots and empirical printability guidelines illustrated above will provide ink engineers target rheological parameters for a given yield stress fluid microstructure. Until this point, rheological optimizations and selections were performed iteratively and ad-hoc. These ranges will not only reduce experimental time and the need for conventional analysis of materials but enable them to identify novel yield stress fluid microstructures and composites.

However, a few limitations of the work must be addressed. Broadly, one can break down the DIW process into five steps: 1) extrusion, 2) nozzle exit, 3) surface impingement, 4) surface adhesion and ambient drying, and 5) post-processing. The Ashby-like plots presented in this chapter address the challenges of steps 1 and 2, and broadly enable success for steps 3-5. Spanning and three-dimensional capability may be loosely included in steps 3 and 4. However, these steps further include effects of the ink surface tension and substrate surface energy. Essentially, the parameter space of DIW quickly grows as one considers the entire processing space. While not an all-encompassing solution, we believe this work pushes DIW ink engineering in a more sustainable and mature direction. The following chapters - Chapter 4, and Chapter 5 - demonstrate the utility of the Ashby-like plots in the synthesis and implementation of a repulsion dominated copper ink and attractive glass alumina formulation. The work follows the four-stage design template of Ashby and intends to serve as case studies for design within DIW ink engineering.<sup>93</sup>

## 4 Repulsive Yield Stress Case studies

### 4.1 Introduction

Here, we aim to engineer a 3D porous copper current collector for solid-state lithium metal batteries. Copper serves as a common current collector within battery systems. However, solid-state lithium metal batteries are prone to lithium dendrite formation, which leads to premature failure of the battery. The dendrites result from the planar, heterogeneously wet interface of the solid electrolyte and electrode which then leads to the inhomogeneous deposition of Li on small protuberances guided by a non-uniform current density.<sup>108</sup> For reference, in liquid or gel-electrolyte batteries, the charge density is homogenous from complete wetting of the electrolyte-electrode interface.<sup>109</sup> The drawback however, especially for liquid electrolyte cells, is safety, stemming from the risk of leakage and electrolyte flammability.<sup>45</sup>

Solid state batteries offer improved safety, replacing all liquid components with solid, stable components. In contrast, utilization of a 3D porous current collector or scaffold, which transforms the planar Li metal anode to a 3D structure, has shown to be an effective strategy to suppress dendritic lithium and to accommodate the Li volume changes.<sup>110,111</sup> *Yun et al.* utilized

this concept to reduce the spatial inhomogeneity in charge distribution and local current density, inducing a more uniform Li ion flux.<sup>108</sup>

DIW is an efficient approach to fabricate 3D architectures facilely and accurately, providing a route to rapidly explore different structure–property relationships at a range of length scales.<sup>112</sup> 3D printing also allows for patterning of the inks directly onto the ceramic electrolyte, providing an intimate interfacial electrode/electrolyte contact. To that end, we explored the 3D printing of a copper scaffold on the solid-state LATP electrolyte as a current collector and dendrite inhibitor for Li metal anodes.

## 4.2 Copper Ink Design

As outlined in Chapter 3, the design process follows three basic steps: 1) the problem statement, 2) the model, 3) material selection, and 4) the post-script. The following sections detail the hybrid design approach implemented for copper ink synthesis and implementation. Several of the key design elements were utilized, but the infrastructure for materials selection was (more or less) non-existent at the time. As such, sections will take on the shape of a post-script, with a proper design strategy outlined at the end of the chapter.

## 4.3 Hybrid Design Approach

In this work, first, the performance criteria of the ink, irrespective of microstructure and rheological targets, were determined. These include gap spanning ability, print fidelity (filament diameter), and processability (limited clogging). The ink also needed to conform to the post processing regimen, which includes a binder burnout at 550 °C. Moreover, the final microstructure must feature a hierarchical porosity to enhance lithium dendrite caging. Macroporosity was to be guided via the DIW patterning, while meso- and micro-structure dictated by interparticle pores.

Without explicit intention for *DIW design*, we employed a hybrid analysis-design approach (Figure 42). In inverse *design*, performance specifications are stated and related to the rheological properties. From here, the microstructure may be selected. Though more flexible, the step of relating microstructure to rheological properties remains a significant challenge, and the crux of this thesis. As an aside, this step cannot happen without Ashby-like

plots and an understanding of the rheology-microstructure relationships, which are two of the significant contributions of this thesis.

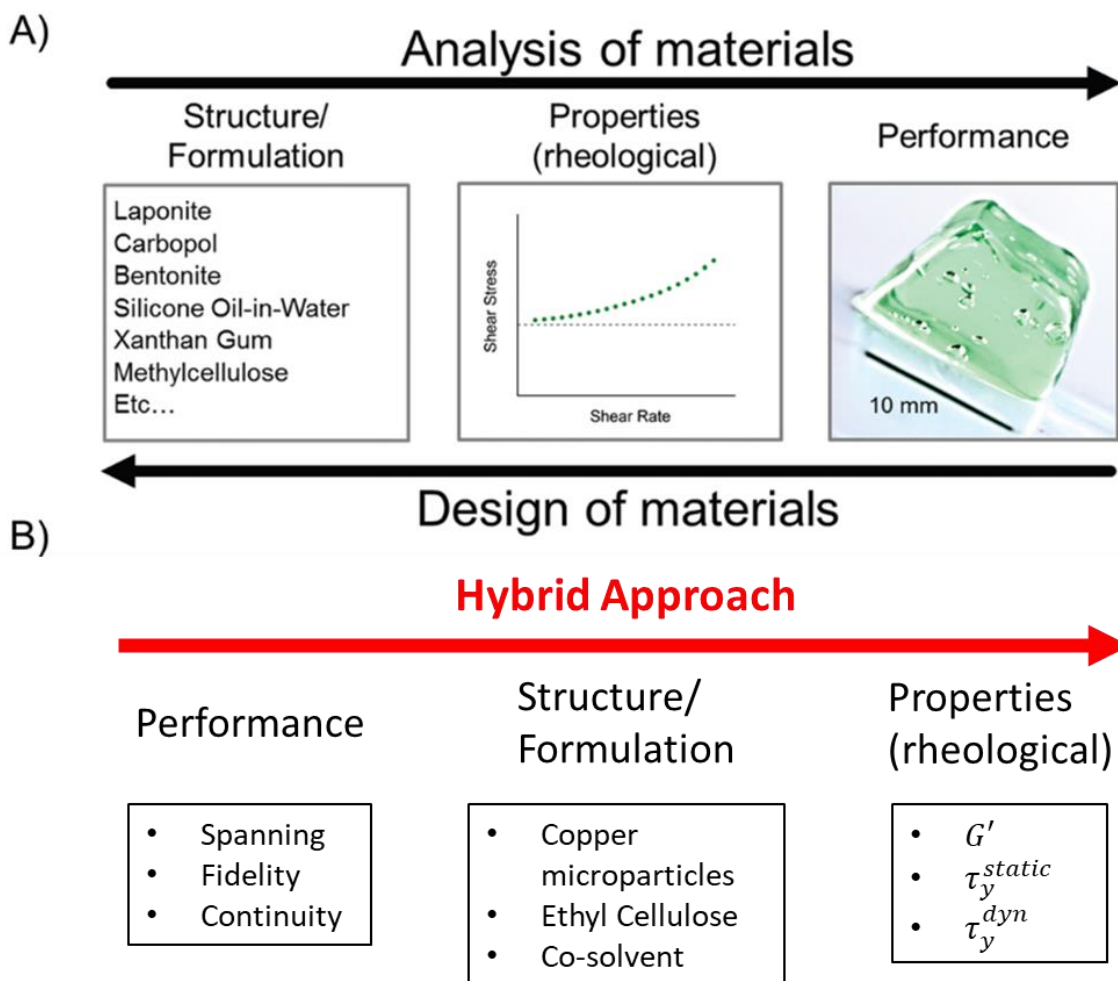


Figure 42: a) Analysis of materials versus design of materials. Analysis begins with a structure, analyzes the properties, and relates them to performance. Design works backwards, first specifying the performance requirements, and ultimately identifying a microstructure.<sup>57</sup> The hybrid approach (b) was used for the copper inks. Performance specifications were made, but the rheological properties were tied to a ‘pre-selected’ microstructure.

Within our hybrid approach, the microstructure was selected following definition of the general performance targets. To ensure scaffold integrity and conductivity (i.e., percolation) after post-processing, the yield stress fluid required a high-volume fraction of copper. Initially, nanoparticles were considered, which in hindsight, would provide significant fluid

microstructural design freedom. However, microparticles (10  $\mu\text{m}$ ), were thought to better resist oxidation during both ambient and post-processing. As a note, it so happened that the chemical transformation and subsequent copper oxide reduction, was pivotal in chemically and mechanically stabilizing the electrode-electrolyte interface.

With the microstructure selected (jammed repulsion-dominated ink), the hybrid approach then focused on the identification of first and second order rheological parameters and their optimization. Essentially, we asked ourselves: what rheological properties are important and what models currently exist to guide optimization? Table 12 shows the selected properties and optimization targets.

*Table 12: Targeted rheological parameters and their optimizations.*

Parameter	Reason	Target Range
Dynamic yield stress	Support subsequent layers	$\sim 10\text{-}1000\text{ Pa}$
Static yield stress	Enable extrusion with pressure constraints	$< 8.6\text{ kPa}$
Storage modulus	Enable spanning filaments	$> 70\text{ Pa}$
Shear-thinning index	Enable flow through fine nozzles	Minimize, $> 0$

However, these rheological targets were selected from various literature sources, with variable microstructures. For example, the target level dynamic yield stress was determined using attractive glasses<sup>113</sup> and the storage modulus criteria was devised using model colloidal gels.<sup>53</sup> Interparticle attractive forces are contribute to network formation in these inks, in combination with caging for attractive glasses. At this point in the hybrid design approach, a yield stress fluid was a yield stress fluid – little to no attention was given to the yield stress mechanism and the yield stress fluid subgroupings proposed herein.

Finally, the performance targets were quantified and qualified. These will be referred to as the performance metrics. Briefly, the performance metrics of the ink reduced to: (i) the Herschel-Bulkley shear thinning index, (ii) the dynamic yield stress, (iii) the static yield stress, (iv) ink stiffness  $G'_{LVR}$ , (v) line continuity, and (vi) % Spreading. Thus, the shear thinning index  $n$

should be minimized, as values approaching zero signal increased shear thinning behavior and enable flow through fine nozzles. Again, the dynamic yield stress of the ink must be tailored to achieve a level which allows for self-supporting features and minimal deformation after printing. This target level yield stress described by *Franks et al.* typically ranges between ~100-1000 Pa.<sup>113</sup> The static yield stress should be less than the maximum given the hardware. With a maximum pressure of ~4.3 MPa reliably produced by the pressure dispenser, a nozzle radius of 100  $\mu m$ , and a nozzle length of 25 mm, a maximum shear stress of 8.6 kPa develops at the wall. From this, the target level yield stress should range between ~0 – 8.6 kPa. A lower bound of the static yield stress was not specified. The required ink stiffness (storage modulus) to facilitate spanning features may be estimated from the relationship proposed by Smay:

$$G'_{LVR} \geq 1.4\rho^*s^4D \quad (3)$$

where  $G'_{LVR}$  is the ink stiffness,  $\rho^*$  is the specific weight of the ink,  $s$  is the reduced span distance ( $L/D$ ),  $L$  is the distance between the center of adjacent filaments, and  $D$  the filament diameter.<sup>53</sup> Ideally, with an aim of zero spreading ( $D = 200 \mu m$ ), 100  $\mu m$  pores ( $L = 300 \mu m$ ), and theoretical specific weights ranging from  $\sim 16.7 \cdot 10^3 - 50 \cdot 10^3 \frac{N}{m^3}$ , a minimum required stiffness can be set at ~70 Pa.

From these rheological constraints, we developed a mixture design problem determined from a literature review of common DIW ingredients and model ink formulations. The ink components – chosen without considerations for DIW design or their impact on microstructure – included 10  $\mu m$  copper particles, an ethyl cellulose binder system, and an ethanol-toluene co-solvent system. From this mixture, we aimed to maximize line continuity to enable continuous features and 3D geometries. Line continuity will be maintained when the ink possesses a robust, but not overly brittle, internal structure. In practice, maximizing continuity encourages high volume fraction formulations, and essentially eliminates attraction dominated fluids, save attractive glasses. Here, unknowingly, we were also designing for extensibility, as *Nelson et al.* have previously identified.<sup>57</sup> Finally, for an optimized ink, % Spreading must be minimized to allow for maximum printing fidelity and control. Ideally, an ink will exhibit zero spreading in



which the extruded filament has a diameter equal to that of the nozzle. This minimization was also a function of the processing parameters, which we visualize with processing maps.

Using the ink performance metrics of the Herschel-Bulkley shear-thinning index, the dynamic and static yield stresses, ink stiffness, % Spreading, and line continuity, an optimization problem is formed with respect to the weight percent of the ink constituents. These constituents include the solids loading, the binder solution, and the humectant, toluene, referred to as X1, X2, and X3, respectively. These ink constituents are subject to the mixture constraint:

$$X1 + X2 + X3 = 1$$

*Equation 19*

Initial boundary constraints for the ink constituents are established primarily through a literature review and preliminary experiments. The ink constituents, as weight percent, were initially bound as follows:

$$0.3 \leq X1 \leq 0.7$$

*Equation 20*

$$0.3 \leq X2 \leq 0.7$$

*Equation 21*

$$0 \leq X3 \leq 0.2$$

*Equation 22*

From here, a series of mixture experiments, rheological characterizations, and analysis-based printability experiments were performed. In total, 15 inks were mixed and assessed, with several being application compatible.

#### 4.3.1 Commentary

Overall, a hybrid design approach was taken, but the design objectives may have been too broad, or simply misguided. As Nelson stated, “a good functional objective cannot be too broad but cannot be over-specified as to be creativity stifling”. The creativity stifling aspect comes from the perceived “need” to use hard spherical 10 um copper particles. This was also a

constraint in part due to post-processing and stability concerns but were ultimately unfounded. The goal of the work was to produce a copper anode – not a copper or cuprous oxide anode. Generally, nanoparticles are more ambiently unstable and will quickly oxidize, requiring a reducing step (which was in fact adopted and helped to stabilize the interface chemically and mechanically). However, this foresight was not available at the time. Therefore, the microstructure was essentially bound to hard spheres suspended in a viscous polymer matrix. If nanoparticles were adopted, emulsions or colloidal gels could have been employed. Interestingly, with the goal of hierarchical porosity, an emulsion or foam may have been optimal. Previous work in our lab did focus on the development of printable titania foams, though the synthesis is non-trivial. The “need” to employ microparticles forces the hybrid approach and removes the concept generation phase, in which various yield stress fluid microstructures may be assessed for rheological compatibility. However, in pursuit of DIW *design*, these analytical trial and errors, and their associated learnings, are necessary. These trial and errors are what contribute to the Ashby-like plots presented in Chapter 3.

The other critically missing aspect of DIW design, addressed in the previous chapters – is that the functional objectives such as target yield stress and storage modulus – are absent for a given microstructure. Assembling the library of printability and the resultant Ashby plots allows one to simultaneously link the microstructure with the functional objectives. This process removes the need for analysis, or at the very least, minimizes the monotonous trial-and-error formulation analysis stage highlighted above. Having decided upon a jammed microstructure, in lieu of the fundamental spanning element model set forth by Smay and instead employing the  $G' - \tau_y$  Ashby plot, we could have set our  $G'$  optimization targets to  $10^5 - 10^6$ . This would have likely decreased experimental time and eliminated many of the low weight fraction inks initially analyzed.

Finally, it may have been overreaching to include processing objectives such as ‘line continuity’ or ‘% Spreading’ in the initial functional objectives. Upon revisiting these objectives, ‘line continuity’ is likely a function of both the extensibility of the fluid and the brittleness. Secondly, it is related to solids volume fraction, and consequently, in jammed formulations, the storage modulus. If one designs a highly extensible yield stress fluid, the processing space

expands, as the fluid can withstand higher printing speeds and more rapid directional changes without breaking. Though this was not initially considered, the elastic strain was used in this work to explain why inks – given the same constituents – were highly brittle, while others were highly ‘printable’. Likely, changes in the binder and solvent fractions shifted the microstructure from a strictly repulsive yield stress fluid to that of a blended repulsion-dominated fluid. For example, the jammed copper particles will dominantly contribute to the yield stress, while the cellulose polymer network contributes to the extensibility and ability of the ink to withstand deformation and reform the internal structure.

While writing the thesis, we revisited the copper ink synthesis to work through the ink engineering process utilizing Ashby-like plots and the method set forth by Ashby. The following sections present a condensed case study on formulating a repulsion dominated fluid utilizing design of materials principles.

#### 4.4 Design of Materials Approach

##### 4.4.1 Problem Statement

A copper scaffold is to act as a cage for lithium metal dendrites and bond to the ceramic electrolyte. The ink also needs to conform to the post processing regimen, with temperatures reaching a maximum of 600 °C. Moreover, the final microstructure must feature a hierarchical porosity to effectively suppress dendrite growth. Macroporosity is to be guided via DIW patterning, while microporosity dictated by interparticle porosity. Finally, the substrate measures  $5 \times 5 \text{ mm}^2$ . To provide appropriate surface area, the ink must be capable of printing three-dimensional structures and 3D grids. Grid spacing should similarly be as high resolution as possible. Pores approximately 300  $\mu\text{m}$  in diameter can be patterned using a 200  $\mu\text{m}$  nozzle. Therefore, the ink must be capable of spanning distances upwards of at least 300  $\mu\text{m}$ . Scaffold height is not a concern in this applications, because no more than two layers will be printed.

##### 4.4.2 The Model

Appropriate DIW rheological models are sparse, but models from Smay and M'Barki<sup>53,73</sup>, coupled with non-Newtonian fluid flow equations (see Appendix) to calculate the maximum shear stress during flow can provide guidance. With the need to span 300  $\mu\text{m}$ , the minimum

required storage modulus is 70 Pa. The required ink stiffness (storage modulus) to facilitate spanning features may be estimated from the relationship proposed by Smay:

$$G'_{LVR} \geq 1.4\rho^*s^4D$$

Equation 23

where  $G'_{LVR}$  is the ink stiffness,  $\rho^*$  is the specific weight of the ink,  $s$  is the reduced span distance ( $L/D$ ),  $L$  is the distance between the center of adjacent filaments, and  $D$  the filament diameter. Ideally, with an aim of zero spreading ( $D = 200 \mu m$ ),  $100 \mu m$  pores ( $L = 300 \mu m$ ), and theoretical specific weights ranging from  $\sim 16.7 \cdot 10^3 - 50 \cdot 10^3 \frac{N}{m^3}$ , a minimum required stiffness can be set at  $\sim 70$  Pa. Likewise, the maximum shear stress within a  $200 \mu m$  was 8.6 kPa, so the static yield stress of the formulation must be less than that value.

Finally, *Hernandez et al.* proposed an inequality to determine ranges of the shear thinning index ( $n$ ) and consistency index ( $K$ ) for power law and yield stress fluids. Fluid regions which satisfy the constraint will achieve a desired flow rate and satisfy extrudability constraints. To further generalize this model, and remove the dependence of  $K$  on  $n$ , we re-write the inequality using the critical shear rate:

$$\dot{\gamma}_{crit} \geq \frac{\tau_y^{1/n}}{\left(\frac{P_{max}R}{2L}\right)^{1/n} \left(\frac{\pi R^3}{Q_{min}}\right) \left(\frac{n}{3n+1}\right)}$$

Equation 24

where  $\dot{\gamma}_{crit}$  is the critical shear rate,  $P_{max}$  is the maximum applied extrusion pressure,  $L$  is the nozzle length,  $R$  is the nozzle radius,  $Q_{min}$  is the minimum target flow rate, and  $n$  is the shear-thinning index. However, there remain several unknowns. To determine a target flow rate ( $Q_{min}$ ), one can utilize the target printing speed and the nozzle area ( $Q = v \cdot A$ ). If the extrusion flow rate and stage relative flow rate are equal, towing or extrusion overflow are minimized. A minimum viable yield stress, irrespective of microstructure, can be determined from the database, and approximated as 100 Pa. Using a nozzle length of 14 mm and a desired

nozzle diameter of  $200\ \mu m$ , regions which satisfy the inequality can be highlighted on the Ashby-like plots. Table 13 highlights the function, objective, and design constraints.

*Table 13: Design table for 3D copper scaffolds.*

Function	<i>3D scaffold for batteries</i>
Objective	<i>High fidelity and Hierarchical structure</i>
Constraints	<p><i>(a) <math>200\ \mu m</math> nozzle</i></p> <p><i>(b) <math>\tau_{max} &lt; 8600\ Pa</math></i></p> <p><i>(c) <math>G' &gt; 70\ Pa</math></i></p> <p><i>(d) Compatible with high-temp post processing</i></p>

#### 4.4.3 The Selection

With the storage modulus and static yield stress as model criteria, we can now utilize the  $G' - \tau_y^{static}$  Ashby plot (Figure 43).

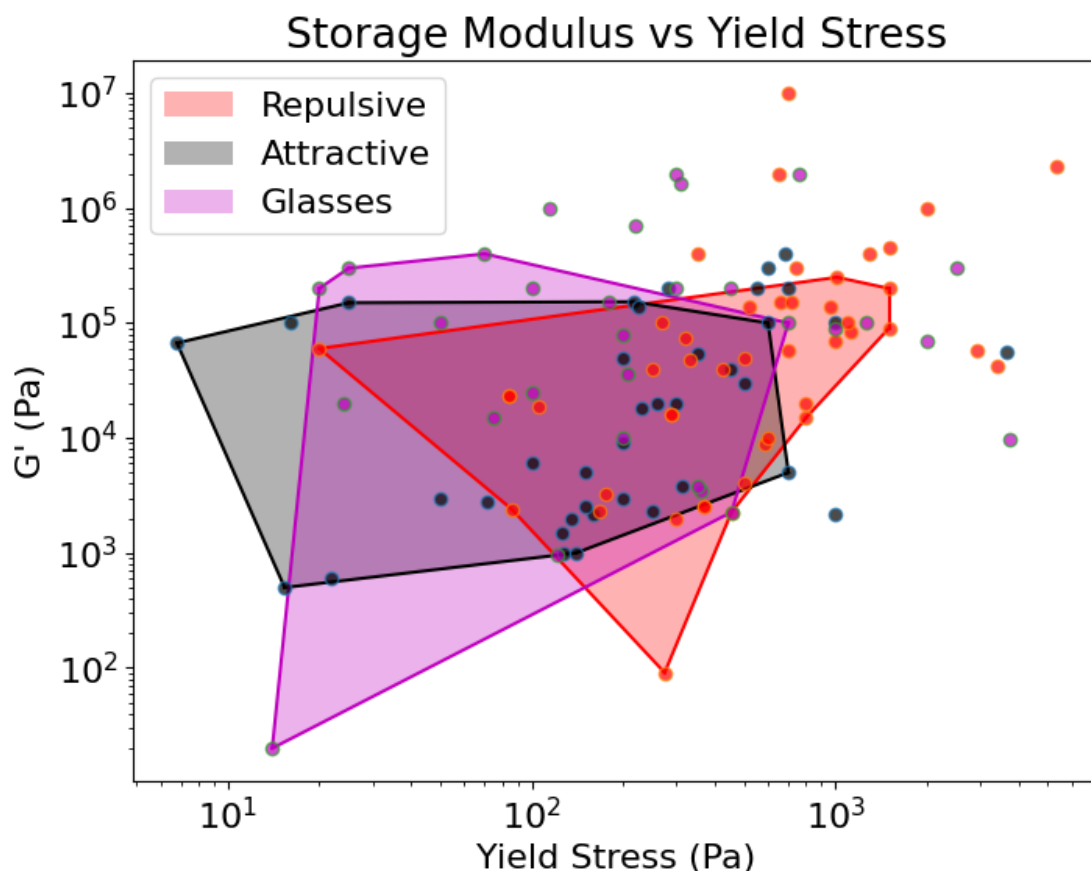
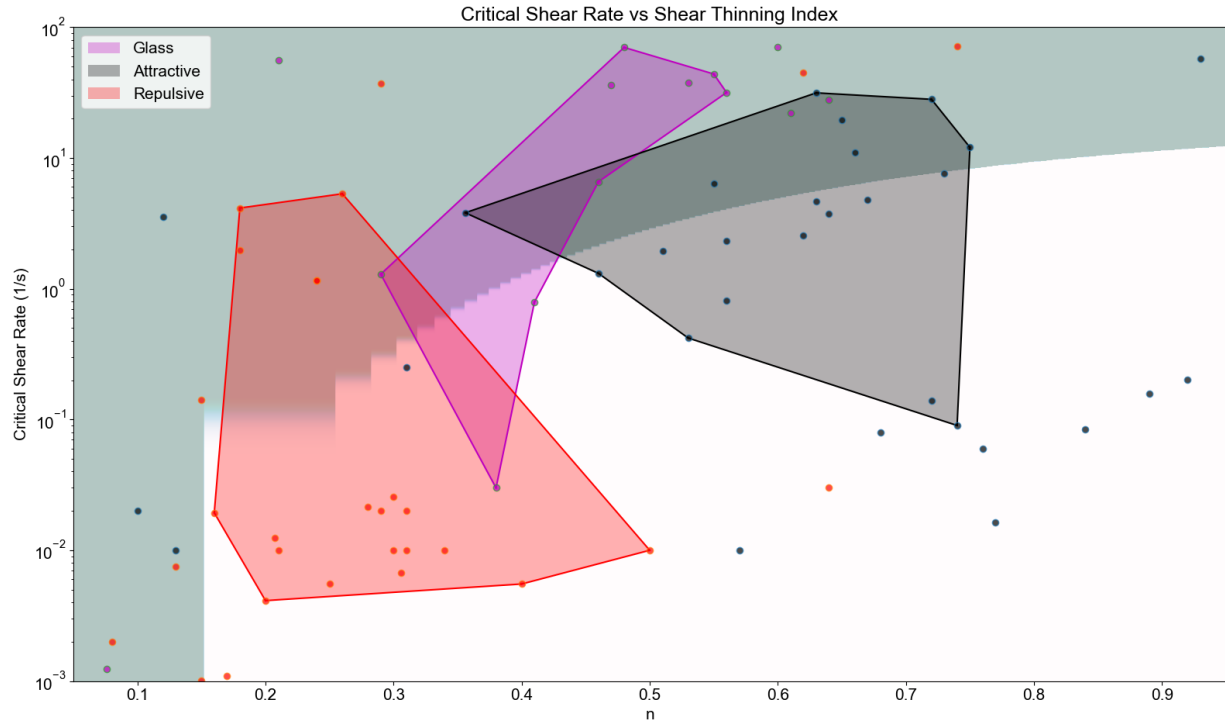


Figure 43:  $G'$  vs. static yield stress Ashby plot for initial material selection.

Nearly all existing printable inks, save some attractive dominated fluids (black shaded region), have a storage modulus orders of magnitude greater than 70 Pa. The upper bound of static yield stress still enables one to use repulsion dominated fluids. Ultimately, as will occasionally be the case, these initial constraints do not greatly help with ink selection – secondary rheological and design constraints will need to be employed.

To enable flow through a  $200\ \mu\text{m}$  nozzle, the ink should be highly shear thinning. Using the inequality presented in Equation 24, extrudable and printable regions of the critical shear rate and shear thinning index space can be noted (Figure 44).



*Figure 44: Region of the critical shear rate and shear thinning index space which enable extrudability, given a target print speed of 10 mm/s and 200  $\mu\text{m}$  diameter nozzle. Regions shaded in blue satisfy the inequality (Equation 24).*

From Figure 44, a significant portion of the attractive glass printable region falls within the inequality region. A smaller portion of the repulsion dominated fluids fall within the printable region, though most points are focused on lower critical shear rates. Attraction dominated inks are mostly ruled out. These inks are further incompatible with high temperature post processing regimens. From the Ashby-like plots, repulsion dominated fluids with shear thinning indices from 0.15-0.35 and high critical shear rates are compatible. Likewise, most attractive glass inks are compatible, with fewer restrictions.

Finally, the hierarchical porosity design and continuity design objectives place a subtle selection guideline. Within a unimodal microparticle ink, the interparticle porosity will tend to be greater. However, a bimodal ink will provide enhanced continuity through a reduction of the interparticle porosity and increased packing fraction. Likewise, this increase in packing fraction will reduce shrinkage and enhance dense ceramic substrate compatibility, which shrinks negligibly during post-processing.<sup>50</sup> Using the design constraints and Ashby-like plots, an

attractive glass consisting of a bimodal copper particle network would be a reasonable starting point. Moreover, with the need for extensibility, attractive glasses feature greater critical shear rates, and will resist internal breakdown to a greater extent. Ultimately, the tradeoff of interparticle porosity, extrudability, and application performance would still need to be assessed. Though this design process selects an attractive glass, a repulsion dominated fluid was synthesized. Synthesis details and experimental results are briefly described below.

#### 4.4.4 Experimental

Copper particles (10  $\mu\text{m}$ ) were purchased from Beantown Chemical and used as received to serve as the ink's particulate phase (X1). Ethyl cellulose (ethoxyl content 48%) was purchased from Acros Organics. Ethanol (Decon Labs, 200 proof) was used as a solvent. The resulting ethyl cellulose solution serves as the polymer matrix (X2). Toluene was purchased from Alfa Aesar and used as a humectant to retard ink drying in the nozzle tip (X3).

Ink synthesis started by mixing a homogenous 10% (w/v) solution of ethyl cellulose in ethanol to serve as the binder and matrix material. Copper particles were then placed in a beaker and wet by toluene. Next, ethyl cellulose solution was added. In all cases, the mass of the ink was 10.1 g prior to mixing. The solution was set to mix at room temperature with mechanical stirring for the various mixing times explored. The mixing speed was initially set at 350 rpm and adjusted as solution viscosity increased to allow continuous rotation of the stir bar. This method was used for all ink formulations explored in this study.

Printing of the inks was performed using a Nordson JR2300N robotic arm equipped with a Performus V pneumatic pressure dispensing system. Following mixing, the inks were loaded into Nordson 3cc syringe barrels and extruded through 200  $\mu\text{m}$  plastic tapered Nordson syringe tips in ambient conditions. To gauge printing fidelity during the parametric studies, inks were printed using a 5x5 mm<sup>2</sup> snake gird pattern with 750  $\mu\text{m}$  line spacing. The line widths were measured using an optical microscope (DinoLite). For fabrication, a copper scaffold was printed onto the ceramic LATP electrolyte (Figure 45). The sample was then flipped, and the other side patterned identically. Next, the samples were sintered to 550C for binder burnout.



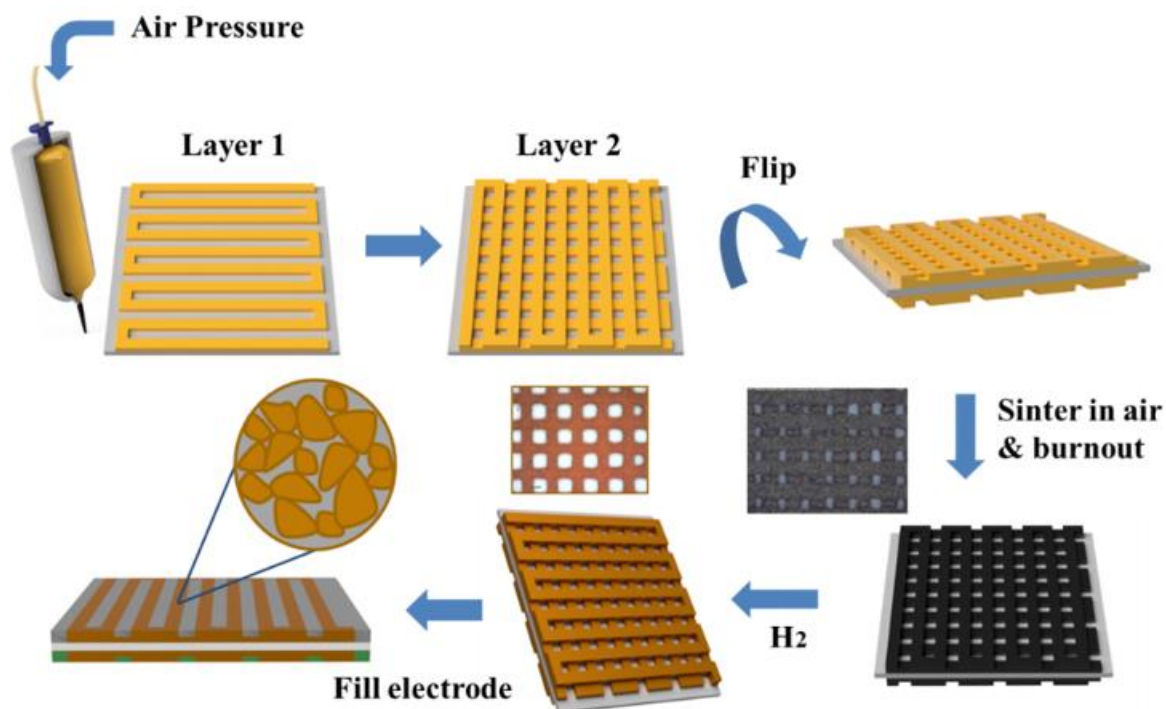


Figure 45: Processing schematic for the copper scaffolds. Inks are patterned on one side and then the other side of the LATP. Following sintering and binder burnout, the hierarchical pores are infiltrated with lithium metal.

Ink viscosity was first evaluated using a Brookfield DV-II+ Pro and a Rheometrics RMS-800 rotational rheometer at shear rates ranging from 0.1-100  $s^{-1}$  at 0.5% strain to obtain and evaluate the ink flow curves. When possible, ink rheology was further evaluated with the RMS-800 rheometer using dynamic strain sweeps from 0.1-100% strain at 10 rad/s with a 1.4 mm gap. The strain sweeps help to further characterize the internal ink structure, which could not be easily assessed from the shear-rate controlled flow curves. The linear viscoelastic region (LVR) is defined as the region in which the storage modulus ( $G'$ ) varies no more than 5%. From the LVR, one can also determine ink 'stiffness'. An adequate stiffness is necessary to assist filaments in retaining shape, supporting the weight of subsequent layers, and enabling spanning features. In our case, ink stiffness was taken as the average of the storage modulus in the LVR.

#### 4.4.5 Postscript

A jammed microparticle copper ink was ultimately employed. However, having down-selected the microstructure to a repulsion dominated or attractive glass ink would have reduced the binder weight percent range, as the binder would contribute to the attractive shear properties. Moreover, the jammed ink did provide substantial interparticle porosity, but greatly suffered from delamination. In fact, the delamination issues present in the jammed system nearly eliminated any '3D' structures, because the interfacial area between the scaffold and electrolyte was minimal. More complex 2D structures were printed instead. It is likely that an attractive glass would have provided greater design freedom. Moreover, an attractive glass, even with minimal binder volume fraction, could have mitigated the issues of brittleness and the tendency of the high-volume fraction suspension to break during deposition.

#### 4.5 Results

Regarding performance, the copper scaffold shown in Figure 46 delivered a relatively low stripping/plating overpotential of 60 mV at the same current density of 0.05 mA/cm<sup>2</sup>, which was 27 times smaller than that of the bare lithium metal anode. Moreover, the Coulombic efficiency of the 3D system was measured at current densities of 0.05 mA/cm<sup>2</sup>, 0.1 mA/cm<sup>2</sup>, and 0.2 mA/cm<sup>2</sup>, respectively. The average Coulombic efficiency of the 3D system was 99.90% at a current density of 0.05 mA/cm<sup>2</sup>, 99.93% at 0.1 mA/cm<sup>2</sup>, and 99.98% at 0.2 mA/cm<sup>2</sup>, respectively. Notably, all Coulombic efficiencies of the 3D system at different current densities during cycling were retained above 99%, which indicates a stable SEI film and a good (de)lithiation process. The printed pattern was maintained after all post-processing, as shown in the optical images of Figure 46a and Figure 46b. Surprisingly, it was found that nanowire structures of a 150 nm in width and 5 μm in length were formed on the surface of the copper particles. These numerous protuberant nanofibers on the 3D printed Cu scaffold functioned as the charge centers and nucleation sites. *Chi et al.* and *Yang et al.* demonstrate that Li preferentially nucleates and grows on the protuberant surfaces of the nanofiber structures and fills in the pores of the 3D structure.<sup>111,114</sup>

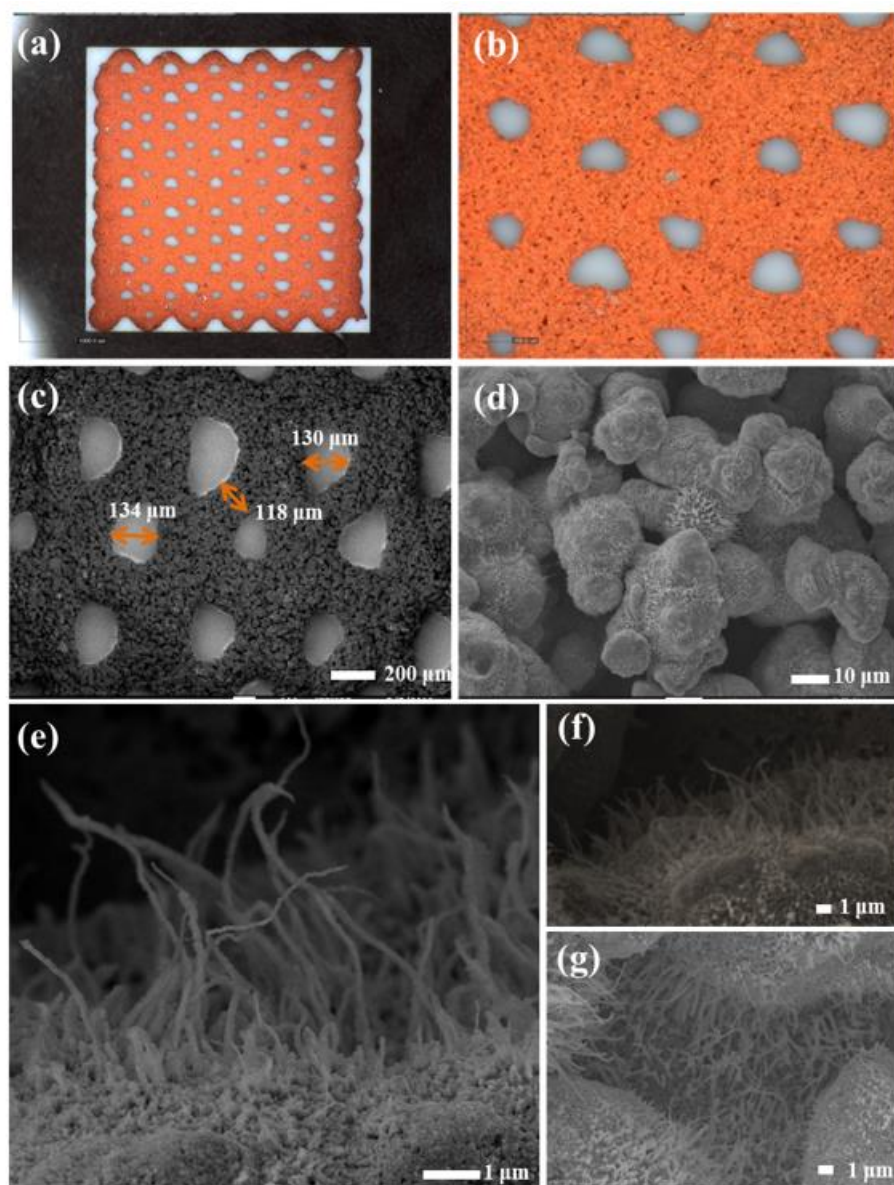


Figure 46: (a, b) Optical images of the single-layer grid after reduction in a hydrogen atmosphere. (c) Low-magnification SEM image showing the  $\sim 130 \mu\text{m}$  pore size and structure. (d) SEM images of the post-processed grid revealing the internal porosity from the binder burnout, and (e-g) SEM images of the CuO nanowires growing on the particles' surface.

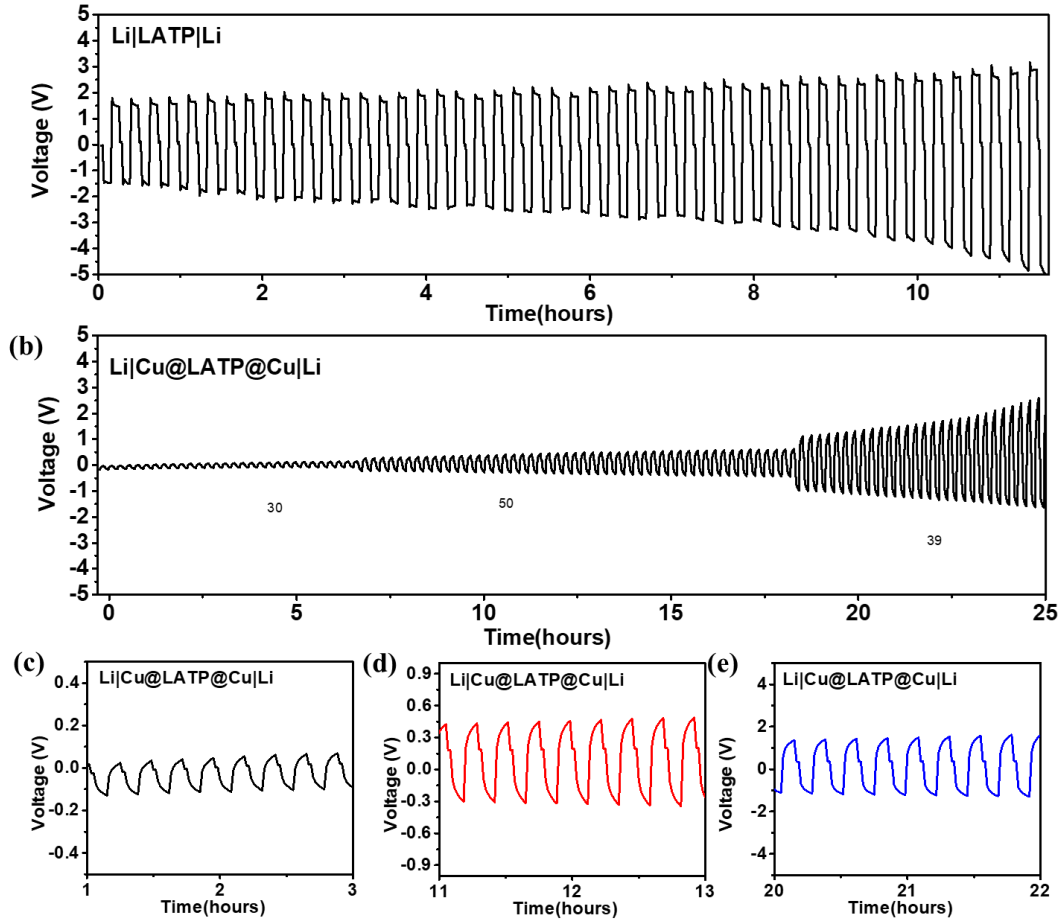


Figure 47: Voltage–time curves of (a) Li|LATP|Li symmetric cell at current density of 0.05 mA/cm<sup>2</sup>, (b) Li|Cu@LATP@Cu|Li symmetric cell at different current densities of 0.05 mA/cm<sup>2</sup>, 0.1 mA/cm<sup>2</sup>, 0.2 mA/cm<sup>2</sup>. Zoomed-in profiles at different current density of (c) 0.05 mA/cm<sup>2</sup>, (d) 0.1 mA/cm<sup>2</sup>, (e) 0.2 mA/cm<sup>2</sup>.

## 5 Attractive Glass Case Study

### 5.1 Problem Statement

Within industry, real-time structural health monitoring is critically important.<sup>115</sup> However, in high temperature environments (>600 °C), integration of sensing elements in-situ remains a challenge.<sup>116,117</sup> For example, in furnace refractory, the sensing element's substrate may be highly heterogenous and irregular, featuring multimodal aggregate distributions. The resulting protrusions pose a significant challenge to forming intimate sensor-substrate interfaces. Additionally, the substrate protrusions force any *in-situ* deposition technique to

adapt to the surface, introducing further manufacturing and operational challenges. Ideally, the sensing material and its respective substrate must both conform to the structural substrate, intimately bond, and shrink minimally to prevent stress induced failures. This problem requires a sensor material suite which can be extruded simultaneously. A core material will act as an insulator and protective shield, while the inner core material will serve as the electronic material. One technique, coaxial DIW, enables extrusion of two materials simultaneously.<sup>118</sup> As such, the challenge is to engineer two materials which can withstand high temperatures, shrink minimally during post-processing, maintain continuity, and electronically conduct.

## 5.2 The Model

For a reliable cross-section and predictable resistance, the core must minimally deform during deposition. The deformation will be both a function of the co-flow– and associated dimensionless numbers (Re, Ca, We) – as well as the gravitational forces from the shell after deposition. The ability of the core to resist deformation can be modeled using a modified version of M'Barki's proposed  $\mathcal{E}$  parameter (Equation 25):

$$\mathcal{E} = \frac{\tau_y^{dyn}}{(\rho g h + \gamma R^{-1})}$$

*Equation 25*

where  $\tau_y^{dyn}$  is the dynamic yield stress of the core,  $\rho$  is the density of the shell ink,  $g$  is the gravitational constant,  $h$  is the height of the shell acting on the core,  $\gamma$  is the surface tension of the shell ink, and  $R^{-1}$  is the radius of the shell. If  $\mathcal{E} > 1$ , the core can resist the inward pulls of capillary and gravitational forces.

To calculate  $\mathcal{E}$ , the surface tension of the yield stress fluid must be known. However, the surface tension of a yield stress fluid is challenging to calculate but can be reasonably approximated as that of the solvent medium.<sup>119</sup> To encourage substrate bonding, the solvent medium of the shell ink will be water. Surface tension can then be approximated as 72 mN/m. The coaxial nozzle has an exit radius 0.625 mm. Ideally, assuming a circular cross section, the maximum height of the shell above the core should 0.625 mm. However, the effects of die swell

may increase the cross section ~5-10%.<sup>120</sup> With that,  $h \approx 0.69 \text{ mm}$ . The density,  $\rho$ , and the dynamic yield stress  $\tau_y^{dyn}$  of the shell and core ink are the remaining variables for which to select through design.

Additionally, both fluids must be extrudable, and match the stage relative flow rates. Under extrusion will result in towing and discontinuities, while over extrusion will decrease fidelity and deform the core. From hardware constraints, the maximum extrusion pressure of the core and shell ink are approximately 345 kPa and 138 kPa, respectively. The target printing velocity for the coaxial system is 5 mm/s. Likewise, a 410  $\mu\text{m}$  nozzle is to be used for the core. Nozzle lengths are approximately 14 and 25 mm for the core and shell nozzles, respectively. Using these targets, we can again employ the critical shear rate inequality (Equation 24).

Finally, a significantly constraining factor is the need for high temperature compatibility and minimal shrinkage. The high temperature requirements stem from the need to monitor processes in industrial furnaces. The minimal shrinkage requirements –defined as < 2% shrinkage – stems from the refractory substrates. Refractory tends to contain multimodal aggregate distributions tailored to maximize packing and minimize shrinkage and dimensional changes. Therefore, if the printed sample does not match the shrinkage, catastrophic cracking and failure will result. This is an important constraint in that it immediately guides design towards a multimodal particle distribution. Multimodal distributions enable increased solids loading and enhance the packing fraction. These enhancements positively influence sintering, as the smaller particles are expected to fill in any intra-granular gaps between the larger grains, leading to improved densification. This effect on  $\Phi_m$  has been shown to be especially pronounced on particles with a size ratio of ~7:1, i.e. the coarse particles are approximately 7 times the size of the fine.<sup>50</sup>

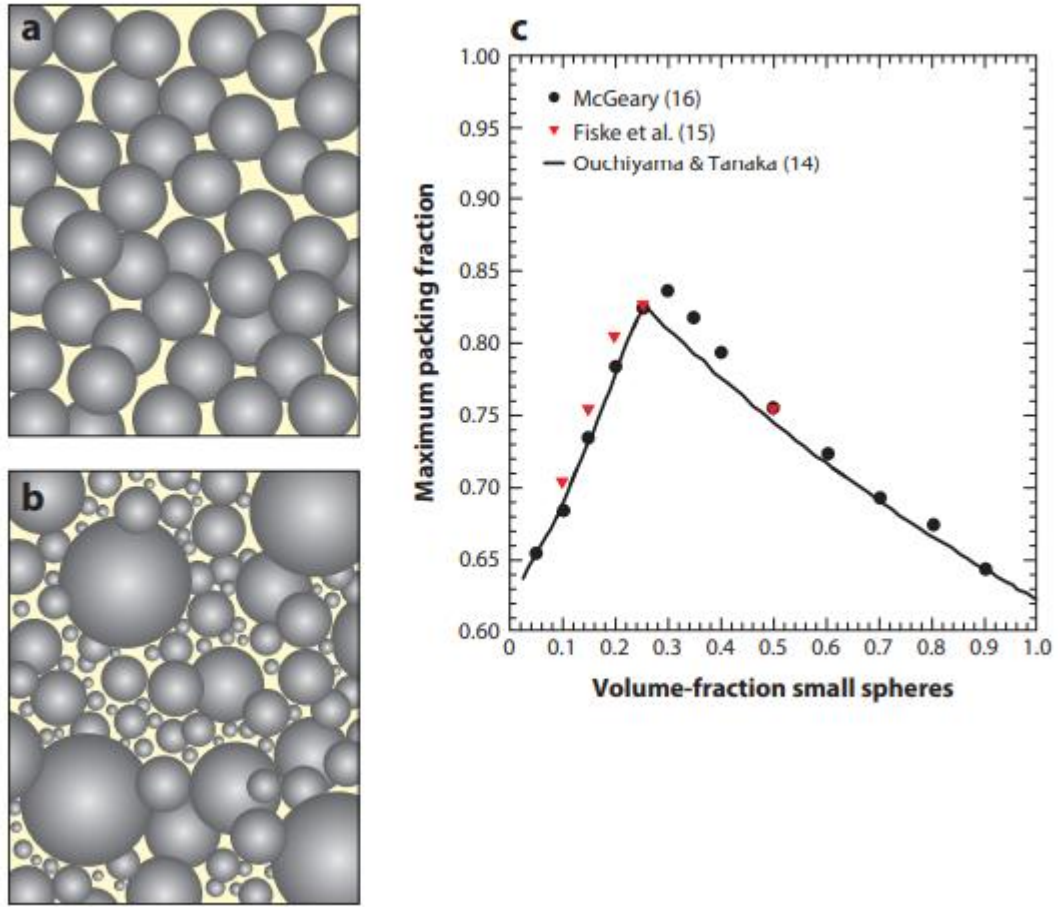


Figure 48: (a) Visual representation of packing in a unimodal distribution, b) visual representation of packing in a bimodal distribution, and (c) max packing fraction vs small sphere volume fraction for a bimodal particle formulation with  $\alpha_p = 20$ . Here, formulations with approximately 30 vol% maximize the packing fraction.<sup>121</sup>

Using the above models and clearly defined objectives, a design table is formulated (Table 14).



Table 14: Design table for coaxial ceramic conductors.

Function	<i>Conductive elements for high temperature electronics</i>
Objective	<i>Minimize discontinuities in conductors printed on rough/uneven substrates</i>
Constraints	<i>(a) Compatible with temp &gt; 1000°C</i> <i>(b) Shrinkage &lt; 2%</i> <i>(c) Core: <math>E &gt; 1</math></i> <i>(d) Extrudable at 5 mm/s stage velocity</i>

### 5.3 Selection

First, one can apply the extrudability inequality for both the core and shell systems (Figure 49).

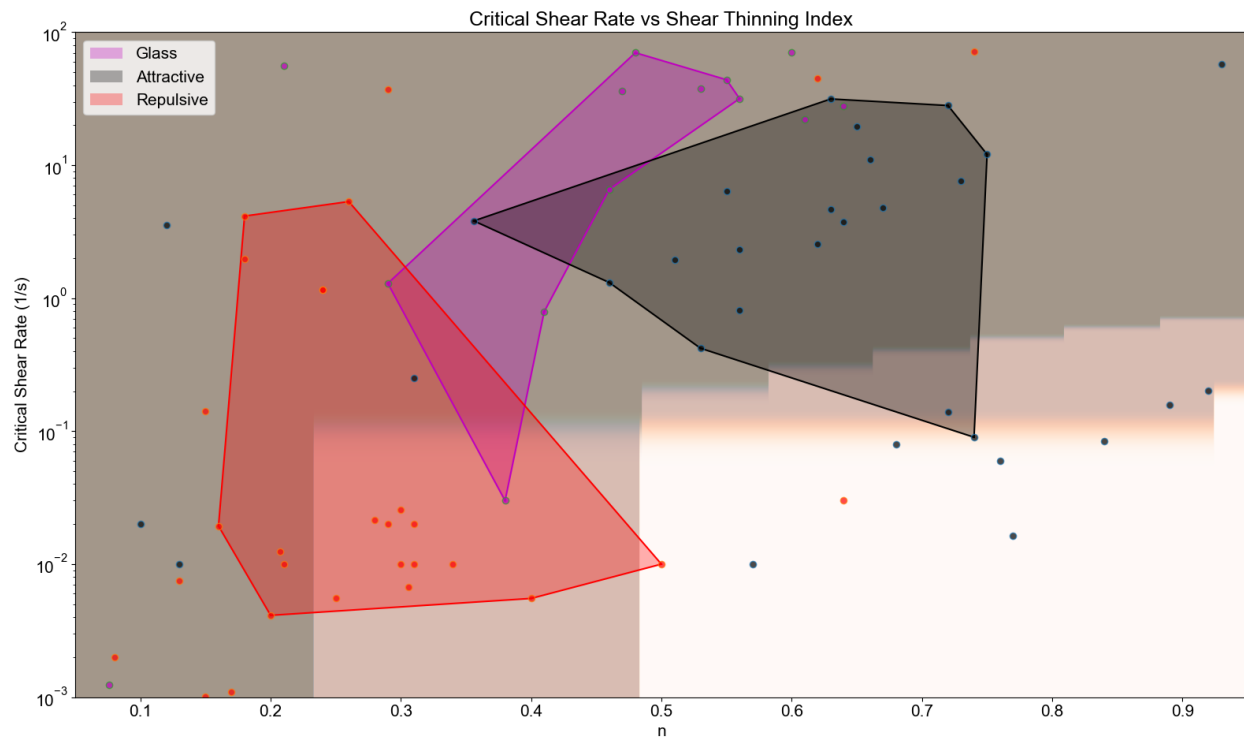


Figure 49: Extrudability inequality applied to the shell (darker region) and core (lighter region) systems.

From Figure 49, compatible shell fluids fall mostly in the attractive glass and attraction dominated regions. However, the need for high temperature compatibility pushes one towards



ceramics fillers, as most polymers will degrade quickly at furnace temperatures. Likewise, even if the polymer does not degrade, the shrinkage would likely be greater than allowable.

Therefore, purely attractive polymeric networks are eliminated as core or shell ink candidates. On the other hand, both repulsion dominated systems and attractive glass systems will likely be extrudable as the core system. The core ink needs to form a continuous conductive network following sintering, but does not require a threshold storage modulus, because it will be supported by the shell ink. As is typically the case with DIW, we have limited numerical constraints, so design space is open. What have we deduced so far?

For the shell, shrinkage and post-processing are the primary concern. Therefore, a bimodally distributed ceramic ink is likely needed. To minimize shrinkage, approximately 70 vol% will be microparticles, and 30 vol% nanoparticles. Likewise, polymeric binder should further be minimized to reduce shrinkage. This combination will likely place us in the attractive glass region, as the yield stress will be a function of the jammed microparticles and attractive interactions of the nanoparticles. We can then consult the Ashby-like co-plots and target static yield stresses from  $10^2 - 10^3 \text{ Pa}$ , a storage modulus ranging from  $10^4 - 10^6 \text{ Pa}$ , a shear thinning index ranging from 0.3 – 0.4, and a critical shear rate ranging from  $10^0 - 10^3 \text{ 1/s}$ .

Again, for the core, we have significant flexibility. In practice, one of the simplest methods to quickly formulate an ink is to add microparticles to a viscous binder solution. Depending on the attractive degree of the binder, these formulations will typically place one in the attraction dominated yield stress fluid region. Using the Ashby-like plots and extrudability inequality, we can target static yield stresses from  $10^1 - 10^3 \text{ Pa}$ , a storage modulus ranging from  $10^3 - 10^4 \text{ Pa}$ , a shear thinning index ranging from 0.5 – 0.9, and a critical shear rate ranging from  $10^{-2} - 10^1 \text{ 1/s}$ .

#### 5.4 Experimental

Fine alumina (A 16 SG) and coarse alumina (A 20 SG) particles were purchased from Almatix (Leetsdale, PA USA) and used as received to serve as the ink's particulate phase. The fine alumina contains a median particle size of  $0.5 \text{ }\mu\text{m}$  (Cilas d90  $2.9 \text{ }\mu\text{m}$  and Cilas d50  $0.5 \text{ }\mu\text{m}$ ). However, the coarse alumina features a median particle size of  $\sim 3 \text{ }\mu\text{m}$  (Cilas d90  $7.8 \text{ }\mu\text{m}$  and

Cilas d50 3.3  $\mu\text{m}$ ). Methylcellulose (Methoxyl content 28-32%) was purchased from Sigma Aldrich (St. Louis, MO USA) and deionized water was used as a solvent. Polyacrylic acid powder (avg. MW 1800) was purchased from Sigma Aldrich (St. Louis, MO USA) and used as a surfactant and pH modifier. To further adjust the ink pH and tailor the particle surface charge and ink stiffness, sodium hydroxide (1 N, Sigma Aldrich, St. Louis, MO USA) was used for titration. Finally, indium tin oxide particles (325 mesh,  $\text{In}_2\text{O}_3$  90%,  $\text{SnO}_2$  10%) were purchased from Sigma Aldrich (St. Louis, MO USA) and used as received. A Johnson Matthey (London, UK) ink vehicle (Johnson Matthey 63-2 organic ink vehicle), consisting of ethyl cellulose and terpeneol, was used as the core ink binder solution and used without modification. This terpeneol based binder system lends the core ink hydrophobic properties, ensuring the core-shell ink system is immiscible.

Rheology was characterized using an RMS-800 Rheometer (Rheometric Scientific, Piscataway, NJ USA) with a 1 mm gap and 25 mm parallel plate. Sandpaper was attached to both plates to prevent slip. Strain sweeps, used to characterize the shear moduli and stiffness, were performed at 10 rad/s from 0.02 – 50% strain. Steady state measurements, used to characterize the viscosity and dynamic yield stress, were performed from 0.01 – 50 1/s. The dynamic yield stress critically provides insight into how much stress the filament or feature can endure after printing without causing deformation.

Core and shell dimensional measurements were obtained using a digital microscope (Dino-Lite Edge, Los Angeles, CA USA). Cross-sectional areas were characterized through built-in Dino-Lite automatic edge tracing tools. Cross-sectional scanning electron microscopy (SEM) and energy dispersive X-ray spectroscopy (EDX) was performed using a Hitachi S-4700 electron microscope after briefly sputtering the samples with platinum. Finally, when feasible, surface tension was measured with the pendant drop method using the ImageJ (National Institute of Health) Drop Analysis Plugin.

#### 5.4.1 Ink Synthesis

Alumina core ink preparation began with the synthesis of a 2.5 wt% aqueous methylcellulose binder solution. A 40 wt% aqueous polyacrylic acid solution was then mixed and added to the binder solution. Coarse and fine alumina were added in a 3:1 volume ratio to

bring the alumina volume fraction to approximately 52%. Upon addition of half of the alumina, the ink was mixed in a planetary mixer (Thinky AR200, Thinky USA) for 2 minutes, followed by wand sonication (Model 50 Sonic Dismembrator, Fischer Scientific) for 20 seconds. The remainder of the alumina was then added, and the planetary mixer and sonication procedure repeated. Finally, the ink pH was measured using a digital benchtop pH meter (Orion Star A211, Thermo Scientific). The pH was adjusted as necessary using a 1 N NaOH hydroxide solution (Sigma Aldrich, St. Louis, MO USA). The final ink consisted of approximately 52 vol% alumina, 4 vol% PAA stabilizer solution, and 34 vol% methylcellulose solution. By constituent, the final alumina shell ink consisted of approximately 52 vol% alumina, 0.75 vol% PAA, 0.85 vol% methylcellulose, and 46.4 vol% water.

Two conductive core ITO inks were prepared by mixing the required ITO volume into a Johnson Matthey Ink vehicle. ITO inks were prepared such that the solids volume fraction represented 15 vol% and 20 vol%, respectively. In each case, the powder was added to the ink vehicle, mixed within the planetary mixer and wand sonicated for 20 seconds. All inks (core and shell) were then briefly degassed in the planetary mixer and loaded into printing syringes (Nordson EFD, Providence, RI USA) for deposition.

## 5.5 Results

To demonstrate the potential functionality of the core-shell system in maintaining continuity across a heterogeneous substrate, coaxial alumina-ITO lines were printed onto a ceramic surface with visible roughness. Within the substrate are multimodal distributions of aggregate, which vary by several millimeters and perturb the surface (Figure 50b). Within the ink-substrate system, both the alumina shell and refractory material are aqueous based. Therefore, the alumina shell forms an intimate interface with the substrate, mitigating the 'foreign body' issue typically associated with embedded sensing elements. Additionally, the minimal binder content and large storage modulus help to limit spreading and promote fidelity retention, highlighted by the hemispherical coaxial cross-section. The dashed red line in Figure 50b details the ability of the shell to conform to the substrate, while shielding the ITO core (green circle).

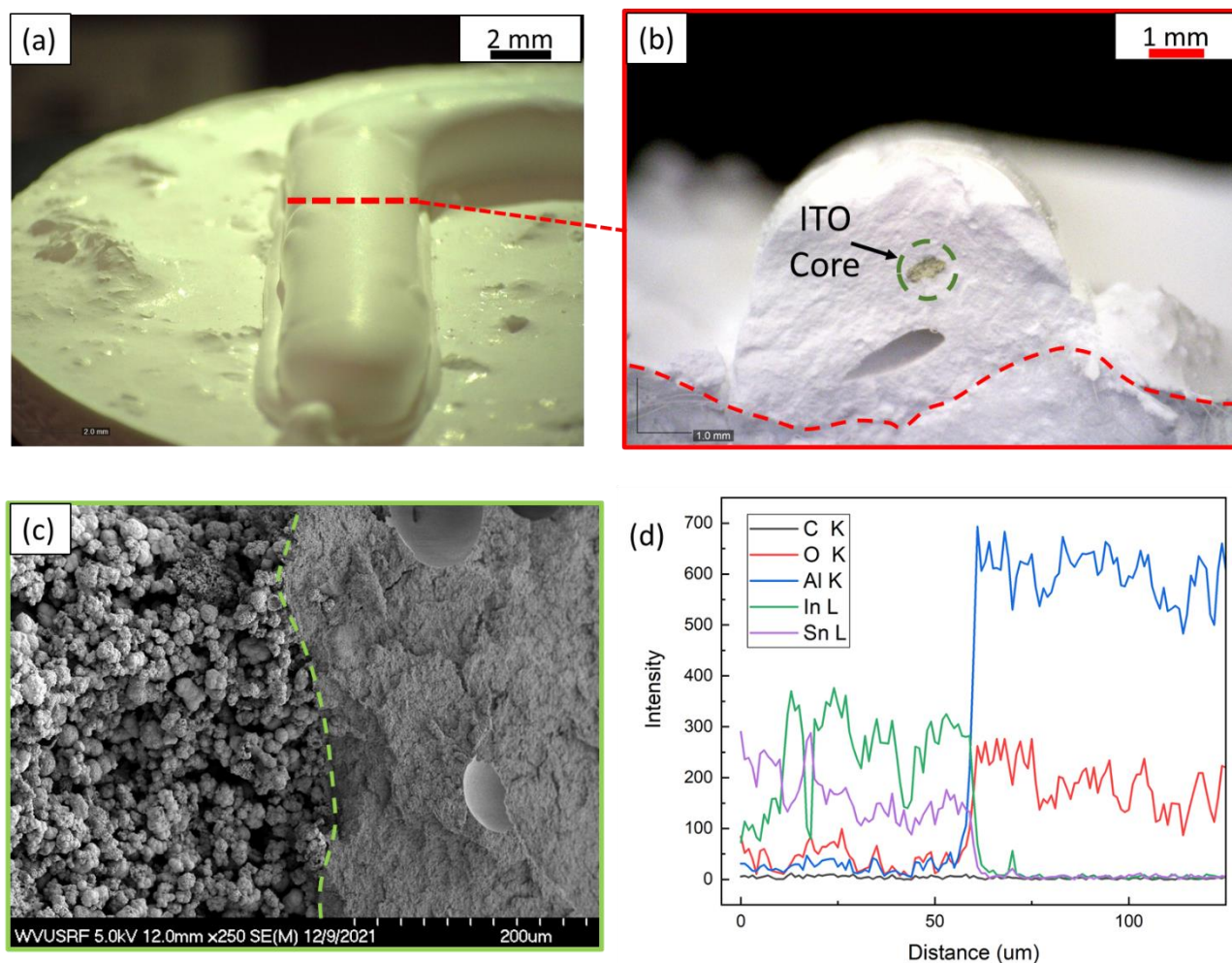
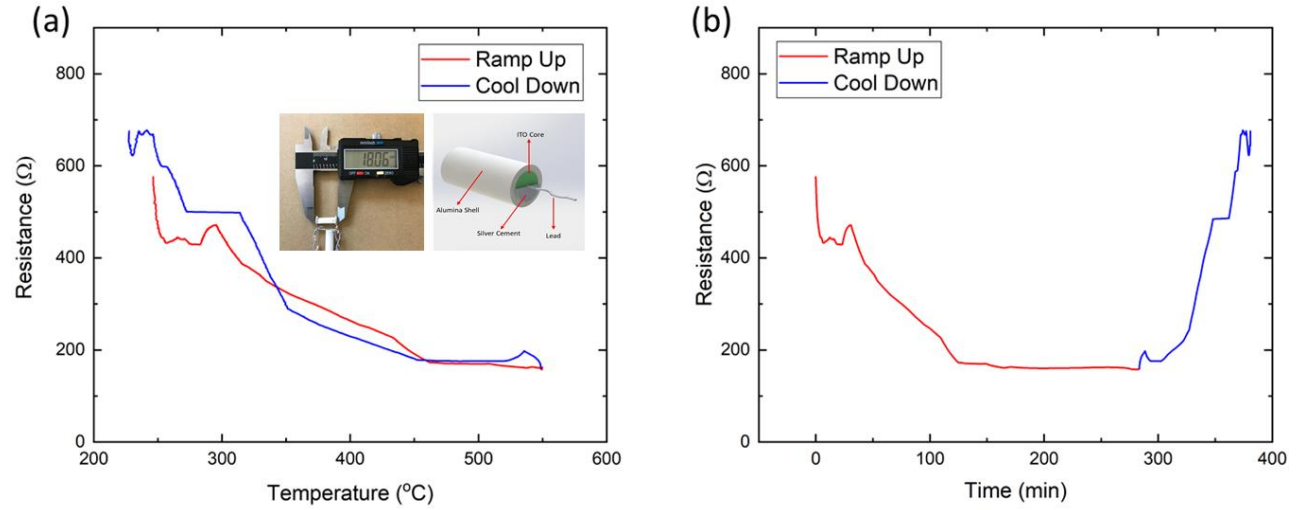


Figure 50: (a) A coaxial thermistor printed directly onto a wet and heterogenous refractory substrate. (b) Optical cross-sectional image demonstrating shell conformability to the substrate surface. (c) Cross-sectional SEM image of the core (left) and shell (right) interface of a sintered sample. (d) Results of an EDS line scan detailing a sharp transition in composition at the interface.

Finally, to demonstrate system functionality, a coaxial Alumina-ITO sample was printed and cycled to 600 °C to assess the system's ability to detect changes in temperature. For analysis of stability, the furnace temperature was held at 600 °C for two-hours, following a  $2 \frac{\text{deg}}{\text{min}}$  ramp up. Despite the moderate hysteresis observed in Figure 51a, system functionality is reflected by the maintained continuity and relative stability during the temperature hold (Figure 51). While there is room for improvement, this data shows promise in utilizing coaxial

ceramic DIW to address the manufacturing challenges facing the *in-situ* deposition of high temperature materials or structural health monitoring systems.



*Figure 51: Resistance measurements as a function of time and temperature during a ramp and two-hour hold at 600°C. (a) Resistance versus temperature, revealing moderate system hysteresis and instability in the ramp phases. Left inset: Optical image of the measured coaxially printed sample length (18 mm). Right inset: Schematic of the coaxial sample, silver braze, and lead connection. (b) Resistance versus time for the coaxial ceramic system, detailing stability during the two-hour hold. Instability during the ramps is attributed to mobility of the contacts, and not a reflection of ITO instabilities.*

## 5.6 Postscript

As discussed, to address sintering and drying shrinkage, a bimodal alumina shell ink was synthesized. When fine particles are added to coarse the maximum packing fraction ( $\Phi_m$ ) increases. This effect on  $\Phi_m$  has been shown to be especially pronounced on particles with a size ratio of  $\sim 7:1$ , i.e., the coarse particles are approximately 7 times the size of the fine.<sup>50</sup> Additionally, minimal amounts of binder vol% are critical for two reasons: 1) to minimize shrinkage from binder burnout and 2) maintain the ink in the attractive glass region. Considering the nanoparticles, one can engineer the rheological properties through colloidal interaction and target regions of printable attractive glasses. The alumina shell ink was prepared with the addition of polyacrylic acid (PAA), which provides steric repulsion, initially placing the ink the repulsion dominated regime. The polyacrylic acid adsorbs to the alumina particle surface electrostatically or through hydrogen bonding of (-COOH) if pH is monitored to

maintain alumina surface hydroxyl (-OH) groups. The steric repulsion provided by the adsorbed polymer is sufficient to prevent agglomeration of the microparticles. Further particle dispersion is induced through hand sonication following the planetary mixing stages. At this point, the ink may be considered repulsion dominated.

However, some degree of flocculation is needed for DIW, particularly in ink systems with relatively low organic binder content. Inducing flocculation, and increasing particle interaction, increases the viscosity which is typically provided through viscous polymers. Likewise, this flocculation transitions the fluid from repulsion dominated (sterically or electrostatically repulsed) to an attractive glass. Here, the attraction is enabled through charge screening. Through titration with NaOH following ink mixing, the alumina ink storage modulus could be tailored by approximately one order of magnitude (Figure 52a). Figure 52a reveals that as the pH increases from 7.5 to 7.9, ink stiffness increases. However, upon passing the point of zero charge, ink stiffness again decreases as particles regain electrostatic or steric repulsion.

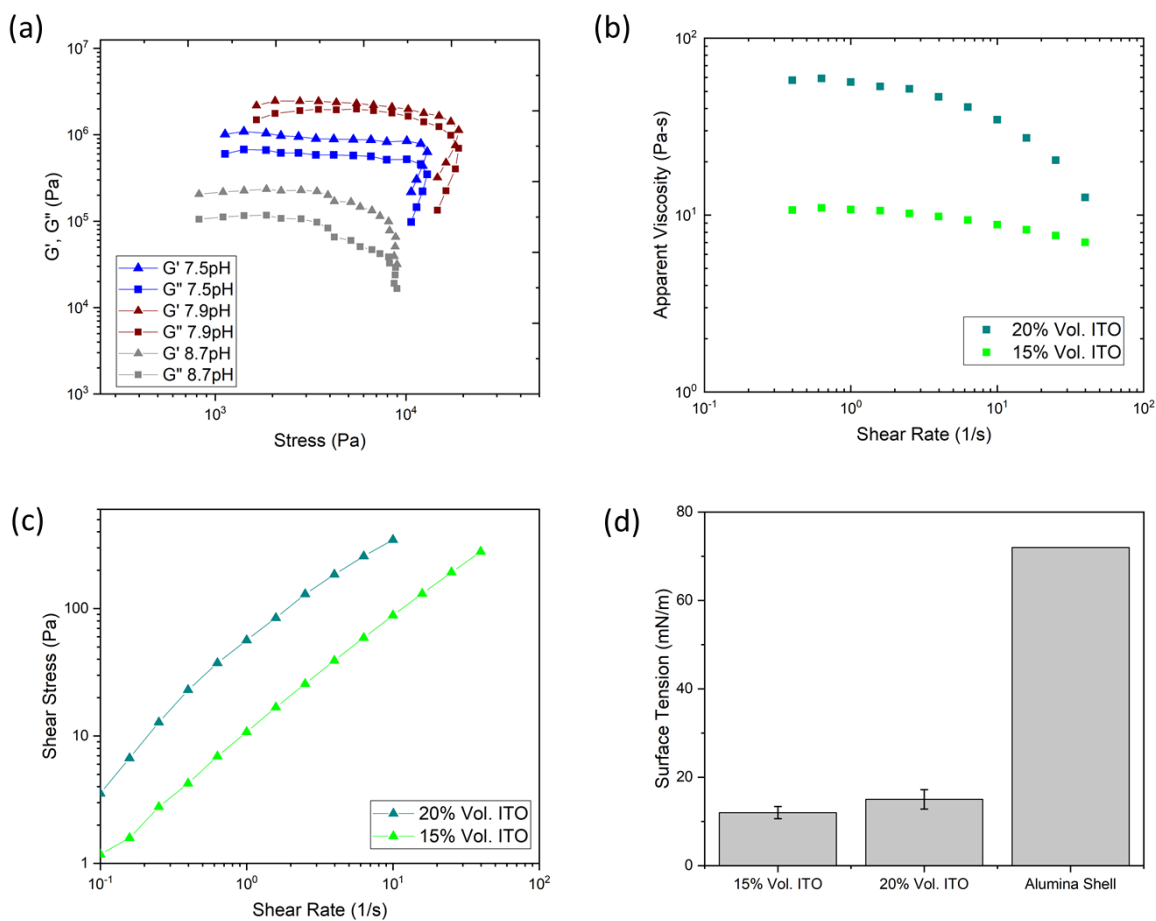


Figure 52: Core-shell ink rheological data and surface characterizations. (a) Storage and loss moduli vs. shear stress of the alumina shell inks, (b) apparent viscosity vs. shear rate, (c) shear stress vs. shear rate of the ITO core inks and (d) pendant drop measured surface tension.

Considering the initial design constraints and targets provided by the Ashby-like plots, how do we compare? Table 15 details the constraints, initial target properties, and potential candidate properties.

*Table 15: Target and achieved rheological parameters for the core and shell coaxial inks.*

	Target				Available			
Ink	$G'$	$\tau_y^{static}$	$\dot{\gamma}_{crit}$	$n$	$G'$	$\tau_y^{static}$	$\dot{\gamma}_{crit}$	$n$
15 vol% ITO	N/A	$10^1$ – $10^3$	$10^{-2}$ – $10^1$	0.5 – 0.9	N/A	1.25 0.25 (dyn)	0.05	0.83
20 vol% ITO	N/A	$10^1$ – $10^3$	$10^{-2}$ – $10^1$	0.5 – 0.9	30	7.16 5.0 (dyn)	0.06	0.76
7.5 pH Al <sub>2</sub> O <sub>3</sub>	$10^4$ – $10^6$	$10^2$ – $10^3$	$10^1$ – $10^3$	0.2 – 0.4	$10^6$	740	N/A	N/A
7.9 pH Al <sub>2</sub> O <sub>3</sub>	$10^4$ – $10^6$	$10^2$ – $10^3$	$10^1$ – $10^3$	0.2 – 0.4	$2 \cdot 10^6$	755	0.79	0.41
8.7 pH Al <sub>2</sub> O <sub>3</sub>	$10^4$ – $10^6$	$10^2$ – $10^3$	$10^1$ – $10^3$	0.2 – 0.4	$2 \cdot 10^5$	250	N/A	N/A

Since we are targeting an attractive glass, the 7.9 pH alumina formulation provides acceptable rheological parameters. Specifically, the yield stress of 755 Pa falls within the range of  $10^2$  –  $10^3$  Pa. Additionally, the shear-thinning index and critical shear rate place this formulation firmly in the attractive glass region and within the boundary proposed using Equation 24. For the core fluids, both fall in the target range for the shear thinning index ranging  $n = [0.5 - 0.9]$ . Furthermore, both fluids possess target critical shear rates in the range of  $10^{-2}$  –  $10^1$  1/s. The differentiating factor was the dynamic yield stress which is critical to resist deformation post-printing. In this case, the 20 vol% formulation was optimal and contributed to the annularity of the cores. For future work, the core could be made an attractive glass as well. In this case, shrinkage would be further minimized. However, challenge would be developing a non-aqueous based attractive glass.



## 6 Contributions and Future Work

### 6.1 Conclusions and Contributions

This thesis addresses several challenges facing direct ink writing. As stated in Chapter 2, DIW will progress beyond a rapid prototyping technology through 1) the rapid development and implementation of novel ink chemistries and 2) via a holistic coupling of the DIW process-property relationships. In literature, the rapid development of novel chemistries remains a time-consuming effort. This is due, in part, to the analysis-based approach, in which design targets are an afterthought. As such, the ink microstructure is rarely considered, and the microstructure relevant rheological properties are not noted. In essence, the ‘optimal’ rheological properties remain highly local to that ink system. Additionally, analysis-based approaches encourage many synthesis experiments and many rounds of characterization. Conversely, design begins by determining the rheological properties of an optimal ink and works backwards to identify compatible ink microstructures. The essence current DIW ink engineering is that authors routinely describe printability for local systems. If they characterize the microstructure, they will see how their printability metrics conform from, differ from, or fit into the current global understanding.

The Ashby-like plots, new extrudability constraints (Equation 24), and DIW database provide a route forward for design-based ink engineering. Before this thesis, the major element prohibiting design was the existence of a DIW database. The availability of the data and of the Ashby-like plots provides regions of the yield stress fluid parameter space compatible with three-dimensional DIW. As this design-based work progresses, we will look to integrate the database with existing materials data infrastructure, such as that of the Materials Genome Initiative. Likewise, by providing additional extrudability models, we further enable material down selection – a key element of the design process. We ultimately argue the DIW community has analyzed enough, and it is time to begin the transition to a design-based approach. In essence, it is time for the field to mature. Through the collection and synthesis of available DIW rheological data, Ashby-like plots can be generated, iterated upon, and used to provide target rheological metrics for a given ink microstructure.

Ultimately, we demonstrate the utility of the design-based approach in identifying a target ink microstructure and the target rheological parameters. Implementation of the Ashby-like plots and rheological database provide rapid parameter identification. Likewise, the design-outline encourages precise guidelines, and further clarifies desirable rheological properties. Instead of defaulting to the overly general “shear-thinning yield stress fluid” constraint, we can place hard constraints on the dynamic yield stress, static yield stress, shear-thinning index, and critical shear rate. From there, we can identify the yield stress fluid microstructure compatible with those constraints, and the overarching application goals.

## 6.2 Future Work

Expanding the database is a key priority. The database should ultimately be made available to all and serve as a repository for future DIW related work. Further refining the ink labels (repulsion dominated, attractive glass, etc.) will contribute to higher confidence in defining local printability. Future researchers may also reformat the yield stress fluid classification criteria by introducing new constraints. This re-classification will greatly change the convex hulls and Ashy-like plots. For example, the particle shape and surface roughness may be introduced as variables. Likewise, one may change the volume fraction constraints for the attraction dominated to repulsion dominated transition. Additionally, two important rheological metrics are absent from the database - the recovery index and recovery time. These values measure the change in storage modulus following process related shear. The work in this thesis essentially presumes that for printable inks the LVR storage modulus is maintained following extrusion. This is a reasonable presumption; however, it has not been explored in depth for the various yield stress fluid microstructures. Future work should normalize characterization of the recovery index and recovery time, enabling addition to the database.

Additionally, the changes within individual ink systems need to be mapped. For example, *Nelson et al.* note that repulsion dominated fluids tend to have smaller changes in the shear thinning index, while the yield stress changes significantly.<sup>57</sup> These changes and general flow behaviors can lend further insight into the shear response and further distinguish the yield stress fluid classes.

Finally, improving the resolution of the Ashby-like plots is paramount. There exist numerous sub-groups within the broad classes of attraction and repulsion dominated inks. Emulsions, foams, sterically repulsed hard spheres, and certain polymers constitute repulsive fluids. On the other hand, soft colloidal spheres, electrorheological, and magnetorheological fluids comprise attractive fluids. A framework for higher fidelity Ashby-like plots is shown in Chapter 3, but future efforts can focus on further refining the printability space within the parent classes. For example, the fluid class labels could broadly expand to “strongly attractive”, “weakly attractive”, “weakly repulsive”, and “strongly repulsive”. In promising work, *Fuhrmann et al.* distinguish “weak attractive glass”, “gelled glass” and “attractive glass” through characterization of the low amplitude oscillatory strain and loss modulus behavior.<sup>122</sup> Widely accepting these DIW characterization and adding the refined labels to the database will further enable engineering design decisions.

Furthermore, deeply understanding the process-property relationships is a key element of material down selection and ink design. Hardware constraints, nozzle selection, and substrate surface properties significantly impact the ink’s viability (Figure 53). Clearly defining these relationships remains a significant challenge. For example, even if one utilizes a design-based approach to accelerate ink development, identifying the optimal first-order processing variables is time consuming.

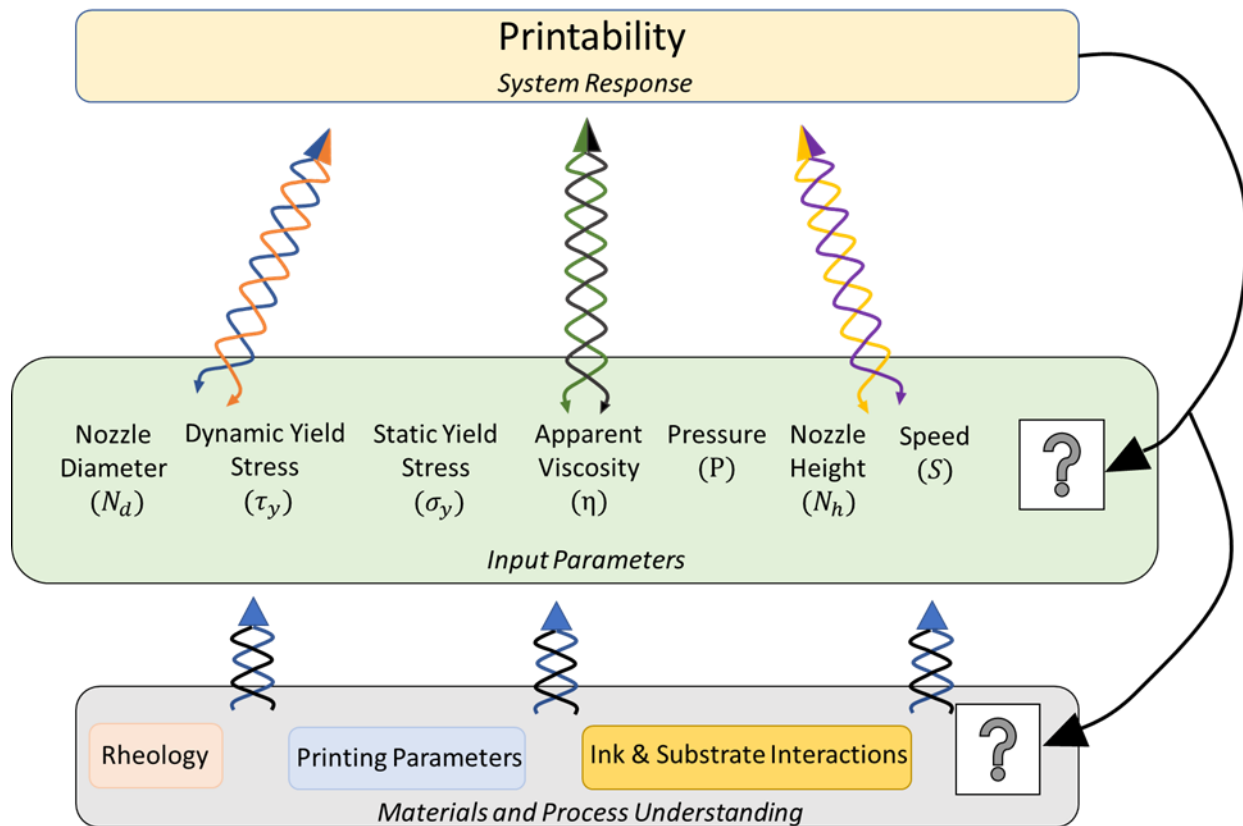


Figure 53: Coupling materials and process properties to further define printability.

An interesting approach to quickly identify process parameters involves machine learning. Using the database and associated labels, classification tasks using support vector machines or logistic regression could enable rapid printability assessments. Moreover, for some time, we explored the ability of a scalable Gaussian-process to synthesize process and material variables and predict the final printed feature dimensions (Figure 54). Theoretically, if achieved, one could implement a controller to target and change the first-order process variables for a given formulation and desired feature diameter. We further aimed to do this globally. For instance, silicones, copper inks, low-viscosity alumina suspensions, and silver inks were all printed at various conditions and their printed dimensions characterized. However, mixed success was achieved. For singular compositions, the accuracy was quite high. For example, predictions of one-part moisture cure silicones were highly accurate, with a root-mean squared error (RMSE) of less than 50 microns. Similarly, *Deneault et al.* had success implementing a

gaussian process to identify optimal print parameters, aiming to minimize the initial contact spreading in dilute ceramic compositions.<sup>123</sup>

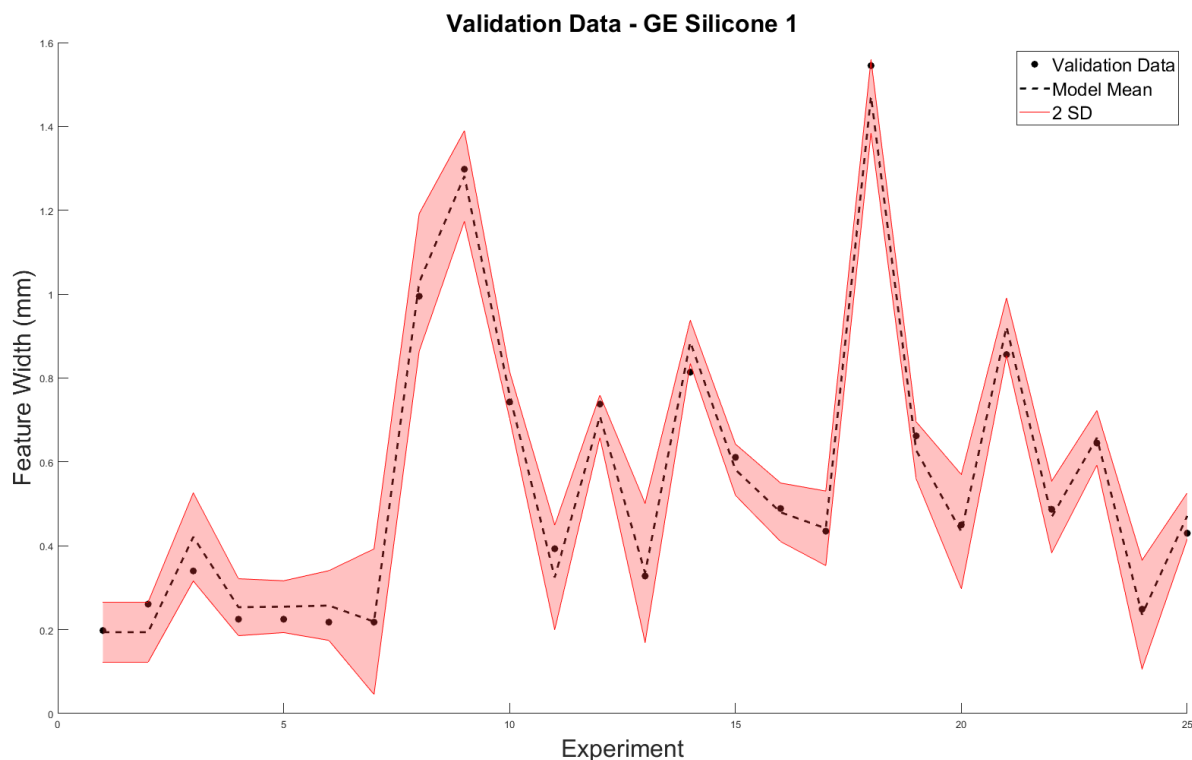


Figure 54: Gaussian Process Regression predicting the diameter of a GE Silicone 1 filament. Input variables include first order processing variables.

However, in our attempts, a global model was not achieved. This is likely a combination of relatively small sample size ( $n \approx 250$ ), as well as unidentified process variables. Within the scalable Gaussian process, a generalized additive model is used to produce a function which includes one-way and two-way variable interactions. It was our hypothesis that these two-way interactions would generate novel printability metrics. For example, *Menon et al.* utilized Lasso regression and two-way variable interactions to generate a ‘printability’ function for an attraction dominated ink.<sup>124</sup> Here, the printability was defined as an output within a small margin of error of the target. The caveat again, is that this printability function describes one material and one process. Though they produced a novel function and variable interactions, no globally transferrable metrics were borne. This thesis defines printability locally, and within

those local clusters identifies rheological ranges which enable rapid and successful material implementation. Therefore, future work can take a step back and utilize the scalable Gaussian Process within the local clusters – attraction dominated, repulsion dominated, and attractive glasses. Novel printability metrics – i.e., impactful variable interactions – may result and be unique to each class. This may then facilitate intrinsic, surface, or rheological characterizations for each ink classification and guide experimentation.

This leads to a final area of future work – identifying novel printability metrics. These metrics may include useful dimensionless quantities, like  $\Xi$ , which physically relate the ink's rheology and processing conditions.<sup>73</sup> Moreover, these dimensionless quantities provide a lower-level representation of the rheological parameter space and may be more visually compatible. As such, further Ashby-like plots could be presented, representing printable and non-printable regions for ink microstructures using metrics such as the Flow Transition Index (FTI).

## 7 References

1. Kodama, H. Automatic method for fabricating a three-dimensional plastic model with photo-hardening polymer. *Review of Scientific Instruments* **52**, 1770–1773 (1981).
2. American Society of Mechanical Engineers. *Stereolithography The First 3D Printing Technology*. (2016).
3. Candi, M. & Beltagui, A. Effective use of 3D printing in the innovation process. *Technovation* **80–81**, 63–73 (2019).
4. Deckard, C. R. Apparatus for producing parts by selective sintering. (1986).
5. Crump, S. Modeling apparatus for three-dimensional objects. (1989).
6. Cesarano, J. & Grieco, S. Robocasting: A New Technique for the Freeform Fabrication of Near-Net-Shape Ceramics. *Materials Technology* **12**, 98–100 (1997).
7. Cordonier, G. J. & Sierros, K. A. Unconventional Application of Direct Ink Writing: Surface Force-Driven Patterning of Low Viscosity Inks. *ACS Appl Mater Interfaces* **12**, 15875–15884 (2020).
8. Torres Arango, M. A. *et al.* Robotic Deposition of TiO<sub>2</sub> Films on Flexible Substrates from Hybrid Inks: Investigation of Synthesis–Processing–Microstructure–Photocatalytic Relationships. *ACS Appl Mater Interfaces* **8**, 24659–24670 (2016).
9. Kolesky, D. B., Homan, K. A., Skylar-Scott, M. A. & Lewis, J. A. Three-dimensional bioprinting of thick vascularized tissues. *Proc Natl Acad Sci U S A* **113**, 3179–84 (2016).

10. Colosi, C. *et al.* Microfluidic bioprinting of heterogeneous 3D tissue constructs using low viscosity bioink. *Adv Mater* **28**, 677–684 (2016).
11. Zhang, B. *et al.* High-resolution 3D Bioprinting System for Fabricating Cell-laden Hydrogel Scaffolds with High Cellular Activities. *Procedia CIRP* **65**, 219–224 (2017).
12. Sears, N. A., Dhavalikar, P. S. & Cosgriff-Hernandez, E. M. Emulsion Inks for 3D Printing of High Porosity Materials. *Macromol Rapid Commun* **37**, 1369–1374 (2016).
13. Chan, S. S. L., Sesso, M. L. & Franks, G. v. Direct ink writing of hierarchical porous alumina-stabilized emulsions: Rheology and printability. *Journal of the American Ceramic Society* **103**, 5554–5566 (2020).
14. Minas, C., Carnelli, D., Tervoort, E. & Studart, A. R. 3D Printing of Emulsions and Foams into Hierarchical Porous Ceramics. *Advanced Materials* **28**, (2016).
15. Ambrosi, A. & Pumera, M. 3D-printing technologies for electrochemical applications. *Chem Soc Rev* **45**, 2740–2755 (2016).
16. Loh, H. A., Graves, A. R., Stinespring, C. D. & Sierros, K. A. Direct ink writing of graphene-based solutions for gas sensing. *ACS Appl Nano Mater* **2**, 4104–4112 (2019).
17. Schwab, A. *et al.* Printability and Shape Fidelity of Bioinks in 3D Bioprinting. *Chem Rev* **120**, 11028–11055 (2020).
18. Cipollone, D. *et al.* 3D printing of an anode scaffold for lithium batteries guided by mixture design-based sequential learning. *J Mater Process Technol* **295**, 117159 (2021).
19. Alejandra, M. *et al.* Engineered Inks for Environment-Friendly Additive Manufacturing of Hierarchical Microstructures Thesis submitted to the Statler College of Engineering and Mineral Resources Materials Science & Engineering Department of Mechanical & Aerospace Engineering. (2017).
20. Yan, J., Huang, S., Lim, Y. von, Xu, T. & Kong, D. Direct-ink writing 3D printed energy storage devices : From material selectivity , design and optimization strategies to diverse applications.
21. Saadi, M. A. S. R. *et al.* Direct Ink Writing: A 3D Printing Technology for Diverse Materials. *Advanced Materials* **2108855**, 2108855 (2022).
22. Hou, Z., Lu, H., Li, Y., Yang, L. & Gao, Y. Direct Ink Writing of Materials for Electronics-Related Applications: A Mini Review. *Front Mater* **8**, 1–8 (2021).
23. Shahzad, A. & Lazoglu, I. Direct ink writing (DIW) of structural and functional ceramics: Recent achievements and future challenges. *Composites Part B* **225**, (2021).
24. Maazouz, Y. *et al.* Robocasting of biomimetic hydroxyapatite scaffolds using self-setting inks †. (2014) doi:10.1039/c4tb00438h.
25. Seitz, H., Rieder, W., Irsen, S., Leukers, B. & Tille, C. Three-dimensional printing of porous ceramic scaffolds for bone tissue engineering. *J Biomed Mater Res B Appl Biomater* **74**, 782–788 (2005).

26. Skylar-Scott, M. A., Mueller, J., Visser, C. W. & Lewis, J. A. Voxeled soft matter via multimaterial multinozzle 3D printing. *Nature* **575**, 330–335 (2019).
27. Lan, H. Active mixing nozzle for multimaterial and multiscale three-dimensional printing. *J Micro Nanomanuf* **5**, 1–10 (2017).
28. Xu, C. *et al.* Multi-Material Direct Ink Writing (DIW) for Complex 3D Metallic Structures with Removable Supports. *ACS Appl. Mater. Interfaces* **11**, 36 (2019).
29. Nan, B. *et al.* Direct ink writing of macroporous lead-free piezoelectric Ba 0.85 Ca 0.15 Zr 0.1 Ti 0.9 O 3. *Journal of the American Ceramic Society* **102**, 3191–3203 (2019).
30. Elsayed, H., Chmielarz, A., Potoczek, M., Fey, T. & Colombo, P. Direct ink writing of three dimensional Ti2AlC porous structures. *Addit Manuf* **28**, 365–372 (2019).
31. Peng, E. *et al.* Robocasting of dense yttria-stabilized zirconia structures. *Journal of Materials Science: Ceramics* **53**, (2018).
32. Herrada-Manchón, H. *et al.* Effect on Rheological Properties and 3D Printability of Biphasic Calcium Phosphate Microporous Particles in Hydrocolloid-Based Hydrogels. *Gels* **8**, (2022).
33. Cifuentes, S. C. & Gordo, E. *Processing and characterization of novel biodegradable and bioresorbable PLA/Mg composites for osteosynthesis.*
34. Cifuentes, S. C., Benavente, R. & González-Carrasco, J. L. Does magnesium compromise the high temperature processability of novel biodegradable and bioresorbables PLLA/Mg composites? *Revista de Metalurgia* (2014) doi:10.3989/revmetalm.011.
35. Sachyani Keneth, E., Kamyshny, A., Totaro, M., Beccai, L. & Magdassi, S. 3D Printing Materials for Soft Robotics. *Advanced Materials* **2003387**, 1–17 (2020).
36. Zhou, L. *et al.* Multimaterial 3D Printing of Highly Stretchable Silicone Elastomers. *ACS Appl Mater Interfaces* **11**, 23573–23583 (2019).
37. Park, S. *et al.* Silicones for Stretchable and Durable Soft Devices: Beyond Sylgard-184. *ACS Appl Mater Interfaces* **10**, 11261–11268 (2018).
38. Niiyama, R., Rus, D. & Kim, S. Pouch Motors: Printable/inflatable soft actuators for robotics. *Proc IEEE Int Conf Robot Autom* 6332–6337 (2014) doi:10.1109/ICRA.2014.6907793.
39. Hughes, J. *et al.* Soft manipulators and grippers: A review. *Frontiers Robotics AI* **3**, 1–12 (2016).
40. Yirmibesoglu, O. D. *et al.* Direct 3D printing of silicone elastomer soft robots and their performance comparison with molded counterparts. in *2018 IEEE International Conference on Soft Robotics (RoboSoft)* 295–302 (IEEE, 2018). doi:10.1109/ROBOSOFT.2018.8404935.
41. Zhang, Y. F. *et al.* Miniature Pneumatic Actuators for Soft Robots by High-Resolution Multimaterial 3D Printing. *Adv Mater Technol* **4**, (2019).
42. Zhang, Y. *et al.* Fast-Response, Stiffness-Tunable Soft Actuator by Hybrid Multimaterial 3D Printing. *Adv Funct Mater* **29**, 1806698 (2019).



43. Zhou, Z., Jia, D., Hollingsworth, J. v., Cheng, H. & Han, C. C. From repulsive to attractive glass: A rheological investigation. *Journal of Chemical Physics* **143**, (2015).
44. Petekidis, G. Rheology of colloidal gels. *J Rheol (N Y N Y)* **58**, 1085–1087 (2014).
45. Xia, S., Wu, X., Zhang, Z., Cui, Y. & Liu, W. Practical Challenges and Future Perspectives of All-Solid-State Lithium-Metal Batteries. *Chem* **5**, 753–785 (2019).
46. Goodenough, J. B. & Kim, Y. Challenges for Rechargeable Li Batteries <sup>†</sup>. *Chemistry of Materials* **22**, 587–603 (2010).
47. Minami, T., Hayashi, A. & Tatsumisago, M. Recent progress of glass and glass-ceramics as solid electrolytes for lithium secondary batteries. *Solid State Ion* **177**, 2715–2720 (2006).
48. Takada, K. Progress and prospective of solid-state lithium batteries. *Acta Mater* **61**, 759–770 (2013).
49. Lin, D., Liu, Y. & Cui, Y. Reviving the lithium metal anode for high-energy batteries. *Nat Nanotechnol* **12**, 194–206 (2017).
50. Feichtinger, A., Scholten, E. & Sala, G. Effect of particle size distribution on rheological properties of chocolate. *Food Funct* **11**, 9547–9559 (2020).
51. Cipollone, D., Mena, J. A., Sabolsky, K., Sabolsky, E. M. & Sierros, K. A. Coaxial Ceramic Direct Ink Writing on Heterogenous and Rough Surfaces: Investigation of Core-Shell Interactions. *ACS Appl Mater Interfaces* **14**, 24897–24907 (2022).
52. Lewis, J. A., Smay, J. E., Stuecker, J. & Cesarano, J. Direct ink writing of three-dimensional ceramic structures. *Journal of the American Ceramic Society* **89**, 3599–3609 (2006).
53. Smay, J. E., Cesarano, J. & Lewis, J. A. Colloidal Inks for Directed Assembly of 3-D Periodic Structures. *Langmuir* **18**, 5429–5437 (2002).
54. Bingham, E. C. *An Investigation of the Laws of Plastic Flow*. (1916).
55. Herschel, W. H. & Bulkley, R. Konsistenzmessungen von Gummi-Benzollösungen. *Kolloid-Zeitschrift* **39**, 291–300 (1926).
56. Jaworski, Z., Spychaj, T., Story, A. & Story, G. Carbomer microgels as model yield-stress fluids. *Reviews in Chemical Engineering* (2021) doi:10.1515/revce-2020-0016.
57. Nelson, A. Z. & Ewoldt, R. H. Design of yield-stress fluids: A rheology-to-structure inverse problem. *Soft Matter* **13**, (2017).
58. Miri, T. Viscosity and Oscillatory Rheology. in *Practical Food Rheology: An Interpretive Approach* 7–28 (Wiley-Blackwell, 2010). doi:10.1002/9781444391060.ch2.
59. Muth, J. T., Dixon, P. G., Woish, L., Gibson, L. J. & Lewis, J. A. Architected cellular ceramics with tailored stiffness via direct foam writing. *Proceedings of the National Academy of Sciences* (2017) doi:10.1073/pnas.1616769114.
60. TA Instruments. *Rheological Techniques for Yield Stress Analysis*.

61. TA Instruments. *Rheological Techniques for Yield Stress Analysis*.
62. Naghieh, S., Sarker, M. D., Sharma, N. K., Barhoumi, Z. & Chen, X. Printability of 3D printed hydrogel scaffolds: Influence of hydrogel composition and printing parameters. *Applied Sciences (Switzerland)* **10**, (2020).
63. Feilden, E., Blanca, E. G. T., Giuliani, F., Saiz, E. & Vandeperre, L. Robocasting of structural ceramic parts with hydrogel inks. *J Eur Ceram Soc* **36**, 2525–2533 (2016).
64. Alkhnbashi, O. S., Meier, T., Mitrofanov, A., Backofen, R. & Voß, B. 3D printing via the direct ink writing technique of ceramic pastes from typical formulations used in traditional ceramics industry. (2019).
65. Bastola, A. K., Paudel, M. & Li, L. Development of hybrid magnetorheological elastomers by 3D printing. *Polymer (Guildf)* **149**, (2018).
66. Corker, A., Ng, H. C. H., Poole, R. J. & García-Tuñón, E. 3D printing with 2D colloids: Designing rheology protocols to predict ‘printability’ of soft-materials. *Soft Matter* **15**, 1444–1456 (2019).
67. Trappe, V., Prasad, V., Cipelletti, L., Segre, P. N. & Weitz, D. A. Jamming phase diagram for attractive particles. *Nature* **411**, 772–775 (2001).
68. Fuchs, M. & Cates, M. E. Schematic models for dynamic yielding of sheared colloidal glasses. *Faraday Discuss* **123**, 267–286 (2003).
69. Nelson, A. Z. *et al.* Designing and transforming yield-stress fluids. *Curr Opin Solid State Mater Sci* **23**, 1–34 (2019).
70. Zhang, B. *et al.* Direct ink writing of polycaprolactone / polyethylene oxide based 3D constructs. *Progress in Natural Science: Materials International* **31**, 180–191 (2021).
71. Dolganov, A., Bishop, M. T., Chen, G. Z. & Hu, D. Rheological study and printability investigation of titania inks for Direct Ink Writing process. *Ceram Int* **47**, 12020–12027 (2021).
72. Sun, Q. *et al.* Creation of three-dimensional structures by direct ink writing with kaolin suspensions. *J Mater Chem C Mater* **6**, 11392–11400 (2018).
73. M’Barki, A., Bocquet, L. & Stevenson, A. Linking Rheology and Printability for Dense and Strong Ceramics by Direct Ink Writing. *Sci Rep* **7**, 1–10 (2017).
74. Chan, S. S. L., Pennings, R. M., Edwards, L. & Franks, G. v. 3D printing of clay for decorative architectural applications: Effect of solids volume fraction on rheology and printability. *Addit Manuf* **35**, (2020).
75. Ji, H. *et al.* A novel experimental approach to quantitatively evaluate the printability of inks in 3D printing using two criteria. *Addit Manuf* (2022).
76. Sarraf, H. *et al.* Direct Probing of Dispersion Quality of ZrO<sub>2</sub> Nanoparticles Coated by Polyelectrolyte at Different Concentrated Suspensions. *Nanoscale Res Lett* **10**, 1–14 (2015).

77. Zocca, A., Colombo, P., Gomes, C. M. & Günster, J. Additive Manufacturing of Ceramics: Issues, Potentialities, and Opportunities. *Journal of the American Ceramic Society* **98**, 1983–2001 (2015).
78. Costakis, W. 3D printable ceramic pastes design: Correlating rheology & printability. *J Eur Ceram Soc* **42**, (2022).
79. Minas, C., Carnelli, D., Tervoort, E. & Studart, A. R. 3D Printing of Emulsions and Foams into Hierarchical Porous Ceramics. *Advanced Materials* **28**, 9993–9999 (2016).
80. Rueschhoff, L., Costakis, W., Michie, M., Youngblood, J. & Trice, R. Additive Manufacturing of Dense Ceramic Parts via Direct Ink Writing of Aqueous Alumina Suspensions. (2016) doi:10.1111/ijac.12557.
81. Karyappa, R. & Hashimoto, M. Chocolate-based Ink Three-dimensional Printing (Ci3DP). *Sci Rep* **9**, (2019).
82. García-Tuñón, E. *et al.* Graphene Oxide: An All-in-One Processing Additive for 3D Printing. *ACS Appl Mater Interfaces* **9**, 32977–32989 (2017).
83. Costaskis, W. Additive manufacturing of boron carbide via continuous filament direct ink writing of aqueous ceramic suspensions. *J Eur Ceram Soc* **36**, 3249–3256 (2016).
84. Zhu, C. *et al.* Highly compressible 3D periodic graphene aerogel microlattices. *Nat Commun* **6**, 1–8 (2015).
85. Fu, Q., Saiz, E. & Tomsia<sup>1</sup>, A. P. Direct Ink Writing of Highly Porous and Strong Glass Scaffolds for Load-bearing Bone Defects Repair and Regeneration. *Mol Cell Biochem* **7**, 3547–3554 (2011).
86. Petekidis, G. & Wagner, N. J. Rheology of Colloidal Glasses and Gels. in *Theory and Applications of Colloidal Suspension Rheology* 173–226 (2021).
87. Moghimi, E. & Petekidis, G. Mechanisms of two-step yielding in attractive colloidal glasses. *J Rheol (N Y N Y)* **64**, 1209–1225 (2020).
88. Marnot, A., Dobbs, A. & Engineering, B. Material extrusion additive manufacturing of dense pastes consisting of macroscopic particles Challenges in AM dense pastes Particle characteristics. *MRS Commun* **XX**, 1–12 (2022).
89. Sarker, M. & Chen, X. B. Modeling the Flow Behavior and Flow Rate of Medium Viscosity Alginate for Scaffold Fabrication With a Three-Dimensional Bioplotter. *Journal of Manufacturing Science and Engineering, Transactions of the ASME* **139**, 1–14 (2017).
90. Gulicovski, J. J., Čerović, L. S. & Milonjić, S. K. Point of zero charge and isoelectric point of alumina. *Materials and Manufacturing Processes* **23**, 615–619 (2008).
91. Wiśniewska, M., Chibowski, S., Urban, T. & Sternik, D. Investigation of the alumina properties with adsorbed polyvinyl alcohol. *J Therm Anal Calorim* **103**, 329–337 (2011).
92. Joshi, Y. M. Dynamics of colloidal glasses and gels. *Annu Rev Chem Biomol Eng* **5**, 181–202 (2014).

93. Ashby, M. F. *Materials Selection in Mechanical Design*. (Elsevier, 2011). doi:10.1016/C2009-0-25539-5.
94. Wegst, U. G. K., Bai, H., Saiz, E., Tomsia, A. P. & Ritchie, R. O. Bioinspired structural materials. *Nat Mater* **14**, 23–36 (2015).
95. Manikandan, K., Jiang, X., Singh, A. A., Li, B. & Qin, H. Effects of nozzle geometries on 3D printing of clay constructs: Quantifying contour deviation and mechanical properties. in vol. 48 678–683 (Elsevier B.V., 2020).
96. Wilms, P., Hinrichs, J. & Kohlus, R. Macroscopic rheology of non-Brownian suspensions at high shear rates: the influence of solid volume fraction and non-Newtonian behaviour of the liquid phase. *Rheol Acta* **61**, 123–138 (2022).
97. Shah, S. A., Ramakrishnan, S., Chen, Y. L., Schweizer, K. S. & Zukoski, C. F. Scattering studies of the structure of colloid-polymer suspensions and gels. *Langmuir* **19**, 5128–5136 (2003).
98. Prasad, V. *et al.* Rideal Lecture Universal features of the fluid to solid transition for attractive colloidal particles. *Faraday Discuss* **123**, 1–12 (2003).
99. Fuchs, M. & Cates, M. E. Schematic models for dynamic yielding of sheared colloidal glasses. *Faraday Discuss* **123**, 267–286 (2003).
100. An, T., Hwang, K. T., Kim, J. H. & Kim, J. Extrusion-based 3D direct ink writing of NiZn-ferrite structures with viscoelastic ceramic suspension. *Ceram Int* **46**, 6469–6476 (2020).
101. Peysson, Y., Aubry, T. & Moan, M. Phenomenological approach of the effective viscosity of hard sphere suspensions in shear-thinning media. *Applied Rheology* **16**, 145–151 (2006).
102. Papadopoulou, A., Gillissen, J. J., Wilson, H. J., Tiwari, M. K. & Balabani, S. On the shear thinning of non-Brownian suspensions: Friction or adhesion? *J Nonnewton Fluid Mech* **281**, 104298 (2020).
103. Zhou, Z., Jia, D., Hollingsworth, J. v., Cheng, H. & Han, C. C. From repulsive to attractive glass: A rheological investigation. *Journal of Chemical Physics* **143**, (2015).
104. Lamnini, S., Baino, F., Montalbano, G., Javed, H. & Smeacetto, F. Printability of carboxymethyl cellulose/glass-containing inks for robocasting deposition in reversible solid oxide cell applications. *Mater Lett* **318**, 132239 (2022).
105. Paxton, N. *et al.* Proposal to assess printability of bioinks for extrusion-based bioprinting and evaluation of rheological properties governing bioprintability. *Biofabrication* **9**, (2017).
106. Sun, Q. *et al.* Direct ink writing of 3D cavities for direct plated copper ceramic substrates with kaolin suspensions. *Ceram Int* **45**, 12535–12543 (2019).
107. Wilt, J. K., Gilmer, D., Kim, S., Compton, B. G. & Saito, T. Direct ink writing techniques for in situ gelation and solidification. *MRS Commun* **11**, 106–121 (2021).
108. Yun, Q. *et al.* Chemical Dealloying Derived 3D Porous Current Collector for Li Metal Anodes. *Advanced Materials* **28**, 6932–6939 (2016).

109. Zhang, C. *et al.* Vertically Aligned Lithiophilic CuO Nanosheets on a Cu Collector to Stabilize Lithium Deposition for Lithium Metal Batteries. *Adv Energy Mater* **8**, 1703404 (2018).
110. Shen, K., Li, B. & Yang, S. 3D printing dendrite-free lithium anodes based on the nucleated MXene arrays. *Energy Storage Mater* **24**, 670–675 (2020).
111. Yang, C. P., Yin, Y. X., Zhang, S. F., Li, N. W. & Guo, Y. G. Accommodating lithium into 3D current collectors with a submicron skeleton towards long-life lithium metal anodes. *Nat Commun* (2015) doi:10.1038/ncomms9058.
112. McOwen, D. W. *et al.* 3D-Printing Electrolytes for Solid-State Batteries. *Advanced Materials* **30**, 1–7 (2018).
113. Franks, G. v., Tallon, C., Studart, A. R., Sesso, M. L. & Leo, S. Colloidal processing: enabling complex shaped ceramics with unique multiscale structures. *Journal of the American Ceramic Society* **100**, 458–490 (2017).
114. Chi, S. sen *et al.* Solid polymer electrolyte soft interface layer with 3D lithium anode for all-solid-state lithium batteries. *Energy Storage Mater* **17**, 309–316 (2019).
115. Dutta, C., Kumar, J., Das, T. K. & Sagar, S. P. Recent Advancements in the Development of Sensors for the Structural Health Monitoring (SHM) at High-Temperature Environment: A Review. *IEEE Sens J* **21**, 15904–15916 (2021).
116. Petrie, C. M., Sridharan, N., Hehr, A., Norfolk, M. & Sheridan, J. Higherature strain monitoring of stainless steel using fiber optics embedded in ultrasonically consolidated nickel layers. *Smart Mater Struct* **28**, (2019).
117. Petrie, C. M., Schrell, A. M. & Richardson, M. D. *Performance of Embedded Sensors in 3D Printed SiC*. (2021).
118. Rafiee, M., Granier, F. & Theriault, D. Advances in Coaxial Additive Manufacturing and Applications. *Adv Mater Technol* **46**, 1 (2021).
119. Géraud, B. *et al.* Capillary rise of yield-stress fluids. *EPL (Europhysics Letters)* **107**, 58002 (2014).
120. Shao, Y., Han, R., Quan, X. & Niu, K. Study on ink flow of silicone rubber for direct ink writing. *J Appl Polym Sci* **138**, 1–11 (2021).
121. Kalyon, D. M. & Aktaş, S. Factors affecting the rheology and processability of highly filled suspensions. *Annu Rev Chem Biomol Eng* **5**, 229–254 (2014).
122. Fuhrmann, P. L. *et al.* Rheological behaviour of attractive emulsions differing in droplet-droplet interaction strength. *J Colloid Interface Sci* **607**, 389–400 (2022).
123. Deneault, J. R. *et al.* Toward autonomous additive manufacturing: Bayesian optimization on a 3D printer. *MRS Bull* 1–10 (2021) doi:10.1557/s43577-021-00051-1.
124. Menon, A., Póczos, B., Feinberg, A. W. & Washburn, N. R. Optimization of Silicone 3D Printing with Hierarchical Machine Learning. *3D Print Addit Manuf* **6**, 181–189 (2019).